nanomaterials

Nanoalloy Electrocatalysts for Electrochemical Devices

Edited by
César Augusto Correia de Sequeira

Printed Edition of the Special Issue Published in *Nanomaterials*

www.mdpi.com/journal/nanomaterials

MDPI

Nanoalloy Electrocatalysts for Electrochemical Devices

Nanoalloy Electrocatalysts for Electrochemical Devices

Editor

César Augusto Correia de Sequeira

MDPI • Basel • Beijing • Wuhan • Barcelona • Belgrade • Manchester • Tokyo • Cluj • Tianjin

Editor
César Augusto Correia de
Sequeira
University of Lisbon
Lisboa
Portugal

Editorial Office
MDPI
St. Alban-Anlage 66
4052 Basel, Switzerland

This is a reprint of articles from the Special Issue published online in the open access journal *Nanomaterials* (ISSN 2079-4991) (available at: https://www.mdpi.com/journal/nanomaterials/special_issues/nanoalloy_electrocatalysts).

For citation purposes, cite each article independently as indicated on the article page online and as indicated below:

LastName, A.A.; LastName, B.B.; LastName, C.C. Article Title. *Journal Name* **Year**, *Volume Number*, Page Range.

ISBN 978-3-0365-4821-0 (Hbk)
ISBN 978-3-0365-4822-7 (PDF)

Cover image courtesy of Dr. Maria Augusta G. Martins

Contents

About the Editor

César Augusto Correia de Sequeira

César AC Sequeira, PhD, has been a member of the faculty staff of Instituto Superior Técnico (Univ. of Lisbon), maintaining his academic career in fundamental and technological electrochemistry for more than 50 years. He is author/co-author of over 280 professional papers, 330 scientific communications, and 42 books and book chapters in the areas of corrosion science and technology, electrochemistry, and materials science. He has directed numerous workshops, research projects, and advanced short courses. He is a Fellow of The Royal Society of Chemistry (UK) and of The Institute of Materials (UK), and is an Emeritus Member of The Electrochemical Society (USA).

nanomaterials

MDPI

Editorial

Editorial for the Special Issue on "Nanoalloy Electrocatalysts for Electrochemical Devices"

César A. C. Sequeira

Materials Electrochemistry Group, CeFEMA, Instituto Superior Técnico, University of Lisbon, 1049-001 Lisboa, Portugal; cesarsequeira@ist.utl.pt

Nanoscale science and technology dealing with materials synthesis, nanofabrication, nanoprobes, nanostructures, nanoelectronics, nano-optics, nanomechanics, nanodevices, nanobiotechnology, and nanomedicine is an exciting field of research and development in Europe, the United States, and other countries around the world [1–4]. Over the past two decades, considerable progress has been made with countless discoveries advancing the understanding of the nanoscale and enabling applications from advanced electronic, magnetic, and electrochemical devices, energy, and defense to life-saving medicines [5–10]. At the heart of these fields are specific complexes of solid units that possess sizes between one and hundred nanometers (1–100 nm), which we call "nanomaterials" [11,12]. These materials have a very large surface area to volume ratio when compared with bulk material and can be produced using chemical or physical methods. They are small enough to confine their electrons and produce quantum effects, thus leading to unexpected chemical, mechanical, magnetic, electronic, electrochemical, and optical properties. They are classified into three major categories—namely, nanoparticles, nanoclays, and nanoemulsions. Nanoparticles can exist as nanostructures or as composites. All nanostructures can be built from elementary units or blocks having low dimensionality. It could either be zero dimension, one dimension, two dimensions, or three dimensions. If only one dimension of a three-dimensional nanostructure is of nanoscale, the structure is referred to as a quantum well; if two dimensions are of nanometer scale, the structure is referred to as a quantum wire; and if all three dimensions are of nanometer scale, the structure is referred to as a quantum dot. Hence, a quantum dot has all three dimensions in the nanorange and is the ultimate example of nanomaterials. The word quantum is associated with these three types of nanostructures because changes in properties arise from the physics of quantum mechanics. Nanoparticles are either organic or inorganic. Inorganic nanoparticles are more stable than organic nanoparticles but are limited by their stability in terms of either mechanical or chemical properties. Nanoclays are prepared using ion-exchange reactions, and usually, their chemical composition is characterized by FTIR. Nanoemulsions can be synthesized by high (e.g., ultrasonification, microfluidization) or low energy emulsification (e.g., solvent displacement, phase inversion composition). In parallel to the development of applications, considerable worldwide attention has focused on the potential implications of nanomaterials and vastly improved our understanding of nanosafety and other emerging nanosciences. Early focus areas of nanoscience, such as nanophotonics, have grown into their own fields. New suites of tools are now available to fabricate and characterize nanomaterials and enable their integration into devices and systems. Additionally, a vibrant, interdisciplinary, and international nanotechnology community has developed [13–23].

With this in mind, and considering that, as a chemical engineer with a doctoral thesis in material science, I have been working for many years in applied domains of electrochemistry in which metallic, bimetallic, trimetallic and other nanoalloys find several applications in the areas of partial oxidation/reduction of fuel cells, catalysis of methane and synthetic ammonia, energy storage, water electrolyzers, electrochemical detectors,

Citation: Sequeira, C.A.C. Editorial for the Special Issue on "Nanoalloy Electrocatalysts for Electrochemical Devices". *Nanomaterials* **2022**, *12*, 132. https://doi.org/10.3390/nano12010132

Received: 8 December 2021
Accepted: 29 December 2021
Published: 31 December 2021

contaminant degradation in water and wastewater, electronic devices, nanomedicine, cellphones, biosensing, drug delivery, electric cars, electrochemical sensors, electrodegradation devices, hydrogen peroxide producers, etc., I was encouraged by the Nanomaterials Coordination Office to advance a Special Issue providing examples of ongoing nanotechnology research, current applications, and an overview of new elements of nanoalloy electrocatalysts, reporting their synthesis, characterization, modeling, unique properties and low cost for electrochemical devices.

Many techniques have been developed to synthesize and fabricate nanomaterials and, in particular, metallic nanoparticles, with controlled shape, size, dimensionality, and structure. The performance of these materials depends on their properties. The properties, in turn, depend on the atomic structure, composition, microstructure, defects, and interfaces, which are controlled by thermodynamics and kinetics of the synthesis. There are two technical approaches for the synthesis of metallic nanoparticles—namely, top-down and bottom-up processes. The former involves the breaking down of the bulk material into nanosized structures or particles. It is inherently simpler and depends either on the removal or division of bulk material or on miniaturization of bulk fabrication processes to produce the desired structure with appropriate properties. Usually, the prepared surface structure contains many impurities and structural defects. Examples of top-down techniques are high-energy wet ball milling, electron beam lithography, atomic force manipulation, gas-phase condensation, aerosol spray, etc. The latter approach refers to the build-up of material from the bottom: atom by atom, molecule by molecule, or cluster by cluster. The organometallic chemical route, reversed micellar route, sol–gel synthesis, colloidal precipitation, hydrothermal synthesis, template-assisted sol–gel, electrodeposition, etc., are some of the well-known bottom-up techniques reported for the preparation of diverse nanoparticles. It has been found that the Gibbs free energy, the thermodynamic equilibrium, and the kinetic methods are the main strategies for the synthesis of nanoparticles by the bottom-up approach.

Many of the bottom-up techniques (or molecular nanotechnology) are still under development or are just beginning to be used for commercial production, belonging to the process intensification philosophy, whose peculiar operative conditions intend to maximize the mass/heat/momentum transfer inside the processing unit itself [2,24,25]. The objective of process intensification is not so as to "increase the efficiency and reduce the plant size", but also to enhance the production efficiency and process safety, to lower the cost, and to minimize the waste at source for reducing the environmental pollution [2].

The spinning disk reactor is a promising process intensification technology for heat and mass transfer rate enhancement. The hydrothermal route is another relevant technique that, according to Chen et al. [25] allowed the synthesis of well-dispersed zinc oxide and carbon co-modified $LiFePO_4$ spherical particles (promising cathode materials for lithium-ion batteries). Green and bio-based technologies permit also to achieve reproducible nanomaterials applied in biomedical, medical, and electrochemical fields. In this context, electrochemical devices that address rising energy demands with the corresponding disadvantages are experiencing a change in this situation by process intensification. For example, Carmo et al. [5] reported $Pt_{57.5}$ $Cu_{14.7}$ $Ni_{5.3}$ $P_{22.5}$ bulk metallic glass (Pt-BMG) nanowires, which circumvent the performance problems of electrochemical devices. Pt-BMG nanowires catalysts were fabricated by a nanoimprinting approach, with high conductivity and activity for methanol and ethanol oxidation. After 1000 cycles, these nanowires, maintain 96% of their performance—2.4 times as much as conventional Pt/C catalysts. Their properties make them ideal candidates for energy conversion/storage and sensors. Using a contemporary PtCu-alloy electrocatalyst as a model system, a unique approach caused by the process of dealloying was presented by Ruiz-Zepeda et al. [11]. Observing detailed structures of the same nanoparticle at different stages of electrochemical treatment, they found new insights on properties such as size, faceting, strain, and porosity development. Furthermore, based on microscopy data and Kinetic Monte Carlo (KMC) simulations, they provided further feedback into the physical parameters governing electrochemically induced structural dy-

namics. This unique approach paves the way for an understanding of the structure–stability relationship.

In the area of alkaline polymer electrolyte fuel cells (APEFCs), a series of Ni-Cu binary alloy films were prepared using a combinatorial magnetron computing method, and their corresponding electrocatalytic performances toward HOR in alkaline media were systematically studied [19]. A volcano-type correlation between HOR activity and Cu doping content was revealed. The impart of Cu addition on the HOR catalytic activity (and antioxidation property) of Ni was deeply understood.

Allowing two kinds of metal, such as platinum group metals with 3d transition metals, has a great interest in advanced technological applications due to enhanced chemical stability and catalytic activities via increased active surface area [20,22]. In particular, loading Pt-based nanoparticles with ferromagnetic Fe, Co, and Ni atoms result in a reduction in the production cost, while the catalytic activities increase, such as hydrogen evolution and oxygen reduction reactions, the magnetic properties controlled, such as coercivity and saturation magnetization, for practical applications [6]. While Pt Fe alloy nanoparticles are widely used for permanent magnets (uniaxial magnetocrystalline anisotropy) and good chemical stability, PtNi nanoparticles is a promising material for magnetoresistive sensors, ultra-high density data recording technologies, and magnetic resonance imaging (MRI) applications, and exhibits better performance and durability for catalytic activities than commercially available Pt/C [26].

Electrodeposition is one of the practical methods to make nanocrystalline (NC) materials. There are two classes of deposition methods—electrodeposition and electroless deposition; both are inexpensive methods to manufacture relatively ductile metallic bulk materials or films/coatings. Electrodeposition is usually used for making thicker films (with higher deposition rates), while electroless deposition is typically employed for making high-quality thin coatings. The grain size and microstructure of electrodeposited films are controlled by tuning deposition parameters. Furthermore, these deposition parameters can be changed continuously or discontinuously to make functionally graded materials. The density, thickness, grain orientation of the deposited films can also be affected by the substrate conditions. To date, electrodeposition methods have been used to make various NC-materials (<100 nm in grain size) including Ni, Co, Pd, Cu, Zn, Ni-P, Ni-Fe, Ni-W, Zn-Ni, Ni-Fe-Cr, Ni-SiC, etc. The hardness, wear resistance, and electrical resistivity of most of these NCs are strongly dependent on grain size, surface morphology, and preferred orientation, and these effects are better exhibited by pulse than by direct current electrodeposition.

The corrosion behavior of NC alloys has been assessed by several techniques in various environments [27–31]. First results on the corrosion of crystallized melt-spun materials were obtained in Fe-Ni-Cr-P-B alloys in chloride–sulfate and sulfuric acid solutions [27,28]. It was determined that the corrosion resistance of the NC made of Fe_{32}-Ni_{36}-Cr_{14}-P_{12}-B_6 was significantly greater than that of the amorphous counterpart. This improved corrosion resistance was attributed to the observed enrichment of Cr in the passive layer due to rapid interface boundary diffusion. Zeiger et al. [29] studied NCs made of Fe8Al in sodium sulfate solution. At the earlier stage of the formation of oxide film, this region becomes impoverished in Al. Diffusion of Al occurs due to a gradient in the Al content between the region beneath the Al oxide and the bulk alloy. The diffusion preferentially occurs through the grain boundaries and is enhanced in NC alloy due to its higher density of intergranular paths. As in NC alloy, the protective Al oxide is formed rapidly, and the uniformity and the compactness of passive film are enhanced. This film constitutes an effective barrier and protects the alloy against corrosion. Thus, it is possible to apply Fe8Al alloy films on carbon steel surfaces as protective measures. Barbucci et al. [30] investigated the corrosion behavior of $Cu_{90}Ni_{10}$ alloy in neutral media containing chlorides. They reported a decrease in the protective properties of the passive layer in the nanostructured alloy that was found to depend on the oxygen concentration. The increased amount of grain boundary in the nanostructured alloy could justify the loss of oxide compactness as a result of its irregular

growth on the surface. Alves et al. [31] found that NC alloys made of $(Ni_{70}\ Mo_{30})_{90}B_{10}$ are less sensitive to corrosion in alkaline solutions than the coarse-grained material.

Engineering alloys for high-temperature applications rely on the formation of protective oxide films such as Al_2O_3 and Cr_2O_3 to resist high temperature and corrosive environments. The high density of grain boundaries in an NC material provides fast diffusion paths, promoting selective oxidation of protective oxide scales with better adhesion to the substrate. Consequently, the percentage of passivating elements (such as Al and Cr) in the alloy/composite that is required to form a complete protective oxide scale can be substantially reduced. Experimental results indicate that when the grain size of the NC comprising Ni-20Cr-Al coatings was $\sim$ 60 nm, alloys containing $\sim$ 2 wt% Al could form a complete α-Al_2O_3 scale at 1000 °C in air. This concentration is only one-third of the required Al% for Ni-20Cr alloys with normal grain size [8].

The interest in Ti alloys and TiAl intermetallic alloys is growing in recent years because of their excellent ratio between mechanical properties and density [32]. However, for the last 15 years, the application was restricted at temperatures up to 873–973 K by the resistance to oxidation. For this reason, it was of great importance to study protective coatings able to raise its temperature of performance above 1073 K. A $TiAl_3$ layer was obtained on the surface of TiAl intermetallic samples, depositing an Al coating by arc physical vapor deposition, followed by a thermal treatment. The mechanical behavior of the thermally treated layer was investigated by means of scratch tests and nanoindentation. Oxidations at 1123 K were carried out on coated and uncoated samples, in order to study the effect of the coating on the oxidation resistance of the samples. The aluminide coating provides protection against oxidation in air at the considered temperatures due to its ability to form a continuous $Al_2\ O_3$ scale on the surface. Thus, these nano- or submicro-alloy coatings provide powerful tools for TiAl intermetallics to be used as high-temperature structural materials [8].

Many of the latest contributions on the possibilities and challenges to overcome the drawbacks that nanotechnology still exhibits and that prevent its large-scale development have been collected above, emphasizing nanoalloys for electrochemical devices. This Special Issue deals with these multimetallic nanoparticles and their theoretical and computational studies, as well as their synthesis, characterization, chemical and physical properties, and recent electrochemical application-driven research. The Guest Editor is very satisfied with the contributions received and finally published.

Funding: This research received no extra funding.

Data Availability Statement: Not applicable.

Conflicts of Interest: The authors declare no conflict of interest.

References

1. Nalwa, H.S. (Ed.) *Handbook of Nanostructured Materials and Nanotechnology*; Academic Press: San Diego, CA, USA, 2000; Volume 1.
2. Hakke, V.; Sonawane, S.; Anandan, S.; Sonawane, S.; Ashokkumear, M. Process intensification approach using microreactors for synthesizing nanomaterials—A critical review. *Nanomaterials* **2021**, *11*, 98. [CrossRef]
3. Ferriday, T.B.; Middleton, P.H. Alkaline fuel cell technology—A review. *Int. J. Hydrog. Energy* **2021**, *46*, 18489–18510. [CrossRef]
4. Oshchefkov, A.G.; Braesch, G.; Bonnefont, A.; Savinova, E.R.; Chatenet, M. Recent advances in the understanding of nickel-based catalysts for the oxidations of hydrogen-containing fuels in alkaline media. *ACS Catal.* **2020**, *10*, 7043–7068. [CrossRef]
5. Carmo, M.; Sekol, R.C.; Ding, S.; Kumar, G.; Schroers, J.; Taylor, A.D. Bulk metallic glass nanowire architecture for electrochemical application. *ACS Nano* **2011**, *5*, 2979–2983. [CrossRef]
6. Kaya, D.; Adanur, I.; Akyol, M.; Karadag, F.; Ekicibil, A. Detailed investigation of structural and magnetic properties of multiphase binary Pd-Co alloys prepared by modified polyol process. *J. Alloys Compd.* **2021**, *876*, 160157. [CrossRef]
7. Saji, V.S.; Thomas, J. Nanomaterials for corrosion control. *Curr. Sci.* **2007**, *92*, 51–55.
8. Gao, W.; Li, Z. Nano-structured alloy and composite coatings for high temperature applications. *Mater. Res.* **2006**, *7*, 175–182. [CrossRef]
9. Zhao, G.; Chen, J.; Sun, W.; Pan, H. Non-platinum group metal electrocatalysts toward efficient hydrogen, oxidation reaction. *Adv. Funct. Mater.* **2021**, *31*, 2010633. [CrossRef]
10. Palmer, R.E. (Ed.) *Frontiers in Nanoscience*; Elsevier Ltd.: London, UK, 2012.

11. Ruiz-Zepeda, F.; Gatalo, M.; Pavlisic, A.; Drazic, G.; Yovanovic, P.; Bela, M.; Gaberscek, M.; Hodnik, N. Atomically resolved anisotropic electrochemical shaping of nano-electrocatalyst. *Nano Lett.* **2019**, *19*, 4919–4928. [CrossRef]
12. Zhao, R.; Yue, X.; Li, Q.; Fu, G.; Lee, J.-M.; Huang, S. Recent advances in electrocatalysts for alkaline hydrogen oxidation reaction. *Small* **2021**, *5*, 2100391. [CrossRef]
13. Zhao, L.; Lin, H.; Lin, Y.; Han, X.; Xu, J.; Xing, W.; Guo, W. Mechanistic insights into the hydrogen oxidation reactions on PtNi alloys in alkaline media: A first-principles investigation. *ACS Appl. Mater. Interfaces* **2020**, *12*, 40248–40260. [CrossRef] [PubMed]
14. Mao, J.; He, C.-T.; Pei, J.; Lin, Y.; Li, J.; Chen, W.; He, D.; Wang, D.; Li, Y. Isolated Ni atoms dispersed on Ru nanosheets: High-performance electrocatalyst toward hydrogen oxidation reaction. *Nano Lett.* **2020**, *20*, 3442–3448. [CrossRef] [PubMed]
15. Su, L.; Gong, D.; Jin, Y.; Wu, D.; Luo, W. Recent advances in alkaline hydrogen oxidation reaction. *J. Energy Chem.* **2022**, *66*, 107–122. [CrossRef]
16. Kinn, H.; Park, H.; Tran, D.S.; Kim, S.-K. Facile fabrication of amorphous Ni Mo catalysts for alkaline hydrogen oxidation reaction. *J. Ind. Eng.* **2021**, *94*, 309–316.
17. Zhao, G.; Jiang, Y.; Dou, S.-X.; Sun, W.; Pan, H. Interface engineering of heterostructured electrocatalysts towards efficient alkaline hydrogen electrocatalysis. *Sci. Bull.* **2021**, *66*, 85–96. [CrossRef]
18. Marenych, O.; Kostryzher, A. Strengthening mechanisms in nickel-copper alloys: A review. *Metals* **2020**, *10*, 1358. [CrossRef]
19. Wang, G.; Li, W.; Huang, B.; Xiao, L.; Lu, J.; Zhuang, L. Exploring the composition-activity relation of Ni-Cu binary alloy electrocatalysts for hydrogen oxidation reaction in alkaline media. *ACS Appl. Energy Mater.* **2019**, *2*, 3160–3165. [CrossRef]
20. Martins, M.; Sljukić, B.; Metim, Ö.; Sevim, M.; Sequeira, C.A.C.; Sener, T.; Santos, D.M.F. Bimetallic Pd M (M=F_e, A_g, Au) nanoparticles assembled reduced graphene oxide fuel cells. *J. Alloys Compd.* **2017**, *718*, 204–214. [CrossRef]
21. Hosseini, M.G.; Daneshvari-Esfahlan, V.; Aghajani, H.; Wolf, S.; Hacker, V. Palladium-nickel electrocatalysts on nitrogen-doped reduced graphene oxide nanosheets for direct hydrazine/hydrogen peroxide fuel cells. *Catalysts* **2021**, *11*, 1372. [CrossRef]
22. Zaleska-Medynska, A.; Manchelek, M.; Diak, M.; Grabowska, E. Noble metal-based bimetallic nanoparticles: The: Effect of the structure the optical, catalytic and photocatalytic properties. *Adv. Colloid Interface Sci.* **2016**, *229*, 80–107. [CrossRef] [PubMed]
23. Pogrebnjak, A.D.; Bondar, O. (Eds.) *Microstructure and Properties of Micro and Nanoscale Materials, Films, and Coatings (NAP 2019)*; Springer Nature: Singapore, 2020.
24. Stoller, M.; Ochande-Pullide, J.M. ZnO nanoparticles production intensification by means of a spinning disk reactor. *Nanomaterials* **2020**, *10*, 1321. [CrossRef] [PubMed]
25. Chen, C.; Li, Y.; Wang, J. Enhanced electrochemical performance of $LiFePo_u$ originating from the synergistic effect of ZuO and C-Co modification. *Nanomaterials* **2021**, *11*, 82.
26. Kaya, D. Synthesis and structural characterization of binary PtNi alloy nanoparticles: Investigating magnetic transition. *J. Mater. Sci. Mater. Electron.* **2021**, *32*, 27975–27986. [CrossRef]
27. Thorpe, S.J.; Ramaswami, B.; Aust, K.T. Corrosion and Auger studies of a nickel-base metal-metalloid glass. *J. Electrochem. Soc.* **1988**, *135*, 2162–2170. [CrossRef]
28. Bragagnolo, P.; Waseda, Y.; Palumbo, G.; Aust, K.T. Corrosion/coating of advanced materials. In Proceedings of the MRS Symposium, Boston, MA, USA, 27 November–2 December 1989; Volume 4, pp. 469–474.
29. Zeiger, W.; Schneider, M.; Scharnwber, D.; Worch, H. Corrosion behavior of a nanocrystalline FeAl8 alloy. *Nanostruct. Mater.* **1995**, *6*, 1013–1016. [CrossRef]
30. Barbucci, A.; Farne, G.; Mattaezzi, P.; Riccieri, R.; Cereisola, G. Corrosion behavior of nanocrystalline Cu90Ni10 alloy in neutral solution containing chlorides. *Corros. Sci.* **1999**, *41*, 463–475. [CrossRef]
31. Alves, H.; Ferreira, M.G.S.; Koster, U. Corrosion behavior of nanocrystalline (Ni70Mo30)90B10 alloys in 0.8 M KOH solution. *Corros. Sci.* **2003**, *45*, 1833–1845. [CrossRef]
32. Saji, V.S.; Cook, R. (Eds.) *Corrosion Protection and Control using Nanomaterials*; Woodhead Publishing in Materials: Oxford, UK, 2012.

nanomaterials

MDPI

Article

Synthesis and Characterization of PdAgNi/C Trimetallic Nanoparticles for Ethanol Electrooxidation

Ahmed Elsheikh [1,2,*] and James McGregor [2,*]

[1] Mechanical Engineering Department, South Valley University, Qena 83511, Egypt
[2] Department of Chemical and Biological Engineering, University of Sheffield, Sheffield S1 3JD, UK
* Correspondence: ahmed.elsheikh@eng.svu.edu.eg (A.E.); james.mcgregor@sheffield.ac.uk (J.M.)

Abstract: The direct use of ethanol in fuel cells presents unprecedented economic, technical, and environmental opportunities in energy conversion. However, complex challenges need to be resolved. For instance, ethanol oxidation reaction (EOR) requires breaking the rigid C–C bond and results in the generation of poisoning carbonaceous species. Therefore, new designs of the catalyst electrode are necessary. In this work, two trimetallic $Pd_xAg_yNi_z$/C samples are prepared using a facile borohydride reduction route. The catalysts are characterized by X-ray diffraction (XRD), Energy-Dispersive X-ray spectroscopy (EDX), X-ray photoelectron Spectroscopy (XPS), and Transmission Electron Microscopy (TEM) and evaluated for EOR through cyclic voltammetry (CV), chronoamperometry (CA), and electrochemical impedance spectroscopy (EIS). The XRD patterns have shown a weak alloying potential between Pd, and Ag prepared through co-reduction technique. The catalysts prepared have generally shown enhanced performance compared to previously reported ones, suggesting that the applied synthesis may be suitable for catalyst mass production. Moreover, the addition of Ag and Ni has improved the Pd physiochemical properties and electrocatalytic performance towards EOR in addition to reducing cell fabrication costs. In addition to containing less Pd, The PdAgNi/C is the higher performing of the two trimetallic samples presenting a 2.7 A/mg_{Pd} oxidation current peak. The $Pd_4Ag_2Ni_1$/C is higher performing in terms of its steady-state current density and electrochemical active surface area.

Keywords: intermetallic XRD patterns; alloy formation; ethanol electrooxidation; metal segregation; borohydride reduction; fuel cells

Citation: Elsheikh, A.; McGregor, J. Synthesis and Characterization of PdAgNi/C Trimetallic Nanoparticles for Ethanol Electrooxidation. *Nanomaterials* **2021**, *11*, 2244. https://doi.org/10.3390/nano11092244

Academic Editor: Eva Pellicer

Received: 28 July 2021
Accepted: 27 August 2021
Published: 30 August 2021

1. Introduction

Fuel cells are electrochemical energy conversion devices capable of converting the fuel chemical energy into electricity [1,2]. They possess multiple technical and environmental advantages considering the decaying fossil fuel resources and growing energy needs. Their operation is theoretically 100% efficient because they are not restricted by the Carnot thermal/mechanical energy conversion limitation of conventional heat engines [3]. Direct ethanol fuel cells (DEFCs) are fed with liquid ethanol instead of hydrogen. DEFCs are friendly to the environment and present high flexibility to supply diverse energy needs. As a liquid, ethanol is easy to store and transport and presents a high energy density (8 kWh/kg) [4–7]. Furthermore, it can be produced from biomass resources such as sugar cane, corn, and, more recently, from diverse agricultural and biomass wastes and residues which means it is sustainable and carbon-neutral [5]. Despite these advantages, the full commercialization of DEFCs is far from being realized. There are difficult-to-overcome challenges mainly in the form of cell fabrication costs. All low-temperature fuel cells need active noble metal (Pt) catalysts to push the fuel oxidation and oxidant reduction reactions forward. Another challenge is that most C-containing fuels generate CO–species during their oxidation. These poison catalytic sites and prevent further reaction, even if present only in low concentrations, e.g., 50 ppm [8,9]. Additionally, ethanol contains a strong C–C

bond thereby favoring its incomplete oxidation to acetate instead of CO_2 and releasing only 4 electrons instead of 12 [10,11]. Pt is very active for fuel cell electrocatalysis but is very expensive and scarce at the same time. Its expense can account for half of the cell fabrication [12]. There is, therefore, a need to find a Pt-alternative that presents comparable activity but also is more abundant to decrease the cell fabrication cost. Pd is more abundant than Pt and has shown a comparable performance for fuel cell electrocatalysis in alkaline electrolyte [13–15]. The fluctuating Pd and Pt prices are a complex phenomenon that involves technological, economic, and political contributions [16,17]. South Africa, Russia, Zimbabwe, Canada, and USA have Pd and Pt deposits. Prior to 1990, Pd was generally cheaper than Pt to mine and produce. However, with the advancement of Pd-based autocatalytic systems by the mid-90s, the demand and cost of Pd soared. By 2000, the price of Pd was much higher than that of Pt [18]. However, in 2007, the prices of Pt and Pd were reported $1450/ounce and $450/ounce, respectively [19]. Still, however, Pd is more attractive for automakers because it is not easy to switch back to Pt-catalytic converters. Furthermore, the diversity of Pd production by country and region is higher than that of Pt. South Africa, solely, controls Pt production while Pd mining capabilities are shared by Russia, South Africa, and North America [18]. This is an important factor due to the potential of a future shortage of Pt which is less likely in the case of Pd [20]. Another advantage of Pd over Pt in this particular EOR application is that it is more CO tolerant than Pt, however, Pt is more CO_2 selective than Pd [21]. To achieve a high-surface-area, Pd nanoparticles are dispersed on an inert, conducting, and porous material such as carbon black.

To further enhance the performance pf Pd and to decrease cell fabrication expenses, it is recommended to add another metal (or two) during the synthesis. The cocatalyst metal is expected to activate water and generate OH species to facilitate the oxidation of adsorbed ethoxy species. Moreover, it would modify the Pd geometry and electronic configuration and tune in its adsorption characteristics. Ni has been proven a beneficial cocatalyst when added to Pd because it can generate OH at a lower applied potential and modify the electronic structure of Pd [22–27]. The coexistence of Ni and $Ni(OH)_2$ can enhance alcohol oxidation on transition metals in acidic and basic electrolytes [6,28]. Feng et al. [29] prepared unsupported porous Pd and PdNi catalysts for ethanol electrooxidation sowing that PdNi exhibits enhanced electrocatalytic performance when compared to monometallic Pd. This enhancement is ascribed to the electronic and bifunctional effects of Ni. Zhang et al. [27] prepared various-proportion Pd_xNi_y/C catalysts for ethanol oxidation reaction. They found that Ni can generate oxygen species at lower applied potential, recovering Pd active sites and thus promoting ethanol oxidation, while through the microemulsion syntheis method it was possible to control PdNi particle size and make efficient contact between Pd and Ni. You et al. [30] prepared bimetallic PdAg dendrites with various composition and porous structure and evaluated them towards ethanol oxidation. Alloying between Pd and Ag shifts up the Pd d-band center leading to more tolerance for intermediates and poisons during EOR. Elsewhere, Li et al. [31] prepared PdAg nanoparticles supported on reduced graphene oxide (RGO), noting enhanced ethanol and methanol oxidation on PdAg when compared to Pd only. Oliveira et al. [32] prepared PdAg alloys and tested their efficacy for oxygen reduction reaction (ORR) and EOR. The kinetics of both reactions are promoted on PdAg as compared to Pd only. Additionally, the alloys maintained a higher selectivity for ORR in presence of ethanol. Similar conclusions on the benefits of adding Ag to Pd have been reported elsewhere [33,34].

In this work, trimetallic samples of C-supported PdAgNi nanoparticles are prepared, characterized, and evaluated for ethanol oxidation reaction (EOR) for the first time. Pd-based bimetallic nanocatalysts have been extensively investigated and reported for fuel cell electrocatalysis and EOR. Yet, a few groups have pursued the synthesis and application of C-supported trimetallic samples for similar purposes [35–43]. It is postulated that adding two metals is likely to provide benefits towards ethanol oxidation through altering Pd geometry, surface configuration, adsorption capacity, and coordination [35,37–39,44,45].

However, several factors such as the metal chemistry, synthesis method, reducing agent, and support structure may adversely affect the outcome. The ultimate objective is to design new electrodes that are cost-effective, EOR-active, CO-tolerant, and CO_2-selective.

2. Materials and Methods

The applied borohydride reduction synthesis method follows [46–48]. Table 1 shows the added precursor quantities of Vulcan carbon (XC72R), $PdCl_2$, $NiCl_2$, and $AgNO_3$ to prepare the monometallic and trimetallic samples. The theoretical metal loading was fixed at 12 Wt. %. The metal and carbon precursors were sonicated in a mixture of 2-propanol and water (50/50 *v*/*v*) for a few minutes. The theoretical Pd:Ag:Ni molar ratio is 57:28:15 and 34:33:33 for $Pd_4Ag_2Ni_1$/C and PdAgNi/C, respectively. The metallic salts were purchased from Sigma-Aldrich (Gillingham, United Kingdom) and the vulcan carbon precursor from Cabot Corp (Boston, MA, USA).

Table 1. Stochiometric added quantities of C, $PdCl_2$, $AgNO_3$, $NiCl_2$ to synthesize Pd/C. PdAgNi/C, and $Pd_4Ag_2Ni_1$/C.

Catalyst	C (mg)	$PdCl_2$ (mg)	$NiCl_2$ (mg)	$AgNO_3$ (mg)	Metal Wt. %
Pd/C	132	30			12
PdAgNi/C	132	11.7	8.5	11.2	12
$Pd_4Ag_2Ni_1$/C	132	18.3	3.4	8.8	12
Ag/C	132		40		12
Ni/C	132			28.3	12

KBr was added as a capping agent following the anion exchange method; the larger Br^- ion is capable of replacing the smaller Cl^- ion in the vicinity of Pd [49,50]. Consequently, Br^- ions can surround the recently reduced metal hindering its coalescence. The KBr/Metal atomic ratio was adjusted to 1.5. After that, the mixture was stirred for 10 min followed by adding the $NaBH_4$ solution (0.5 M, 15 mL) in one portion. Subsequently, the whole mixture was vigorously stirred for 30 min. Finally, the wet powder was dried at 80 °C in vacuum oven overnight.

X-ray diffraction (XRD) was undertaken to analyze the catalyst structure. The equipment is a Bruker D2 Phaser (Billerica, MA, USA) using Cu Kα radiation at 30 kV, 10 mA, and 12°/min scan-rate. The chemical composition of the catalysts was examined through energy-dispersive X-ray (EDX) spectroscopy conducted on a JEOL JSM 6010LA scanning electron microscope (SEM) (Akishima, Tokyo, Japan). Each catalyst surface was examined twice applying two different accelerating voltages: 10 kV and 20 kV. The different accelerating voltages change the interaction volume resulting from the electron beam-sample surface interaction. Thus, applying two different voltages enables the composition at two different depths to be studied [51]. Transmission electron microscopy (TEM) was undertaken to examine the catalyst surface morphology using a Phillips C100 microscope (Hillsboro, OR, USA) operating at 100 kV and equipped with a LaB6 filament. X-ray photoelectron spectroscopy (XPS) was applied to investigate the metal oxidation state and surface composition of the prepared electrocatalysts. A Thermo Scientific K-Alpha$^+$ spectrometer (Waltham, MA, USA) equipped with an Al-X ray source (72 W) was used. The pass energy to record the data was 150 eV for survey scans and 40 eV for high-resolution scans. The survey scan step size is 1 eV, and that of the high-resolution scans is 0.1 eV. Low-energy electrons and argon ions were used to neutralize the charge. CasaXPS (Teignmouth, UK) was used to analyze the data implementing a Shirley-type background and Scofield cross-sections with an energy dependence of −0.6.

The catalysts were evaluated for EOR via cyclic voltammetry (CV), chronoamperometry (CA), and electrochemical impedance spectroscopy (EIS). For this, a 3-electrode half-cell was used in which the working electrode is a glassy carbon electrode (GCE, Ø 3mm) coated with each catalyst ink. The reference and counter electrodes were Ag/AgCl (sat' KCL) and Pt wire, respectively. The applied potential is converted to normal hydrogen electrode

(NHE). A Gamry 600 portable Station from Gamry Instruments Inc. (Warminster, PA, USA) was used to perform the electrochemical evaluation. The catalyst ink was prepared by dispersing 5 mg of its powder in 25 µL (Nafion® 117, 5%) and 2000 µL of ethanol (100%). The mixture was then sonicated for 1 h. Before drop-casting the working electrode with ink, it was polished with alumina powder (1 and 0.05 µm, respectively) to produce a mirror-like surface. Then, 25 µL of the ink was painted on GCE at 5 µL intervals.

3. Results

3.1. Physical Characterization

X-ray Diffraction (XRD)

Figure 1 shows the XRD patterns of Pd/C, Ni/C, Ag/C, PdAgNi/C, and $Pd_4Ag_2Ni_1$/C. The 25° peak present in all patterns is attributed to the semi-crystalline graphitic nature of Vulcan carbon. For the Ni pattern, the metal peaks are of lower intensity than the carbon peaks as Ni is present in the form of hydroxide and oxide, indicated by peaks at 34°, 60°, and 42.5°, respectively. The Ag pattern, on the other hand, shows the (111), (200), (231), (220), and (311) reflections at 38°, 44°, 46°, 65°, and 77°, respectively resembling a face-centered cubic Ag (JCPDS card, File No. 04-0783) [52]. A similar Ag pattern has been obtained previously [31]. The Pd pattern presents (111), (200), (220), and (311) reflections located at 39.8°, 46°, 76.7°, and 82.2° indicative of Pd (JCPDS card, File No. 46-1043). Considering the XRD patterns of both trimetallic samples, it can be noted that a significant peak overlapping occurs. The high intensity peaks present at lower-angles align well with the pure Ag peak positions, whereas the lower-intensity, broader, peaks at higher-angles align with the peak positions of Pd. Monometallic Ni/C shows $Ni(OH)_2$ and Ni (111) peaks at 34.5°, 60.1°, and 42.7°, respectively.

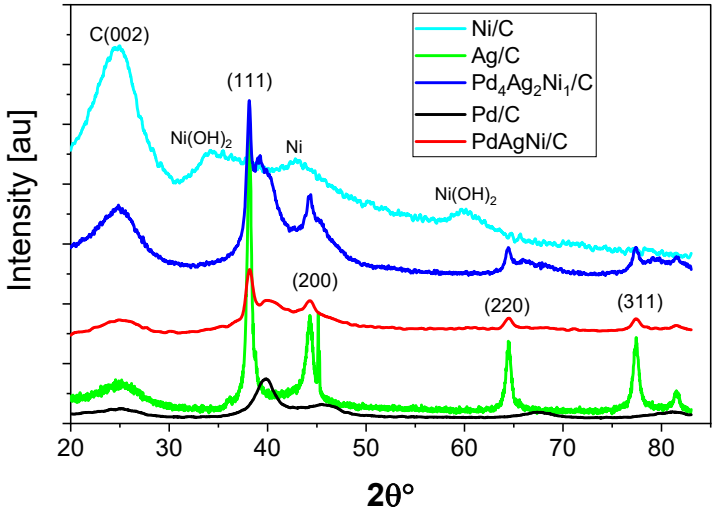

Figure 1. X-ray diffraction patterns of Pd/C, Ag/C, Ni/C, PdAgNi/C, and $Pd_4Ag_2Ni_1$/C.

3.2. Energy Dispersive X-ray Spectroscopy (EDX)

Table 2 lists the elemental metal molar and weight compositional ratios of PdAgNi/C and $Pd_4Ag_2Ni_1$/C. While the average total metal loading of $Pd_4Ag_2Ni_1$/C as measured by EDX is close to the theoretical loading at ~12 wt. %, it is slightly higher (16 wt. %) in the case of PdAgNi/C. As EDX is a surface-weighted technique, this indicates the preferential distribution of metal in the surface region of the catalyst. Furthermore, higher Ni atomic concentrations are observed at 10 kV than at 20 kV indicating the preference of Ni to be distributed in the near-surface region.

Table 2. EDX elemental metal composition of PdAgNi/C and $Pd_4Ag_2Ni_1$/C detected at 20 kV and 10 kV voltages.

Catalyst	Acc. Voltage	Pd		Ni		Ag		Tot. Metal Wt. %
		Wt. % *	At. % **	Wt. %	At. %	Wt. %	At. %	
$Pd_4Ag_2Ni_1$/C	10 kV	7.89	1.02	1.64	0.38	1.98	0.25	11.51
	20 kV	8.28	1.09	1.10	0.26	3.26	0.42	12.46
PdAgNi/C	10 kV	6.47	0.88	7.68	1.90	3.39	0.46	17.54
	20 kV	6.92	0.94	5.04	1.24	4.10	0.55	16.06

* wt. %: weight percentage %; ** at. %: atomic percentage %.

The PdAgNi/C surface can therefore be considered as relatively rich in Ni, while for $Pd_4Ag_2Ni_1$/C the Ni content in the surface region is comparable to that of Ag even though the theoretical Ni quantity in the bulk sample is half of that of Ag. Figure 2 shows the elemental EDX maps of Pd, Ni, Ag, and C in both PdAgNi/C and $Pd_4Ag_2Ni_1$/C. Examining the maps of $Pd_4Ag_2Ni_1$/C (A–D) shows that the carbon support and metal species are evenly dispersed across the catalyst surface.

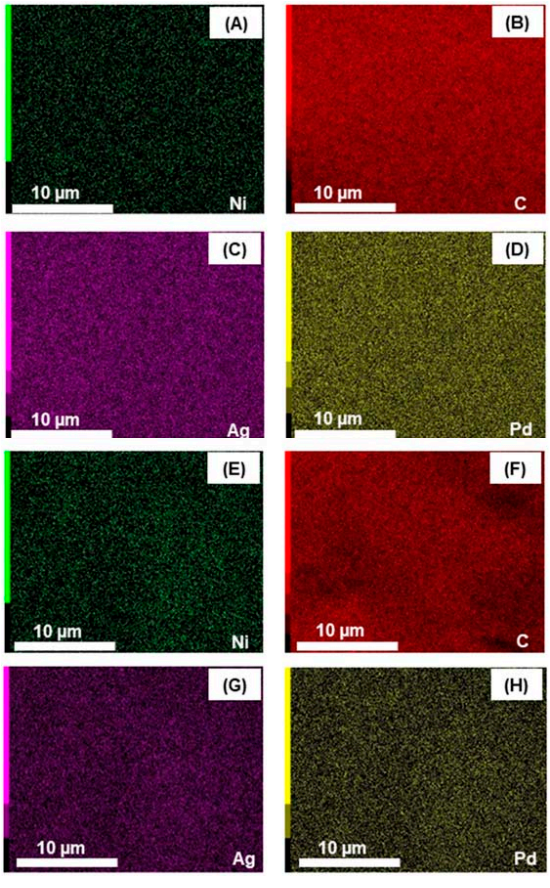

Figure 2. EDS elemental maps of $Pd_4Ag_2Ni_1$/C (**A**–**D**) and PdAgNi/C (**E**–**H**) taken at 10 kV.

3.3. Transmission Electron Microscopy (TEM)

Figure 3 shows TEM micrographs (A, C, D) of Pd/C, $Pd_4Ag_2Ni_1$/C, and PdAgNi/C. The respective particle size distribution is, also, shown (B, D, F). From inspection of the

Pd/C micrograph, it can be noted that Pd nanoparticles (average size 6.7 nm) are dispersed over larger carbon aggregates (40–60 nm). Additionally, some particle agglomeration can be noted. The particle size distribution was measured by manually selecting the metal particles through use of ImageJ software. The average particle size and standard deviation of Pd/C are 6.7 and 5 nm, respectively. The high standard deviation value is suggestive of the high variation in particle size as a consequence of high particle agglomeration. In contrast, the average particle size of $Pd_4Ag_2Ni_1/C$ is 5.6 nm and the standard deviation to 2.7 nm. This is possibly due to the contradicting forces that affect the particle aggregation during both nucleation and growth. It is extensively reported that preparing multi-metallic samples results in different attraction and repulsion forces and, therefore, smaller particle sizes [22,24,41,53–56]. The same trend is noted in PdAgNi, which has a smaller total quantity of Pd; in this case the average particle size and standard deviations are 4.4 nm and 3 nm, respectively.

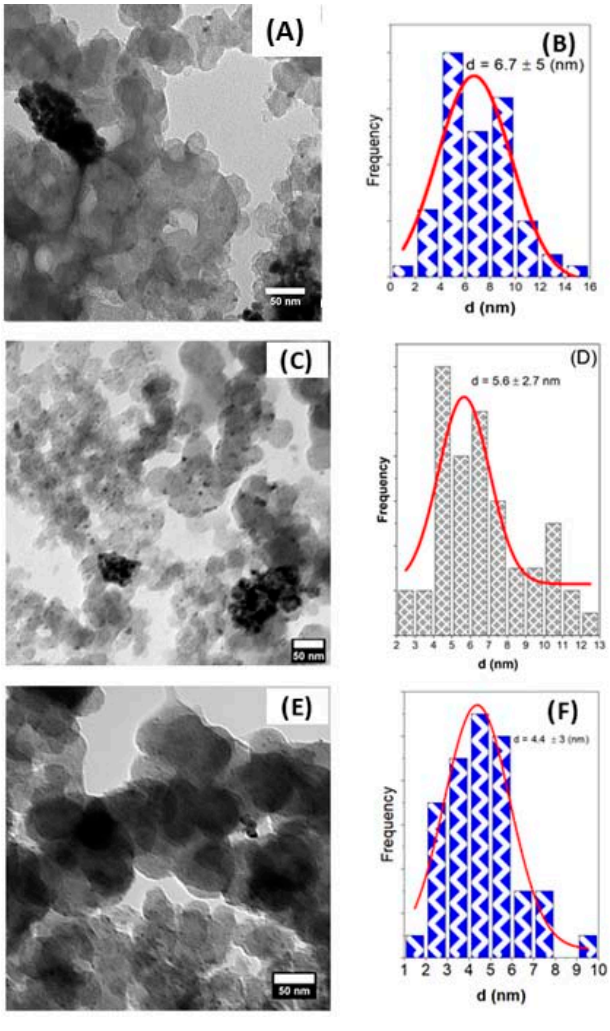

Figure 3. TEM Micrographs and the respective particle size distribution of Pd/C (**A**,**B**), $Pd_4Ag_2Ni_1/C$ (**C**,**D**), and PdAgNi/C (**E**,**F**).

3.4. X-ray Photoelectron Spectroscopy (XPS)

XPS analysis was undertaken to investigate the metal oxidation state and surface composition of the samples. Figure 4 shows the XPS full survey scans of Pd/C, PdAgNi/C, and $Pd_4Ag_2Ni_1$/C. The C1s, Pd 3d, Ag 3d, Pd 3p (overlapping with O 1s), and Ni 2p are located approximately at 284, 335, 370, 532, and 856 eV, respectively.

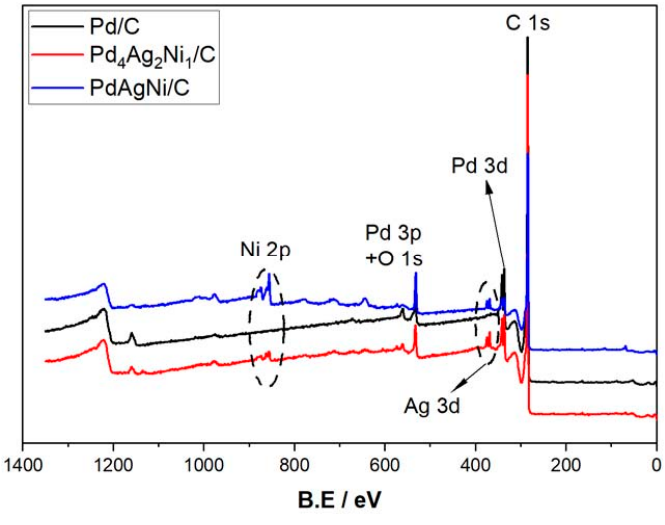

Figure 4. XPS full surveys of Pd/C, $Pd_4Ag_2Ni_1$/C, and PdAgNi/C.

Figure 5 shows the detailed elemental peaks of Pd 3d, Ag 3d, and Ni 2p in Pd/C, $Pd_4Ag_2Ni_1$/C, and PdAgNi/C. The Pd 3d of Pd/C (A) is deconvoluted into a high-energy band (340.4 eV) of Pd $3d_{3/2}$and a low-energy band (335.48 eV) of Pd $3d_{5/2}$. Additionally, the PdO peaks are visible around 342 eV and 337 eV. Table 3 lists the XPS surface concentrations of C, O, Pd, Ag, and Ni for the three samples. The XPS surface concentration Pd of Pd/C is 1.63 At. % and 0.45% for Pd^0 and Pd^{2+}, respectively. The presence of Pd oxide is indicative of Pd air instability which could be improved by adding another metal. PdAgNi/C also presents a significant fraction of Pd^{2+}—16% of the total Pd present. $Pd_4Ag_2Ni_1$/C however, with a lower overall Pd content, presents only metallic Pd^0, as shown in Figure 5D. The Ag 3d double-peak is located at 374 and 368 eV for $3d_{3/2}$ and $3d_{5/2}$ (Figure 5E), respectively. The Ni 2p peaks of Ni^0 and Ni^{+2} of $Pd_4Ag_2Ni_1$/C are present at 852, 856, and 862 eV (Figure 5D), respectively, with no visible satellite peaks. The Ni XPS surface concentration of that sample is 0.05 at. % (for metallic Ni) and 0.73 at. % (for $Ni(OH)_2$).

Table 3. XPS surface atomic concentration of C, O, Pd, Ag, and Ni in Pd/C, $Pd_4Ag_2Ni_1$/C, and PdAgNi/C.

Catalyst	C At. %	O at. %	Pd at. %		Ag at. %	Ni at. %		Pd:Ag:Ni Ratio
			Pd^0	Pd^{2+}		Ni^0	Ni^{2+}	
Pd/C	96.13	1.78	1.63	0.45				
$Pd_4Ag_2Ni_1$/C	93.91	3.14	1.59	0	0.4	0.05	0.73	4:1:2
PdAgNi/C	92.15	4.69	0.64	0.12	0.32	0	2.01	2.7: 1:6.7

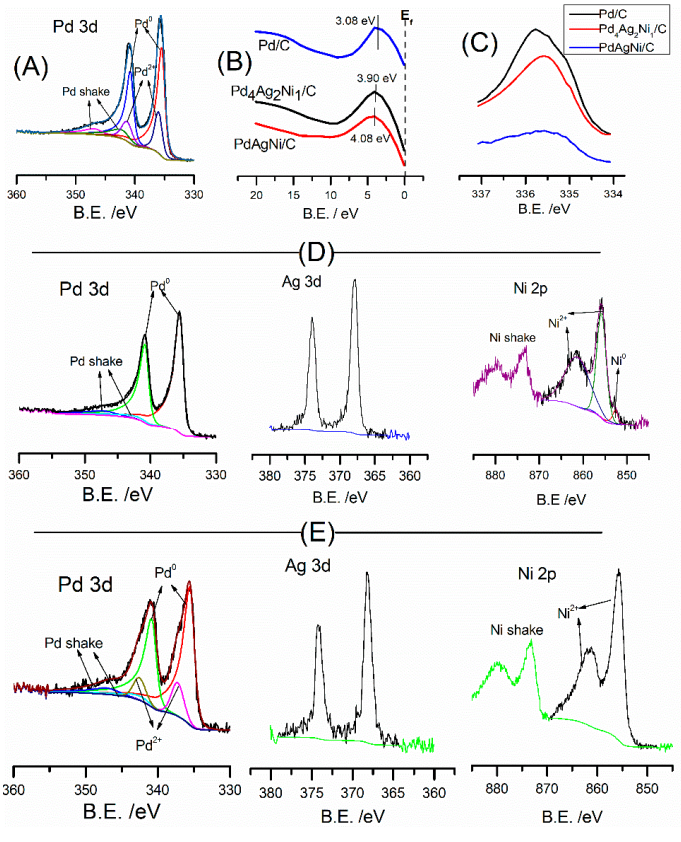

Figure 5. XPS elemental peaks of Pd 3d in in Pd/C (**A**), valence band spectra (**B**) and Pd $3d_{5/2}$ (**C**) of Pd/C, $Pd_4Ag_2Ni_1$/C, and PdAgNi/C, Pd 3d, Ag 3d, Ni 2p, of $Pd_4Ag_2Ni_1$/C (**D**) and PdAgNi/C (**E**).

3.5. Electrochemical Evaluation

Figure 6 shows the cyclic voltammograms of Pd/C, PdAgNi/C, and $Pd_4Ag_2Ni_1$/C performed in 1M KOH at 50 mV/s. It is noteworthy that the thinnest profile is observed for Pd/C. This is indicative of a thinner double-layer, and consequently, faster charging/discharging behavior for Pd/C [42]. As Pd is known to absorb hydrogen within its bulk, the $H_{abs/ads}$ peak in the forward scan at ~−600 mV is not present. This peak is, however, more pronounced on both trimetallic samples, which may be ascribed to the presence of Ag. Upon increasing the potential, the OH adsorption peak between −400 and −200 mV is more apparent for monometallic Pd/C than for the trimetallic samples. OH adsorption can be considered as the onset of surface oxidation, however oxidation of Pd commences at approximately 0.0 mV vs. NHE. Ag surface oxidation is noted at ~470 mV followed by Ni oxidation up to the scan end at 600 mV. Both Ni and Ag oxidation peaks are more pronounced for PdAgNi/C than for $Pd_4Ag_2Ni_1$/C as the former contains higher quantities of Ni and Ag. In the reverse scan, distinctive reduction peaks for Ni, Ag, and Pd appear at 450, 220, and −200 mV, respectively. A small shoulder on the Pd reduction peak is noted for $Pd_4Ag_2Ni_1$/C and Pd/C which is not clear for PdAgNi/C. This is likely to be reflective of the reduction of different Pd oxides.

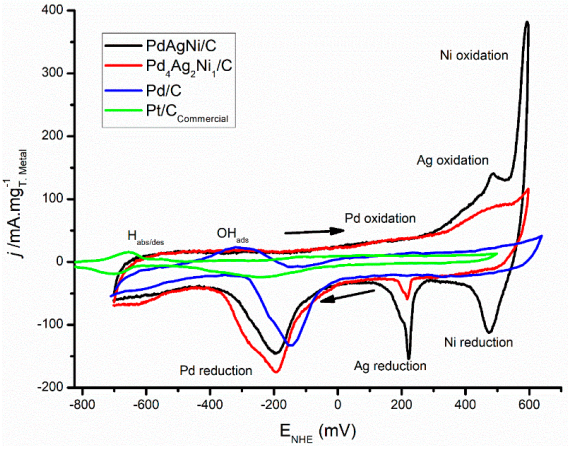

Figure 6. CV voltammograms of Pd/C, $Pd_4Ag_2Ni_1/C$, and PdAgNi/C in 1M KOH at 50 mV/s.

Figure 7 shows the cyclic voltammograms of the three catalysts in 1M KOH+EtOH at 50 mV. The addition of ethanol suppresses the $H_{ands/abs}$ peak as reported elsewhere [55,57]. With the start of OH adsorption, adsorbed ethoxy species undergo oxidation and are removed from Pd sites, thereby making these sites available for further fuel oxidation. As the adsorbed OH increases with increasing potential, the free Pd sites increase, and an increasing current is drawn. While the onset oxidation potential in case of Pd/C is −390 mV, it is shifted to −500 mV in case of PdAgNi/C and $Pd_4Ag_2Ni_1/C$ which suggests a reduction in the activation barrier against ethanol oxidation on the surface of both trimetallic samples. A similar shift in potential is noted for the oxidation peak on PdAgNi sample compared to Pd. The peak current density in case of PdAgNi/C (2700 mA/m_{gPd}) is higher than $Pd_4Ag_2Ni_1/C$ (2300 mA/m_{gPd}) and the smallest peak current density is of Pd/C (1.8 A/m_{gPd}).

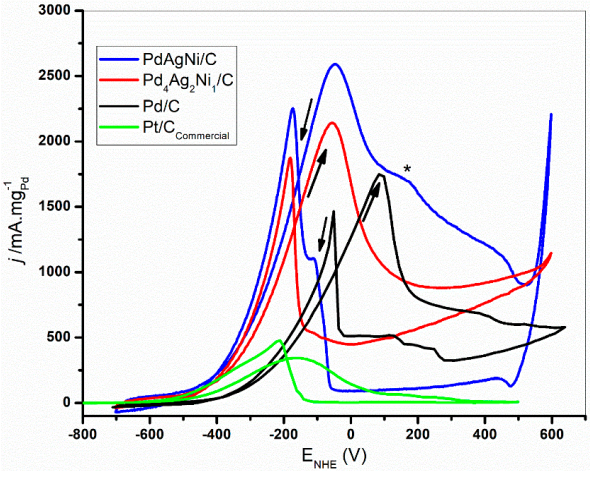

Figure 7. CV Voltammograms of Pd/C, $Pd_4Ag_2Ni_1/C$, and Pd/C in 1 M KOH+EtOH at 50 mV/s.

When the catalyst surface can no longer adsorb OH, the surface Pd oxides thereby decreasing the number of Pd active sites as the potential increases. This ultimately decreases the drawn current up to the end of the forward scan. It is noteworthy that around the forward current peak, the reactants are depleted much faster than at the beginning of the

scan [8]. A shoulder peak is noted on PdAgNi/C at 200 mV which may be suggestive of the oxidation of ethoxy intermediates on Pd. At the end of the PdAgNi forward scan, a sharp current rise is noted due to the Ni oxidation that also appears in the voltammogram conducted in the absence of ethanol. The sharp peak in the inverse scan is due to the removal of the incompletely oxidized intermediates from EOR and recovery of Pd active sites. It is noteworthy that the forward sweep current peak is higher than the reverse one on all catalysts which is a positive indication of the ability of the catalyst to tolerate poisoning species [58,59]. Therefore, CO-like species are less likely to block further EOR on the catalysts developed in the present work.

Figure 8 shows the chronoamperometric scans of Pd/C, $Pd_4Ag_2Ni_1$/C, and PdAgNi/C performed at fixed potentials of −300 mV and +100 mV vs. NHE. The former was chosen because it is in the middle of the window in which OH was adsorbed causing the oxidation and removal of ethoxy species from Pd surface. The latter was chosen because it is greater than the potential at which the Pd surface oxidation starts. These data show that the CA current density of PdAgNi/C sample—though higher than that of $Pd_4Ag_2Ni_1$/C at the two CA steps—decays much faster at the higher-potential (+0.1 V) to the extent that it drops below $Pd_4Ag_2Ni_1$/C towards the end of the CA duration. According to EDX and XPS, the surface of PdAgNi/C is Ni-rich and correspondingly deficient in Pd and Ag. PdAgNi/C, therefore, presents fewer accessible Pd surface sites for EOR than Pd/C or $Pd_4Ag_2Ni_1$/C. During the high-potential CA scan, the number of available Pd sites further decreases through site poisoning via the strong adsorption of EOR intermediates. The PdAgNi voltammograms (Figures 6 and 7) show that OH adsorption does not continue at +0.1 V. Therefore, at high potential, PdAgNi/C is susceptible to poisoning by carbonaceous species from EOR. In contrast, $Pd_4Ag_2Ni_1$/C generates a steadier CA current density than PdAgNi/C at +0.1 V; which is ascribed to the higher concentration of Pd in the surface region for the former, providing a greater number of available Pd sites and hence greater resistance to poisoning. Pd/C achieves an intermediate current decay between PdAgNi/C and $Pd_4A_g2Ni_1$/C which could be explained by two factors: the strong adsorption of CO-like species and the abundance of Pd surface sites.

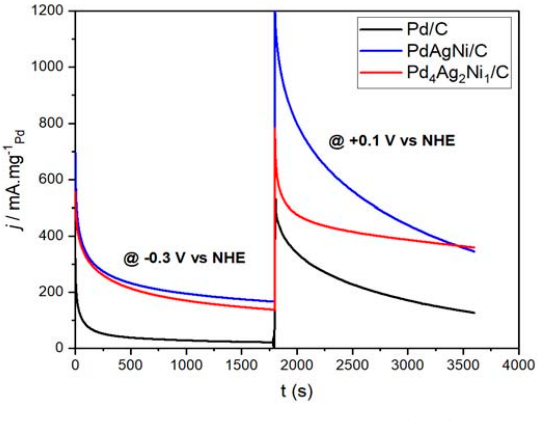

Figure 8. Chronoamperometric (CA) scans of Pd/C, $Pd_4Ag_2Ni_1$/C, PdAgNi/C at −0.3 V and +0.1 V vs. NHE.

Figure 9 shows the EIS spectra of $Pd_4Ag_2Ni_1$/C, and PdAgNi/C recorded at −0.3 V, 0.0 V, and +0.3 V vs. NHE between 10,000 Hz and 0.1 Hz while the voltage amplitude is 5 mV. Each experiment was preceded with a 10-min potentiostatic scan to compensate for the current perpetuation. EIS spectra at −0.3 V and 0.0 V represent, to some extent, a semi-circle due to the interchangeable interaction of the double-layer capacitance through the electrolyte-electrode interface and the charge-transfer resistance. However, at +0.3 V, the effect of charge-transfer resistance is such that with further decreasing frequency, the

arc continues to rise vertically. This is a consequence of more than one factor. For instance, increasing the applied potential affects the charge-transfer resistance more significantly than the double-layer capacitance. Moreover, at +0.3 V no further EOR occurs due to the Pd surface oxidation and current decrease (Figure 7). It is noteworthy the arc size at −0.3 V and 0.0 V of $Pd_4Ag_2Ni_1/C$ is slightly smaller than their counterparts of PdAgNi/C.

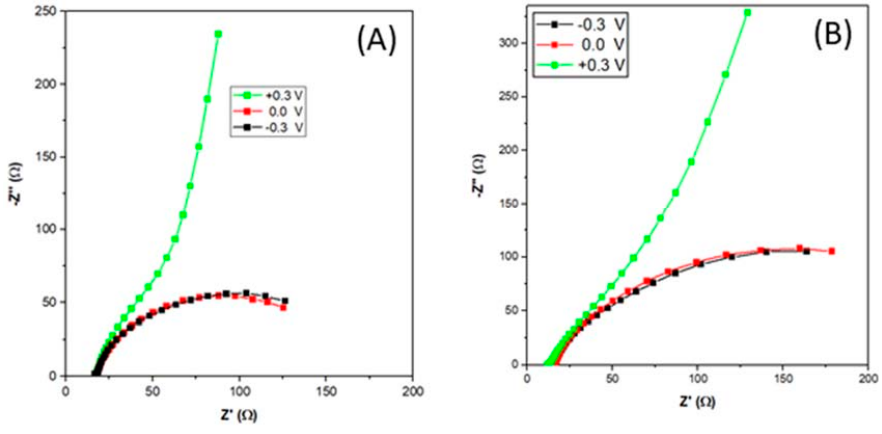

Figure 9. Electrochemical impedance spectroscopy (EIS) of $Pd_4Ag_2Ni_1/C$ (**A**) and PdAgNi/C (**B**) at −0.3 V, 0.0 V, and 0.3 V vs. NHE.

Gamry Echem Analyst software was used to construct an electrical model (Figure 10) that represents the physical phenomena contributing to the impedance. R_s represents the solution resistance measured at the intersection point with the *x*-axis (−Z″= 0, frequency = 10 kHz) and for both catalysts, it is approximately 14 Ω and does not change with the applied potential. The constant-phase element (Ø) represents the double-layer capacitance effect due to opposite-charge accumulation at the electrode-electrolyte interface. R_{ct} represents the charge-transfer resistance that reflects on the specific activity of each catalyst. R_{ct} values of $Pd_4Ag_2Ni_1/C$ are estimated to be 150 Ω and 183 Ω at −0.3 V and 0.0 V vs. NHE, respectively. Larger values of 285 Ω and 290 Ω—at the same respective potentials—are obtained with PdAgNi/C. This further demonstrates the improved performance of $Pd_4Ag_2Ni_1/C$ towards EOR when compared to PdAgNi/C. It is difficult to estimate the R_{ct} value at +0.3 V due to the complex phenomena encountered and missing EOR at such high potential and several EIS models were inaccurate enough to estimate reasonable R_{ct} values at that potential.

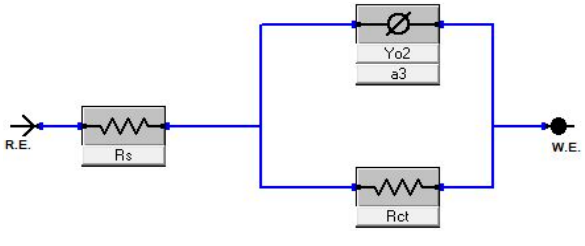

Figure 10. EIS electrical model representative of the physical quantities in a half-cell 3-electrode.

4. Discussion

The XRD peak separation of Pd and Ag (Figure 1) implies that there is substantial separation of Pd and Ag in the nanoparticles and therefore that it is less likely a nanoalloy has been formed. Separate Ag and Pd peaks were also reported by other researchers [31,60], while other groups have found singular peaks that resemble both Pd and Ag [30,39,61].

Olivera et al. [32] annealed electrolessly deposited Pd and Ag films on steel discs to produce Pd-Ag alloy films. Before annealing, distinctive Pd and Ag phases were detected by XRD, with a single peak observed after annealing. The $Ni(OH)_2$ individual peak disappearance in the XRD patterns of both trimetallic samples is suggestive of a high degree of mixing between Pd and Ni whose atoms could be assumed incorporated into the Pd lattice. The separate peaks of $Ni(OH)_2$ are commonly seen when synthesizing bimetallic and trimetallic Ni-containing catalysts [22,29,53–55,62,63]. The surface metal loading of PdAgNi/C (16 wt. %), as measured by ESX, is 4 wt. % higher than the nominal bulk loading (Table 1), with Ni segregating to the surface. The opposite trend is noted for Ag which segregates into the catalyst core. The Pd: Ag: Ni molar ratio at 10 kV is 4:1:2 while it is 4:1.6:1 at 20 kV which shows the Pd concentration does not change significantly with analysis depth, but the Ag and Ni ones do. A similar observation is noted for PdAgNi/C whose Pd:Ag:Ni at 10 kV is 2:1:4 while it is 1.75:1:2.25 at 20 kV.

According to the XPS measurements (Table 3), Ag is present exclusively in the metallic state with a concentration of 0.4 at. % and 0.32 at. % for $Pd_4Ag_2Ni_1/C$ and PdAgNi/C, respectively. This is despite the theoretical Ag loading being lower in $Pd_4Ag_2Ni_1/C$ (Table 1). It is noteworthy that XPS atomic Pd:Ag:Ni ratio is 4:1:2 while the ratio from surface-weighted EDX spectroscopy measurements (Table 2) is 4.4:1.7:1. The higher Ni XPS proportion signifies its segregation into the top surface unlike Ag. In PdAgNi/C, which has a lower fraction of Pd than $Pd_4Ag_2Ni_1/C$, the Pd air stability is lost and 15% of Pd exists in an oxidized form (Figure 5E) Figure 5G shows the Ni 2p peak of PdAgNi/C and two satellite peaks which are potentially due to the multiple Ni excitations. No metallic Ni was detected for this sample and the Ni surface concentration equals 2.01 at.%. Therefore, the XPS-derived Pd:Ag:Ni molar ratio is 2.7:1:6.7 while the EDX spectroscopy derived ratio (Table 2) is 1.7:2.3:1. Once again this is probably due to the Ni tendency to segregate into the surface and Ag and little Pd tendency to segregate into the core. In case of trimetallic samples, the Pd 3d peak is shifted 0.05 eV (Figure 5C) to higher binding energy than Pd/C, which may be suggestive of an electron loss from Pd to either Ag or Ni. Figure 5C shows the valence band of Pd/C, $Pd_4Ag_2Ni_1/C$, and PdAgNi/C which indicates the *d*-band center of the two trimetallic samples are shifted approximately 1 eV from the Fermi level compared to their monometallic counterpart. Note that the impact of particle size on *d*-band center can be neglected as the particle size is ~5 nm and instead shifts in the *d*-band center are the consequence of charge transfer from Pd to other metals [35,64].

As $H_{abs/des}$ peak is missing in Figure 6, it is more appropriate to estimate electrochemical active surface area (ECSA) using the PdO reduction peak in the reverse scan. The PdO reduction area in the reverse scan is the smallest in case of Pd/C while higher reduction currents are obtained with PdAgNi/C and $Pd_4Ag_2Ni_1/C$. The PdO reduction peak is used as a measure of the Pd fraction exposed on the surface, and therefore, available to undertake redox reactions. The electrochemical active surface area (ECSA, cm^2/mg) is calculated according to [26]:

$$ECSA = \frac{Q}{0.43 \times [Pd]}$$

where Q is the charge extracted from PdO reduction peaks in mC, 0.43 mC/cm^2 is the monolayer reduction charge of Pd, and [Pd] is the weight of Pd on GCE in mg. This indicates ECSA is highest on $Pd_4Ag_2Ni_1/C$ followed by PdAgNi/C and finally Pd/C (Table 4). This could be explained by the smaller particle size of both trimetallic samples compared to the monometallic one according to TEM (Figure 3). The three catalysts have very significantly larger ECSAs compared to the other materials listed in Table 4. This is indicative of the high Pd surface fraction; although Ni has a higher tendency to segregate into the surface as shown by EDX and XPS analyses. The low overall metal loading (12 wt. %) decreases the overall metal surface energies and aggregation potential leading to a thicker and rougher catalyst layer, while the KBr capping works against agglomeration by surrounding the individual nanoparticles during synthesis with Br^{-1} ions. The ethanol-enhanced CV performance on both trimetallic samples is a reflection of

the Ag and Ni effects. This indicates that more EOR Pd active sites exist on the trimetallic sample surfaces than on Pd/C. A similar finding was previously reported regarding the activity of PdAgNi towards formic acid oxidation [39]. The lower oxidation onset potentials and higher forward current peak are advantageous for the three samples in this work compared to many other previously published catalysts [58,65–67]. Table 4 compares the EOR onset oxidation current density and current peak obtained with this work catalysts and previously published ones. The reverse current peak of Pd/C, $Pd_4Ag_2Ni_1$/C, and PdAgNi/C are smaller than their forward counterparts. This is indicative of a good Pd tolerance towards the poisoning species. When o_f/j_b is >1, it implies less incompletely oxidized ethoxy intermediates on Pd surface which suggests the catalyst is more likely to recover its surface-active sites and proceed with further EOR. When it is <1, it suggests there are more incompletely-oxidized carbonaceous species on the catalyst surface that are strongly bound to active sites. Adding Ni to the Pd-based catalyst has, in some previous works, resulted in j_f/j_b decreasing below 1 [29,43], although other works observe the opposite trend [42,54,68].

Table 4. Comparison of the ECSA (cm^2/mg), E_{onset} (mV) and j_p (A/mg_{Pd}) in 1M EtOH of this work and previously published catalysts.

Catalyst	ECSA (cm^2/mg)	E_{onset} (mV) vs. NHE	j_p (A/mg_{Pd})	Ref.
Pd/C	1350	−390	1.8	This work
PdAgNi/C	1500	−500	2.7	
$Pd_4Ag_2Ni_1$/C	1618	−500	2.3	
Pd/C	549	−150	0.5	[54]
$Pd_{83}Ni_{17}$	375	−250	1.1	
PdNi	209	−260	1.45	[29]
Pd	135	−209	0.8	
Pd_1Au_1/C	1320	−260	12	[68]
Pd/C		−260	0.75	
$Pd_2Sn_2Ag_1$/C	243	−360	0.8	[42]
$Pd_2Sn_2Ni_1$/C	209	−330	0.4	
$Pd_2Sn_2Co_1$/C	212	−300	0.35	
PdAgCu	506	−360	4.56	[43]
Pd/C		−350	1.47	[21]
Pt/C		−400	0.65	

It should be noted the chronoamperometric currents drawn on trimetallic catalysts (Figure 8) are substantially higher than that on Pd/C which suggests a higher catalyst capability to recover the Pd active sites by generating OH species which indicates the addition of Ag and Ni is beneficial for EOR catalytic performance. The catalyst containing the least Pd (PdAgNi/C) draws the highest current density (−0.3 V). This implies that this surface is highly active for the generation of oxygen species, facilitating the removal of adsorbed ethoxy species. Ni surface segregation and Ag core segregation, as determined through EDX spectroscopy and XPS, may in part explain the enhanced V-*j* behavior of PdAgNi/C. A somewhat similar behavior is noted for the other trimetallic sample. Note, however, that a very high level of OH adsorption on the catalyst surface would negatively impact the overall catalyst performance as many of the EOR-active surface sites would be occupied by OH.

The enhanced the performance of the trimetallic catalysts in the present work is likely due to Ni and Ag generating OH species resulting in the larger ECSA for both samples as shown in Figure 6. The current density drawn on three catalysts at +0.1 V is higher than at

−0.3 V due to the increased activation voltage and OH adsorption. It is also noteworthy that at −0.3 V vs. NHE, the three catalysts exhibit similar behavior in terms of the current decays as the scan proceeds. However, at −0.1 V vs. NHE, $Pd_4Ag_2Ni_1/C$ shows better stability (stable current decay) than PdAgNi/C even though the former draws a higher current for the majority of the 30-min scan. Although the initial current decay at −0.3 V is similar on both $Pd_4Ag_2Ni_1/C$ and PdAgNi/C, at +0.1 V the current decay rate is higher for PdAgNi/C than for $Pd_4Ag_2Ni_1/C$ and the former draws a higher current at the scan end. Several factors likely contribute to this enhanced performance upon adding both Ag and Ni. For instance, the activation barrier of EOR on both trimetallic samples less than that on Pd/C due to the reduction of the bandgap energy, indicated by the smaller activation overvoltage [8]. Also, the large number of active sites verified by the smaller TEM particle size in the case of both trimetallic samples, will play a positive role. Another factor that may contribute to the observed higher ESCA values as compared to previous studies is that the experiment was performed with the electrolyte being stirred. This may help to ensure the uniform distribution of reactants/products and reduce the effects of mass transport and diffusion.

Compared to many reported synthesis methods, the currently applied method is quicker and easier because it is a room-temperature one-pot synthesis. Furthermore, it was concluded in a short time (30 min). Many of the previous synthesis protocols include use of high temperature and/or longer synthesis times [29,42,43,54,68]. Also, the smaller metal loading in the present work is potentially beneficial for the physical and electrochemical characteristics of the supported catalyst. Additionally, it is noted that Ni tends to segregate into the surface while Ag tends to segregate into the bulk of trimetallic particles. Furthermore, the trimetallic catalysts are cost-effective than those consisting only of platinum-group metals. The collective characterization and evaluation results suggest that $Pd_4Ag_2Ni_1/C$ is the best performing catalyst and that adding a significant Ni quantity (>35 At. %) would adversely impact the catalyst physical and electrocatalytic performance

5. Conclusions

C-supported PdAgNi intermetallic catalysts have been successfully prepared through a straight-forward chemical synthesis method suitable for up-scaling for the first time. Adding small quantity of Ni in trimetallic catalysts has a beneficial impact but increasing the Ni content can harm the EOR performance. A relatively low metal loading (12 Wt. %) and adding KBr as a capping agent are recommended to produce a well-dispersed catalyst with a high electrochemical surface area (ECSA). However, the followed protocol does not produce a highly order alloy structure of Pd and Ag as indicated by XRD. Although the $Pd_4Ag_2Ni_1/C$ surpassed the PdAgNi/C in terms of ECSA and ethanol oxidation potential, the latter outperformed it in terms of the oxidation current peak and steady chronoamperometric current. Adding Ag and Ni to Pd not only improves its catalytic performance towards EOR, but considerably decreases the catalyst preparation cost. While Ag tends to segregate to the bulk of the PdAgNi nanoparticle, Ni tends to segregate to its outer surface layers. $Pd_4Ag_2Ni_1/C$ combines both high activity and stability towards EOR.

Author Contributions: Conceptualization, A.E. and J.M.; methodology, A.E.; software, A.E.; validation, J.M. and A.E.; investigation, A.E.; resources, J.M.; data curation, A.E.; writing—original draft preparation, A.E.; writing—review and editing, J.M. All authors have read and agreed to the published version of the manuscript.

Funding: Ahmed Elsheikh is grateful for the financial support of Newton-Mosharafa Fund (Reference No. NMJ8/15) of his Ph.D.

Data Availability Statement: Not applicable.

Acknowledgments: XPS data collection was performed at the EPSRC National Facility for XPS ('HarwellXPS'), operated by Cardiff University and UCL, under contract No. PR16195.

Conflicts of Interest: The authors declare there is no conflict of interest related to this work.

References

1. Katsounaros, I.; Koper, M.T.M. *Electrocatalysis for the hydrogen economy, In Electrochemical Science for a Sustainable Society*; A Tribut. to John O'M Bockris; Springer International Publishing: Basel, Switzerland, 2017; pp. 23–50. [CrossRef]
2. Stamenkovic, V.R.; Strmcnik, D.; Lopes, P.; Markovic, N.M. Energy and fuels from electrochemical interfaces. *Nat. Mater.* **2017**, *16*, 57–69. [CrossRef]
3. O'Hayre, R.; Cha, S.-W.; Colella, W.; Prinz, F.B. *Prinz, Fuel Cell Fundamentals*; John Wiley & Sons, Inc.: Hoboken, NJ, USA, 2016. [CrossRef]
4. Friedl, J.; Stimming, U. Model catalyst studies on hydrogen and ethanol oxidation for fuel cells. *Electrochim. Acta* **2013**, *101*, 41–58. [CrossRef]
5. Badwal, S.; Giddey, S.; Kulkarni, A.; Goel, J.; Basu, S. Direct ethanol fuel cells for transport and stationary applications—A comprehensive review. *Appl. Energy* **2015**, *145*, 80–103. [CrossRef]
6. Bianchini, C.; Shen, P.K. Palladium-Based Electrocatalysts for Alcohol Oxidation in Half Cells and in Direct Alcohol Fuel Cells. *Chem. Rev.* **2009**, *109*, 4183–4206. [CrossRef] [PubMed]
7. An, L.; Zhao, T.; Li, Y. Carbon-neutral sustainable energy technology: Direct ethanol fuel cells. *Renew. Sustain. Energy Rev.* **2015**, *50*, 1462–1468. [CrossRef]
8. O'Hayre, R.; Cha, S.; Colella, W.; Prinz, F.B. Chapter 3: Fuel Cell Reaction Kinetics. In *Fuel Cell Fundam*; John Wiley & Sons, Inc.: Hoboken, NJ, USA, 2016; pp. 77–116. [CrossRef]
9. O'Hayre, F.B.P.R.; Cha, S.; Colella, W.; O'Hayre, R.; Cha, S.-W.; Colella, W.; Prinz, F.B. Chapter 8: Overview of Fuel Cell Types. In *Fuel Cell Fundam*; John Wiley & Sons, Inc.: Hoboken, NJ, USA, 2016; pp. 269–302. [CrossRef]
10. Guo, J.; Chen, R.; Zhu, F.-C.; Sun, S.-G.; Villullas, H.D.L.M. New understandings of ethanol oxidation reaction mechanism on Pd/C and Pd2Ru/C catalysts in alkaline direct ethanol fuel cells. *Appl. Catal. B Environ.* **2018**, *224*, 602–611. [CrossRef]
11. Kamarudin, M.; Kamarudin, S.; Masdar, M.S.; Daud, W.R.W. Review: Direct ethanol fuel cells. *Int. J. Hydrog. Energy* **2013**, *38*, 9438–9453. [CrossRef]
12. Antolini, E. Palladium in fuel cell catalysis. *Energy Environ. Sci.* **2009**, *2*, 915–931. [CrossRef]
13. Antolini, E.; Gonzalez, E. Alkaline direct alcohol fuel cells. *J. Power Sources* **2010**, *195*, 3431–3450. [CrossRef]
14. Merle, G.; Wessling, M.; Nijmeijer, K. Anion exchange membranes for alkaline fuel cells: A review. *J. Membr. Sci.* **2011**, *377*, 1–35. [CrossRef]
15. Brouzgou, A.; Podias, A.; Tsiakaras, P. PEMFCs and AEMFCs directly fed with ethanol: A current status comparative review. *J. Appl. Electrochem.* **2013**, *43*, 119–136. [CrossRef]
16. Sverdrup, H.U.; Ragnarsdottir, K.V. A system dynamics model for platinum group metal supply, market price, depletion of extractable amounts, ore grade, recycling and stocks-in-use. *Resour. Conserv. Recycl.* **2016**, *114*, 130–152. [CrossRef]
17. Khan, K.; Köseoğlu, S.D. Is palladium price in bubble? *Resour. Policy* **2020**, *68*, 101780. [CrossRef]
18. Hagelüken, C. Markets for the catalyst metals platinum, palladium and rhodium. *Metall* **2006**, *60*, 31–42.
19. Company news. *Solder. Surf. Mt. Technol.* **2012**, *24*, 433–434. [CrossRef]
20. Platinum, V.S. Palladium: A Key Factor Holding Back Platinum Demand and Price | Seeking Alpha. Available online: https://seekingalpha.com/article/4270121-platinum-vs-palladium-key-factor-holding-back-platinum-demand-and-price (accessed on 24 January 2021).
21. Ma, L.; Chu, D.; Chen, R. Comparison of ethanol electro-oxidation on Pt/C and Pd/C catalysts in alkaline media. *Int. J. Hydrog. Energy* **2012**, *37*, 11185–11194. [CrossRef]
22. Amin, R.; Hameed, R.A.; El-Khatib, K.; Youssef, M.E. Electrocatalytic activity of nanostructured Ni and Pd–Ni on Vulcan XC-72R carbon black for methanol oxidation in alkaline medium. *Int. J. Hydrog. Energy* **2014**, *39*, 2026–2041. [CrossRef]
23. Sheikh, A.M.; Silva, E.L.; Moares, L.; Antonini, L.M.; Abellah, M.Y.; Malfatti, C.F. Pd-based Catalysts for Ethanol Oxidation in Alkaline Electrolyte. *Am. J. Min. Metall.* **2014**, *2*, 64–69. [CrossRef]
24. Obradović, M.; Stančić, Z.; Lacnjevac, U.; Radmilovic, V.; Gavrilovic-Wohlmuther, A.; Gojković, S. Electrochemical oxidation of ethanol on palladium-nickel nanocatalyst in alkaline media. *Appl. Catal. B Environ.* **2016**, *189*, 110–118. [CrossRef]
25. Jongsomjit, S.; Sombatmankhong, K.; Prapainainar, P. Effect of acid functionalised carbon supports for Pd–Ni–Sn catalyst on ethanol oxidation reaction. *RSC Adv.* **2015**, *5*, 61298–61308. [CrossRef]
26. Moraes, L.; Matos, B.; Radtke, C.; Santiago, E.; Fonseca, F.C.; Amico, S.; Malfatti, C. Synthesis and performance of palladium-based electrocatalysts in alkaline direct ethanol fuel cell. *Int. J. Hydrog. Energy* **2016**, *41*, 6457–6468. [CrossRef]
27. Zhang, Z.; Xin, L.; Sun, K.; Li, W. Pd–Ni electrocatalysts for efficient ethanol oxidation reaction in alkaline electrolyte. *Int. J. Hydrog. Energy* **2011**, *36*, 12686–12697. [CrossRef]
28. Hassaninejad-Darzi, S.K.; Gholami-Esfidvajani, M. Electrocatalytic oxidation of ethanol using modified nickel phosphate nanoparticles and multi-walled carbon nanotubes paste electrode in alkaline media for fuel cell. *Int. J. Hydrog. Energy* **2016**, *41*, 20085–20099. [CrossRef]
29. Feng, Y.; Bin, D.; Yan, B.; Du, Y.; Majima, T.; Zhou, W. Porous bimetallic PdNi catalyst with high electrocatalytic activity for ethanol electrooxidation. *J. Colloid Interface Sci.* **2017**, *493*, 190–197. [CrossRef] [PubMed]
30. Jo, Y.-G.; Kim, S.-M.; Kim, J.-W.; Lee, S.-Y. Composition-tuned porous Pd-Ag bimetallic dendrites for the enhancement of ethanol oxidation reactions. *J. Alloy. Compd.* **2016**, *688*, 447–453. [CrossRef]

31. Li, L.; Chen, M.; Huang, G.; Yang, N.; Zhang, L.; Wang, H.; Liu, Y.; Wang, W.; Gao, J. A green method to prepare Pd–Ag nanoparticles supported on reduced graphene oxide and their electrochemical catalysis of methanol and ethanol oxidation. *J. Power Sources* **2014**, *263*, 13–21. [CrossRef]
32. Oliveira, M.; Rego, R.; Fernandes, L.S.G.; Tavares, P. Evaluation of the catalytic activity of Pd–Ag alloys on ethanol oxidation and oxygen reduction reactions in alkaline medium. *J. Power Sources* **2011**, *196*, 6092–6098. [CrossRef]
33. Qi, J.; Benipal, N.; Liang, C.; Li, W. PdAg/CNT catalyzed alcohol oxidation reaction for high-performance anion exchange membrane direct alcohol fuel cell (alcohol = methanol, ethanol, ethylene glycol and glycerol). *Appl. Catal. B Environ.* **2016**, *199*, 494–503. [CrossRef]
34. Lam, B.T.X.; Chiku, M.; Higuchi, E.; Inoue, H. Preparation of PdAg and PdAu nanoparticle-loaded carbon black catalysts and their electrocatalytic activity for the glycerol oxidation reaction in alkaline medium. *J. Power Sources* **2015**, *297*, 149–157. [CrossRef]
35. Hu, S.; Munoz, F.; Noborikawa, J.; Haan, J.; Scudiero, L.; Ha, S. Carbon supported Pd-based bimetallic and trimetallic catalyst for formic acid electrochemical oxidation. *Appl. Catal. B Environ.* **2016**, *180*, 758–765. [CrossRef]
36. Beyhan, S.; Léger, J.-M.; Kadırgan, F. Understanding the influence of Ni, Co, Rh and Pd addition to PtSn/C catalyst for the oxidation of ethanol by in situ Fourier transform infrared spectroscopy. *Appl. Catal. B Environ.* **2014**, *144*, 66–74. [CrossRef]
37. Shang, C.; Hong, W.; Wang, J.; Wang, E. Carbon supported trimetallic nickel-palladium-gold hollow nanoparticles with superior catalytic activity for methanol electrooxidation electrooxidation. *J. Power Sources.* **2015**, *85*, 12–15. [CrossRef]
38. Sharma, G.; Kumar, D.; Kumar, A.; Al-Muhtaseb, A.; Pathania, D.; Naushad, M.; Mola, G.T. Revolution from monometallic to trimetallic nanoparticle composites, various synthesis methods and their applications: A review. *Mater. Sci. Eng. C* **2017**, *71*, 1216–1230. [CrossRef]
39. Ulas, B.; Caglar, A.; Sahin, O.; Kivrak, H. Composition dependent activity of PdAgNi alloy catalysts for formic acid electrooxidation. *J. Colloid Interface Sci.* **2018**, *532*, 47–57. [CrossRef] [PubMed]
40. Shen, S.; Zhao, T.; Xu, J.; Li, Y. High performance of a carbon supported ternary PdIrNi catalyst for ethanol electro-oxidation in anion-exchange membrane direct ethanol fuel cells. *Energy Environ. Sci.* **2011**, *4*, 1428–1433. [CrossRef]
41. Su, P.-C.; Chen, H.-S.; Chen, T.-Y.; Liu, C.-W.; Lee, C.-H.; Lee, J.-F.; Chan, T.-S.; Wang, K.-W. Enhancement of electrochemical properties of Pd/C catalysts toward ethanol oxidation reaction in alkaline solution through Ni and Au alloying. *Int. J. Hydrog. Energy* **2013**, *38*, 4474–4482. [CrossRef]
42. Zhu, F.; Wang, M.; He, Y.; Ma, G.; Zhang, Z.; Wang, X. A comparative study of elemental additives (Ni, Co and Ag) on electrocatalytic activity improvement of PdSn-based catalysts for ethanol and formic acid electro-oxidation. *Electrochim. Acta* **2014**, *148*, 291–301. [CrossRef]
43. Lv, H.; Sun, L.; Zou, L.; Xu, D.; Yao, H.; Liu, B. Electrode for proton exchange membrane fuel cells: A review. *Chem. Sci.* **2019**, *10*, 1986–1993. [CrossRef]
44. Gebre, S.H.; Sendeku, M.G. Trimetallic nanostructures and their applications in electrocatalytic energy conversions. *J. Energy Chem.* **2022**, *65*, 329–351. [CrossRef]
45. Zhu, W.; Ke, J.; Wang, S.-B.; Ren, J.; Wang, H.-H.; Zhou, Z.-Y.; Si, R.; Zhang, Y.-W.; Yan, C.-H. Shaping Single-Crystalline Trimetallic Pt–Pd–Rh Nanocrystals toward High-Efficiency C–C Splitting of Ethanol in Conversion to CO_2. *ACS Catal.* **2015**, *5*, 1995–2008. [CrossRef]
46. Nandenha, J.; De Souza, R.; Assumpção, M.; Spinacé, E.V.; Neto, A.O. Preparation of PdAu/C-Sb_2O_5·SnO_2 electrocatalysts by borohydride reduction process for direct formic acid fuel cell. *Ionics* **2013**, *19*, 1207–1213. [CrossRef]
47. Neto, A.O.; Tusi, M.M.; Polanco, N.S.D.O.; da Silva, S.G.; dos Santos, M.C.; Spinacé, E.V. PdBi/C electrocatalysts for ethanol electro-oxidation in alkaline medium. *Int. J. Hydrog. Energy* **2011**, *36*, 10522–10526. [CrossRef]
48. Assumpção, M.; da Silva, S.; De Souza, R.; Buzzo, G.; Spinacé, E.; Santos, M.; Neto, A.; Silva, J. Investigation of PdIr/C electrocatalysts as anode on the performance of direct ammonia fuel cell. *J. Power Sources* **2014**, *268*, 129–136. [CrossRef]
49. Antoniassi, R.; Silva, J.C.; Neto, A.O.; Spinacé, E. Synthesis of Pt+SnO2/C electrocatalysts containing Pt nanoparticles with preferential (100) orientation for direct ethanol fuel cell. *Appl. Catal. B Environ.* **2017**, *218*, 91–100. [CrossRef]
50. Naresh, N.; Wasim, F.G.S.; Ladewig, B.P.; Neergat, M. Removal of surfactant and capping agent from Pd nanocubes (Pd-NCs) using tert-butylamine: Its effect on electrochemical characteristics. *J. Mater. Chem. A* **2013**, *1*, 8553–8559. [CrossRef]
51. Leng, Y. X-ray Spectroscopy for Elemental Analysis. In *Materials Characterization*; John Wiley & Sons, Ltd.: Chichester, UK, 2008; pp. 171–196. [CrossRef]
52. Meng, Y. A Sustainable Approach to Fabricating Ag Nanoparticles/PVA Hybrid Nanofiber and Its Catalytic Activity. *Nanomaterials* **2015**, *5*, 1124–1135. [CrossRef]
53. Ramulifho, T.; Ozoemena, K.I.; Modibedi, R.M.; Jafta, C.; Mathe, M. Fast microwave-assisted solvothermal synthesis of metal nanoparticles (Pd, Ni, Sn) supported on sulfonated MWCNTs: Pd-based bimetallic catalysts for ethanol oxidation in alkaline medium. *Electrochim. Acta* **2012**, *59*, 310–320. [CrossRef]
54. Zhu, C.; Wen, D.; Oschatz, M.; Holzschuh, M.; Liu, W.; Herrmann, A.-K.; Simon, F.; Kaskel, S.; Eychmüller, A. Kinetically Controlled Synthesis of PdNi Bimetallic Porous Nanostructures with Enhanced Electrocatalytic Activity. *Small* **2015**, *11*, 1430–1434. [CrossRef]
55. Dutta, A.; Datta, J. Energy efficient role of Ni/NiO in PdNi nano catalyst used in alkaline DEFC. *J. Mater. Chem. A* **2014**, *2*, 3237–3250. [CrossRef]

56. Dutta, A.; Datta, J. Outstanding Catalyst Performance of PdAuNi Nanoparticles for the Anodic Reaction in an Alkaline Direct Ethanol (with Anion-Exchange Membrane) Fuel Cell. *J. Phys. Chem. C* **2012**, *116*, 25677–25688. [CrossRef]
57. Armenta-González, A.J.; Carrera-Cerritos, R.; Guerra-Balcázar, M.; Arriaga, L.G.; Ledesma-García, J. Comparative study of carbon-supported Pd and PdAg catalysts synthesised by the polyol process and reverse micelles methods. *J. Appl. Electrochem.* **2014**, *45*, 33–41. [CrossRef]
58. Chen, L.Y.; Chen, N.; Hou, Y.; Wang, Z.C.; Lv, S.H.; Fujita, T.; Jiang, J.H.; Hirata, A.; Chen, M.W. Geometrically Controlled Nanoporous PdAu Bimetallic Catalysts with Tunable Pd/Au Ratio for Direct Ethanol Fuel Cells. *ACS Catal.* **2013**, *3*, 1220–1230. [CrossRef]
59. Zalineeva, A.; Serov, A.; Padilla, M.; Martinez, U.; Artyushkova, K.; Baranton, S.; Coutanceau, C.; Atanassov, P. Nano-structured Pd-Sn catalysts for alcohol electro-oxidation in alkaline medium. *Electrochem. Commun.* **2015**, *57*, 48–51. [CrossRef]
60. Adekoya, J.; Dare, E.; Mesubi, M.; Nejo, A.A.; Swart, H.; Revaprasadu, N. Synthesis of polyol based Ag/Pd nanocomposites for applications in catalysis. *Results Phys.* **2014**, *4*, 12–19. [CrossRef]
61. Zhang, Y.; Yi, Q.; Deng, Z.; Zhou, X.; Nie, H. Excellent Electroactivity of Ternary Pd–Ag–Sn Nanocatalysts for Ethanol Oxidation. *Catal. Lett.* **2018**, *148*, 1190–1201. [CrossRef]
62. Wei, Y.-C.; Liu, C.-W.; Kang, W.-D.; Lai, C.-M.; Tsai, L.-D.; Wang, K.-W. Electro-catalytic activity enhancement of Pd–Ni electrocatalysts for the ethanol electro-oxidation in alkaline medium: The promotional effect of CeO_2 addition. *J. Electroanal. Chem.* **2011**, *660*, 64–70. [CrossRef]
63. Wang, Y.; Jiang, K.; Cai, W.-B. Enhanced Electrocatalysis of Ethanol on Dealloyed Pd-Ni-P Film in Alkaline Media: An Infrared Spectroelectrochemical Investigation. *Electrochim. Acta* **2015**, *162*, 100–107. [CrossRef]
64. Pan, B.; Chen, F.; Kou, B.; Wang, J.; Tang, Q.; Guo, L.; Wang, Q.; Li, Z.; Bian, W.; Wang, J. Unexpectedly high stability and surface reconstruction of PdAuAg nanoparticles for formate oxidation electrocatalysis. *Nanoscale* **2020**, *12*, 11659–11671. [CrossRef] [PubMed]
65. Chen, X.-M.; Lin, Z.-J.; Jia, T.-T.; Cai, Z.-M.; Huang, X.-L.; Jiang, Y.-Q.; Chen, X.; Chen, G.-N. A facile synthesis of palladium nanoparticles supported on functional carbon nanotubes and its novel catalysis for ethanol electrooxidation. *Anal. Chim. Acta* **2009**, *650*, 54–58. [CrossRef]
66. Correa, P.D.S.; Da Silva, E.L.; Da Silva, R.F.; Radtke, C.; Moreno, B.; Chinarro, E.; Malfatti, C. Effect of decreasing platinum amount in Pt–Sn–Ni alloys supported on carbon as electrocatalysts for ethanol electrooxidation. *Int. J. Hydrog. Energy* **2012**, *37*, 9314–9323. [CrossRef]
67. Habibi, E.; Bidad, E.; Feizbakhsh, A.; Fazli, M. Comparative electrooxidation of C1–C4 alcohols on Pd | CC nanoparticle anode catalyst in alkaline medium. *Int. J. Hydrog. Energy* **2014**, *39*, 18416–18423. [CrossRef]
68. Feng, Y.-Y.; Liu, Z.-H.; Xu, Y.; Wang, P.; Wang, W.-H.; Kong, D.-S. Highly active PdAu alloy catalysts for ethanol electro-oxidation. *J. Power Sources* **2013**, *232*, 99–105. [CrossRef]

nanomaterials

MDPI

Article

Carbon-Supported Trimetallic Catalysts (PdAuNi/C) for Borohydride Oxidation Reaction

Ahmed M. A. ElSheikh [1,2,†], Gordana Backović [3,†], Raisa C. P. Oliveira [3], César A. C. Sequeira [3], James McGregor [2], Biljana Šljukić [3] and Diogo M. F. Santos [3,*]

[1] Mechanical Engineering Department, South Valley University, AlShobaan AlMoslemeen Street, Qena 83521, Egypt; ahmed.elsheikh@eng.svu.edu.eg
[2] Department of Chemical and Biological Engineering, University of Sheffield, Sheffield S1 3JD, UK; james.mcgregor@sheffield.ac.uk
[3] Center of Physics and Engineering of Advanced Materials (CeFEMA), Instituto Superior Técnico, Universidade de Lisboa, 1049-001 Lisboa, Portugal; gordanabackovic@tecnico.ulisboa.pt (G.B.); raisa.oliveira@tecnico.ulisboa.pt (R.C.P.O.); cesarsequeira@tecnico.ulisboa.pt (C.A.C.S.); biljana.paunkovic@tecnico.ulisboa.pt (B.Š.)
* Correspondence: diogosantos@tecnico.ulisboa.pt; Tel.: +351-218417765
† Equally contributed.

Abstract: The synthesis of palladium-based trimetallic catalysts via a facile and scalable synthesis procedure was shown to yield highly promising materials for borohydride-based fuel cells, which are attractive for use in compact environments. This, thereby, provides a route to more environmentally friendly energy storage and generation systems. Carbon-supported trimetallic catalysts were herein prepared by three different routes: using a $NaBH_4$-ethylene glycol complex (PdAuNi/C_{SBEG}), a $NaBH_4$-2-propanol complex (PdAuNi/C_{SBIPA}), and a three-step route (PdAuNi/$C_{3\text{-step}}$). Notably, PdAuNi/C_{SBIPA} yielded highly dispersed trimetallic alloy particles, as determined by XRD, EDX, ICP-OES, XPS, and TEM. The activity of the catalysts for borohydride oxidation reaction was assessed by cyclic voltammetry and RDE-based procedures, with results referenced to a Pd/C catalyst. A number of exchanged electrons close to eight was obtained for PdAuNi/$C_{3\text{-step}}$ and PdAuNi/C_{SBIPA} (7.4 and 7.1, respectively), while the others, PdAuNi/C_{SBEG} and Pd/C_{SBIPA}, presented lower values, 2.8 and 1.2, respectively. A direct borohydride-peroxide fuel cell employing PdAuNi/C_{SBIPA} catalyst in the anode attained a power density of 47.5 mW cm^{-2} at room temperature, while the elevation of temperature to 75 °C led to an approximately four-fold increase in power density to 175 mW cm^{-2}. Trimetallic catalysts prepared via this synthesis route have significant potential for future development.

Keywords: palladium; trimetallic catalysts; nanoparticle; borohydride oxidation; direct borohydride peroxide fuel cell; kinetic parameters

Citation: ElSheikh, A.M.A.; Backović, G.; Oliveira, R.C.P.; Sequeira, C.A.C.; McGregor, J.; Šljukić, B.; Santos, D.M.F. Carbon-Supported Trimetallic Catalysts (PdAuNi/C) for Borohydride Oxidation Reaction. *Nanomaterials* **2021**, *11*, 1441. https://doi.org/10.3390/nano11061441

Academic Editor: Stefano Agnoli

Received: 4 May 2021
Accepted: 24 May 2021
Published: 29 May 2021

1. Introduction

Fuel cells (FCs) are electrochemical energy conversion devices with superior performance compared to conventional internal combustion engines, as they are not limited by the Carnot cycle [1]. Additionally, FCs are more environmentally friendly than conventional energy generation processes since they generally do not generate carbon dioxide (with few exceptions, such as direct alcohol/formic acid FCs) and do not rely on the consumption of fossil resources. Consequently, FC research and development has grown linearly with the worldwide energy demand and is projected to increase as FCs replace conventional heat engines in various applications [2]. However, many challenges need to be overcome if mass uptake of fuel cells is to be realized, including issues of safety, fuel source, and ensuring high efficiencies at low operating temperatures.

Low-temperature FCs targeted for use in portable applications and, particularly, for use in the transportation area have recently undergone rapid development [3]. They are

compact, lightweight, and can attain high power densities. Polymer electrolyte membrane fuel cell (PEMFC), the most developed FC, most commonly comprises an H_2-supplied anode and an O_2-supplied cathode separated by a polymeric membrane. Nevertheless, employing H_2 as fuel presents several challenges to widespread adoption, including safety, storage, and supply. Furthermore, H_2-stream pretreatment is usually required in order to remove trace carbon monoxide, which poisons the electrode. To address these issues, H_2/O_2 PEMFCs can be replaced with direct liquid fuel cells (DLFCs). DLFCs can use organic and inorganic liquid fuels, which usually incorporate a supporting electrolyte in their composition [4].

Solutions of complex hydrides (e.g., $LiBH_4$, $NaBH_4$, or KBH_4) are examples of hydrogen-containing compounds that can be used as fuels in DLFCs. Sodium borohydride ($NaBH_4$) presents many advantages over other fuels. The open-circuit voltage (OCV) for the direct borohydride fuel cell (DBFC, 1.64 V) is higher than that of the direct methanol fuel cell (DMFC, 1.21 V) and the H_2/O_2 PEMFC (1.23 V). While the oxidation of H_2 and methanol generates two and six electrons, respectively, per molecule, BH_4^- direct oxidation generates eight electrons. Consequently, DBFC possesses specific energy over 50% higher than that of the DMFC [5]. Indig and Snyder [6] demonstrated in the 1960s that electricity could be produced via anodic oxidation of borohydride and O_2 cathodic reduction, as shown in Equation (1) and Equation (2), respectively, to yield the overall fuel cell reaction (Equation (3)), where SHE stands for standard hydrogen electrode.

$$\text{BOR} \quad NaBH_4 + 8\,OH^- \rightarrow NaBO_2 + 6\,H_2O + 8\,e^- \qquad E^0 = -1.24 \text{ vs. SHE} \tag{1}$$

$$\text{ORR} \quad 2\,O_2 + 4\,H_2O + 8\,e^- \rightarrow 8\,OH^- \qquad E^0 = 0.40 \text{ vs. SHE} \tag{2}$$

$$\text{Overall} \quad NaBH_4 + 2\,O_2 \rightarrow NaBO_2 + 2\,H_2O \qquad E_0 = 1.64 \text{ V} \tag{3}$$

Many authors have discussed the advantages, disadvantages, and state-of-the-art in DBFCs, including postulating the replacement of O_2 by hydrogen peroxide (H_2O_2) [7–10]. The use of H_2O_2 as an oxidant has become more popular in recent years, in particular as this results in an entirely liquid FC, thereby facilitating its use in applications where a compact design is required. When H_2O_2 is used as the oxidant, the catholyte consists of an acidic solution of H_2O_2 in order to avoid its decomposition into H_2O and O_2. Consequently, the DBFC in which the hydrogen peroxide reduction reaction (HPRR) takes place at the cathode and the BOR at the anode is known as the direct borohydride-peroxide fuel cell (DBPFC). It can generate electricity through Equations (1) and (4), with Equation (5) being the overall FC reaction.

$$\text{HPRR} \quad H_2O_2 + 2e^- + 2H^+ \rightarrow 2\,H_2O \qquad E^0 = 1.78 \text{ V vs. SHE} \tag{4}$$

$$\text{Overall} \quad NaBH_4 + 4H_2O_2 \rightarrow NaBO_2 + 6H_2O \qquad E^0 = 3.01 \text{ V vs. SHE} \tag{5}$$

The majority of published research on DBFCs discusses the need for effective and low-cost anode and cathode materials in order to facilitate the commercialization of DBFCs. This is a result of the high operating costs of the DBFC, which is correlated with the performance, efficiency, and cost of the electrocatalysts [5,8–11]. In fact, anodic catalysts for DBFCs must have high catalytic activity for BOR and be inert towards BH_4^- hydrolysis, a chemical side reaction where BH_4^- is consumed, generating H_2 and BO_2^-. In addition, DBFC anodes need to exhibit chemical stability in a basic solution. Common anodic catalysts for DBFCs include noble metal catalysts such as Au [12–16], Pt [17–20], and their corresponding alloy materials [21–24], as well as some nonprecious metal catalysts, e.g., Ni [25,26], Zn [27], and Co [28–30]. In particular, Au has been extensively studied, as it was originally thought to be capable of inhibiting borohydride hydrolysis; however, it exhibits rather slow kinetics for borohydride oxidation [31,32]. Studies involving Au, Pd, and Pt bulk electrodes for BOR revealed that surface poisoning by reaction intermediates, including BH_{ads} or BH_3, was significantly different for the three noble metals. Results have shown that this effect was more severe for Pt and also that the Au surface was the

least affected by poisoning [33]. Despite this observation, Pt-based catalysts typically demonstrate faster electrode kinetics in BOR [24,34,35]; however, limited resources hinder their application as DBFC anodic catalysts. Pd is a promising alternative to Pt, presenting similar chemical properties and reactivity. Pd is considerably more abundant in the Earth's crust than Pt (ca. fifty times) and hence presents fewer challenges regarding resource scarcity [36–38]. Therefore, Pd has been tested in FCs both as a cocatalyst with Pt and as a Pt-free catalyst [37,39–41]. Decreasing the required quantity of Pd by mixing it with non-noble metals in a well-designed catalytic structure capable of efficient borohydride oxidation can decrease the cost of membrane electrode assemblies (MEAs) and boost the commercialization of DBFCs. It was previously found that co-doping can improve the catalytic performance of noble metal catalysts [42–44]. For example, a Pd-Co/C nanocatalyst has been demonstrated as an electrocatalyst for formic acid oxidation and methanol oxidation [45,46].

Previous studies reported Pd nanocatalysts and Pd nanoalloys as anodic catalysts for BOR in DBFCs [47,48]. Furthermore, Simões et al. [49] analyzed how Pd, Au, and Pd-Au carbon-supported nanoparticles with different compositions performed during BOR in alkaline media. Pd_xAu_{1-x}/C electrocatalyst exhibited an open circuit potential (OCP) lower than Pd and Au did. Merino-Jimenez et al. [50] evaluated a titanium-supported and carbon nanofiber-covered Pd-Ir alloy for BOR. The authors concluded that alloying Pd with Ir improves Pd electroactivity towards BOR. This enhancement was associated with the favoring of BOR (direct oxidation) and suppression of hydrogen evolution reaction (HER). Furthermore, Grimmer et al. [51] studied BOR at Pd/C by cyclic voltammetry, rotating disc electrode (RDE) measurements, chronoamperometry coupled to NMR spectrometry, and in situ Fourier transform infrared spectroscopy (FTIR). RDE results yielded n = 4 (at 0.4 V vs. reversible hydrogen electrode (RHE)) and n = 8 (at 0.8 V vs. RHE). Thus, at 0.8 V vs. RHE, BOR is 100% direct, while at 0.4 V, two different pathways are proposed to operate: (i) the total oxidation of BH_4^- to BO_2^- and two H_2 molecules and (ii) a four-electron electrooxidation with the production of BH_2^- species. The authors also suggested that at low potentials, Pd-BH_2OH species block surface sites, while at higher potentials, this intermediate is fully oxidized (n = 8). Additionally, Pd has been shown to be relatively unharmed by surface poisoning, preserving good BOR kinetics even in highly concentrated BH_4^- solutions relevant for DBPFC operation [33]. Recently, by screening selected metal combinations (e.g., Pd with Co, Au, Ti) over a wide range of compositions, bimetallic and trimetallic Pd-based materials with optimum compositions that exhibited good activity for BOR were identified [51–56]. According to multiple published reports, Ni presents several benefits when added as a cocatalyst to C-supported Pd. First, it is an Earth-abundant metal, and therefore its use tackles issues of resource scarcity and reduces cost. Secondly, it is oxyphilic and capable of generating the oxygen species necessary for the redox reaction. Finally, the presence of Ni can exert an electronic effect over Pd, altering and potentially enhancing the catalytic properties of the latter [57–59].

In this work, investigations on the oxidation of BH_4^- in alkaline media at different working conditions are presented for a selection of trimetallic carbon-supported catalysts based on Pd (PdAuNi/C), prepared by a facile and scalable synthetic route. There is a consensus that adding a second metal as a cocatalyst to Pd is beneficial for its electrocatalytic performance. This is due to the electronic, geometric, and bifunctional effects that the second metal can provide. Previous works have considered multiplying the catalytic benefits by adding two metals to Pd instead of one [56,60–66]. It is hypothesized that adding two metals, such as Au and Ni, each of which is known to be a beneficial addition to Pd individually [67–69], would significantly enhance Pd electrocatalytic performance. A small number of previous studies have previously investigated PdAuNi electrocatalysts [67–72]. Au [12,73–77] and Ni [25,78–80], like Pd, have been proven to possess good catalytic activity towards BOR, which makes their incorporation in a catalyst additionally attractive. Specifically, in the case of Ni electrodes, the formation of β-NiOOH has been pointed out as essential for the oxidation of BH_4^- [26]. Furthermore, to maximize the potential for

BOR, a high-surface inert, mesoporous, and conductive support material is necessary to anchor the trimetallic nanoparticles and prevent their coalescence. Vulcan carbon (XC-72R) is commonly applied for this application due to its high surface area, mesoporous structure, and affordable cost. It was therefore chosen to support the PdAuNi and Pd nanoparticles. There are various chemical and physical synthetic routes in the literature to prepare dispersed metal nanoparticles [81]. The synthesis protocol is thought to play a crucial role and contribute to the catalyst physicochemical and catalytic characteristics. Any chosen method should balance between fine-tuned catalytic properties and ease of preparation, leading potentially to facile mass production [82]. $NaBH_4$ metal reduction is a very common means to prepare C-supported catalysts due to its easy procedure and quality-produced catalysts. Moreover, there is more than one $NaBH_4$ protocol to prepare Pd-supported nanoparticles. This work aims to synthesize three carbon-based trimetallic catalysts based on different borohydride reduction protocols. The physicochemical and morphological properties of those materials were determined and compared. Their performance as electrocatalysts for BOR was analyzed and discussed considering the different synthesis routes employed and the final properties obtained for each material.

2. Materials and Methods

2.1. Chemicals

Metallic precursors ($PdCl_2$, $NiCl_2$, and $AuCl_3$) to synthesize PdAuNi/C electrocatalysts were purchased from Sigma-Aldrich (St. Louis, MO, USA). Vulcan carbon (XC-72R), purchased from Cabot Corp (Boston, MA, USA), was used to support the synthesized metal nanoparticles. $NaBH_4$ (SB, 96 wt.%), ethylene glycol (EG, 99.5 wt.%), 2-propanol (IPA, 99 wt.%), NaOH (85 wt.%), and ethanol (100%) were purchased from Sigma-Aldrich. For the electrochemical measurements, $NaBH_4$ (98 wt.%, Scharlau, Barcelona, Spain) and H_2O_2 (30 vol.%, Carlo Erba, Barcelona, Spain) were used. All chemicals were used as received without further purification.

2.2. Catalyst Preparation

Three borohydride reduction protocols using (i) a $NaBH_4$-ethylene glycol complex, (ii) a $NaBH_4$-2-propanol complex, and (iii) a three-step route were deployed to synthesize carbon-supported PdAuNi catalysts denoted herein as PdAuNi/C_{SBEG}, PdAuNi/C_{SBIPA}, and PdAuNi/$C_{3\text{-step}}$, respectively. The theoretical metal loading based on the quantity of metal salts used in the synthesis was 12 wt.% for PdAuNi/C_{SBIPA} and 20 wt.% for both PdAuNi/C_{SBEG} and PdAuNi/$C_{3\text{-step}}$. Although electrocatalysts for laboratory studies usually load the carbon support with 20 to 40 wt.% of metal, the use of lower loadings is more representative of industrial catalyst loadings which are typically ~5 wt.% [83].

The SBEG synthesis protocol uses a $NaBH_4$-ethylene glycol complex, following previous work [36,84,85]. Vulcan carbon (202 mg) was first dispersed in ethylene glycol (10 mL). The metallic precursor solution containing $PdCl_2$ (28 mg mL^{-1}), $AuCl_3$ (55 mg mL^{-1}), and $NiCl_2$ (36.7 mg mL^{-1}) was then suspended in ethylene glycol (10 mL). The two suspensions were subsequently mixed. Next, a solution of $NaBH_4$ (20 mL) was slowly added to the metal and carbon mixture under magnetic stirring. The mixture was heated to 35 °C and kept at that temperature for 3.5 h. The mixture was then left to cool and washed copiously with deionized water until neutralization. Following this, it was dried in a vacuum oven at 80 °C for 2 h.

The second reduction protocol (SBIPA) applied $NaBH_4$ following methods described in previous reports [86–89]. The Vulcan carbon and metal precursors were sonicated in a mixture of 2-propanol/water (50 vol.%). KBr was added to stabilize the metal nanoparticles. The mechanism of this is that the larger Br^- ions substitute for Cl^- ions in solution, stabilizing Pd particles and preventing further particle agglomeration [90]. Unlike an organic surfactant such as PVP, KBr can be washed off easily after synthesis from the particle surface. The KBr/metal atomic ratio was 1.5. The mixture was stirred for 10 min, followed by the addition of $NaBH_4$ solution (0.5 M, 15 mL). Stirring then continued for

another 30 min. Following this, the sample was washed under vacuum filtration. Finally, the wet powder was dried at 80 °C in a vacuum oven overnight.

The third protocol to prepare PdAuNi/C (three-step) aimed to compare the stepwise reduction of metals on the carbon surface to the co-reduction procedure practiced in the first two protocols. Consecutive reduction of different metals can lead to the formation of core@shell structures, such as Ru@Pd/C [91], Au@Pd [92,93], and Cu@Pd [94]. The $NaBH_4$-2-propanol reduction mixture was once more used to prepare this catalyst. The procedure started with sonicating Vulcan carbon (202.4 mg) in a mixture of 2-propanol/water (50 vol.%). Then, $NiCl_2$ was added and kept in the solution under stirring for 1 h. This was longer than the reduction time required for Au and Pd reduction time, as Ni is more oxyphilic and less reducible [95,96]. Subsequently, $AuCl_3$ was added with stirring for 30 min. Finally, $PdCl_2$ was added with stirring for 30 min. To illustrate the impact of adding both Au and Ni onto Pd, a monometallic C-supported Pd catalyst (Pd/C_{SBIPA}) was synthesized using the SBIPA procedure.

2.3. Physical Characterization

The crystal structure of the prepared catalysts was investigated using X-ray diffraction (XRD) with a Bruker D2 Phaser operating using Cu K_α radiation at 30 kV, 10 mA, and 12° min^{-1} scan rate. To evaluate the crystallite size, the Scherrer equation was applied using the Pd (111) peak details. To quantify the metallic species in each catalyst powder, inductively coupled plasma optical emission spectrometry (ICP-OES) was applied using a Spectro Ciros Vision spectrometer by Spectro Analytical Instruments Inc. (Kleve, Germany). The samples were first digested in HNO_3 (2%), followed by 10-fold dilution in aqua-regia (8%). The surface-weighted chemical composition of the catalysts was examined through energy-dispersive X-ray spectroscopy (EDX) attached to a JEOL JSM 6010LA scanning electron microscope (SEM) by JEOL Ltd. (Tokyo, Japan). Each catalyst surface was examined twice applying two different accelerating voltages: 10 kV and 20 kV [97] enabling studying the composition at two different depths. The catalyst morphology was examined by transmission electron microscopy (TEM) employing a Phillips C100 microscope (Hillsboro, OR, USA) operating at 100 kV applying LaB_6 filament. The TEM samples were prepared by suspending 5 mg of each sample powder in 2 mL of ethanol. Then, the mixture was sonicated for 1 h. A spray atomizer was then used to take 10 µL of the suspension to paint the holey carbon-coated Cu grid. The grid was left to dry for 24 h. The surface chemistry of the prepared electrocatalysts was studied by X-ray photoelectron spectroscopy (XPS) employing a Thermo Scientific K-Alpha+ spectrometer (Waltham, MA, USA). An Al-X ray source (72 W) and 400-μm^2 were applied. The pass energy to record the data was 150 eV for survey scans and 40 eV for high-resolution ones. The survey scan step size was 1 eV, but that of the high-resolution was 0.1 eV. Low-energy electrons and argon ions were used to neutralize the charge. CasaXPS from Casa Software Ltd. (Teignmouth, UK) was used to analyze the data and employed a Shirley-type background and Scofield cross-sections with an energy dependence of −0.6.

2.4. Working Electrode Preparation

Catalytic inks were prepared by ultrasonically dispersing 5 mg of each catalyst in 2 mL of ethanol and 25 µL of 5 wt.% Nafion suspension for 30 min. Subsequently, 5 µL of the prepared ink was deposited onto a glassy carbon electrode (GC, A = 0.0707 cm^2, inactive for BOR [98]) and left to dry at room temperature for 1 h. Catalyst loading was 0.175 mg cm^{-2} for all catalysts. The total metal loadings (calculated based on the ICP-OES results) were 0.021, 0.027, 0.039, and 0.015 mg cm^{-2} for Pd/C_{SBIPA}, $PdAuNi/C_{SBEG}$, $PdAuNi/C_{3\text{-step}}$ and $PdAuNi/C_{SBIPA}$, respectively. Pd loadings were 2.51, 2.41, 4.77, and 5.77 µg cm^{-2} for Pd/C_{SBIPA}, $PdAuNi/C_{SBEG}$, $PdAuNi/C_{3\text{-step}}$, and $PdAuNi/C_{SBIPA}$, respectively.

2.5. Electrochemical Evaluation

Electrochemical characterization was carried out in a conventional three-electrode setup of 125 mL. An ALS 2325 bipotentiostat (ALS Co., Ltd, Japan) combined with an RRDE-3A apparatus was used for fundamental experiments. Pt served as a counter electrode, and a saturated calomel electrode (SCE) as a reference electrode. All potential values within this paper were converted and are presented relative to RHE.

BOR measurements were carried out using cyclic and linear scan voltammetry. A 2 M NaOH solution was employed as the supporting electrolyte for all fundamental experiments. Cyclic voltammetry (CV) measurements were carried out in the potential range from OCP to 1.2 V applying scan rates from 5 to 1000 mV s^{-1}. Furthermore, the temperature effect was analyzed in the 25–65 °C temperature range. The BH_4^- concentration influence was studied in the 0.01–0.12 M range. Studies on the effect of temperature and concentration were conducted at a scan rate of 50 mV s^{-1}. RDE studies were carried out by linear scan voltammetry (LSV) at 10 mV s^{-1} by applying different rotation rates (0–2400 rpm). Apart from the concentration study, all experiments were conducted in a 0.03 M $NaBH_4$ in 2 M NaOH solution. Experiments were run at 25 °C and 0 rpm unless otherwise stated.

2.6. Fuel Cell Testing

A laboratory-scale direct borohydride peroxide fuel cell (DBPFC, V = 100 mL for both anodic and cathodic compartments) was assembled and tested. The two compartments were separated by a Nafion®117 (DuPont, Wilmington, DE, USA) cation-exchange membrane. A PAR 273A (Princeton Applied Research, Inc., Oak Ridge, TN, USA) potentiostat using PowerSuite software (PowerCV+ PowerSTEP) was employed for control of the experiments. The anolyte and catholyte were 1 M $NaBH_4$ in 4 M NaOH and 5 M H_2O_2 in 1.5 M HCl solutions, respectively. The chosen compositions are proven to be optimal in previous studies [99,100]. $PdAuNi/C_{SBIPA}$ was employed as the anodic catalyst (1 cm^2, 0.100 mg cm^{-2} catalyst loading, 0.012 mg cm^{-2} metal loading). The catalytic ink used for the anode was prepared as described in Section 2.4, with a GC tip used as substrate electrode. The cathode was a Pt mesh with a high surface area (Johnson Matthey, A = 50 cm^2) to ensure that fuel cell performance was not limited by the cathodic process. Interelectrode distance was the lowest possible to minimize ohmic resistance. DBPFC performance was analyzed in the 25–65 °C temperature range. Cell polarization curves were recorded, and the corresponding power density curves were plotted.

3. Results and Discussion

3.1. Physical Characterization Results

Figure 1 shows the XRD patterns of Pd/C and the three trimetallic catalysts. All catalysts showed one broad peak at 25°, typical of graphitic Vulcan carbon. For the monometallic Pd/C, the pattern showed four peaks that are characteristic of Pd (111), (200), (220), and (311) faces at 39.8°, 46.5°, 68.3°, and 82.1°, respectively (PDF#46-1043). However, for both trimetallic catalysts prepared by co-reduction (SBEG and SBIPA), there was a small shift in the peak positions to lower diffraction angles. This shift is ascribed to alloying among the three metals. Pd and Au, in particular, are well-known to exhibit remarkable alloying behavior [95,101–108]. Although Pd and Ni are known to form a solid solution for their bulk alloys, their potential for formulating a nanoalloy is lower [96,107–109]. It is not uncommon to see distinctive $Ni(OH)_2$ peaks at 60.1°, which is indicative of bulk Ni species segregation. In the present study, the shift in the two co-reduced trimetallic samples was suggestive of a nanoalloy formation among the metals. However, the appearance of $Ni(OH)_2$ peaks at 33.4° and 60.1° in the case of $PdAuNi/C_{SBEG}$ implied there was some Ni segregation in the bulk of that catalyst. Additionally, these $Ni(OH)_2$ peaks were also present in the three-step catalyst, although smaller than that of $PdAuNi/C_{SBEG}$.

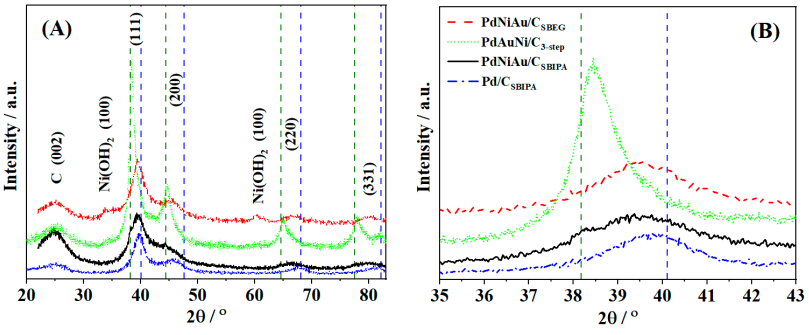

Figure 1. (**A**) XRD patterns of PdAuNi/C_{SBEG}, PdAuNi/C_{SBIPA}, Pd/C_{SBIPA}, and PdAuNi/$C_{3\text{-step}}$ and (**B**) the enlarged (111) facet for the four catalysts.

In contrast to PdAuN/$C_{3\text{-step}}$ and PdAuNi/C_{SBEG}, the catalyst synthesized via the SBIPA protocol did not show any individual Ni peaks. This indicated a higher potential of mixing of the three metals when the SBIPA protocol was used. KBr addition may also have contributed due to the replacement of the smaller Cl^- anion with Br^- during synthesis [110].

Unlike the SBEG and SBIPA catalysts, the XRD peaks of PdAuNi/$C_{3\text{-step}}$ were closer to pure Au (PDF#04-0784) than pure Pd (PDF#46-1043). This suggested the formation of Au@Pd (core@shell) structure as a consequence of the stepwise reduction process as previously reported [92,93]. Another important observation is that the XRD peak shift to lower diffraction angles was suggestive of the expansion of the Pd crystal lattice by the incorporation of the larger Au atoms into the Pd lattice. Ni is, theoretically, expected to contract the lattice, not to expand it. However, previous studies have found that adding Ni to Pd does not seem to displace the Pd diffraction peaks and therefore Ni does not necessarily contract the Pd lattice [59,111,112]. The peak shift in the case of PdAuNi/C_{SBEG} and PdAuNi/C_{SBIPA} is therefore consistent with lattice expansion and tensile strain that could upshift the *d*-band center and decrease the adsorbate-Pd bond strength [105].

The XRD Pd(111) peak of the four catalysts was analyzed to extract the peak broadening and diffraction angle values of each sample, and subsequently to determine their structural parameters: particle size, interplanar distance, and lattice constants (Table 1). The detailed analysis is explained in section "1. XRD calculation" of supplementary information (SI). While the interplanar distance and lattice constant were the same for Pd/C_{SBIPA}, PdAuNi/C_{SBIPA}, PdAuNi/C_{SBEG} (2.26 and 3.92 Å, respectively), it has increased in the case of PdAuNi/$C_{3\text{-step}}$ to 2.33 and 4.03 Å, respectively. It is noteworthy that the smallest particle size and highest broadening (FWHM) were those of PdAuNi/C_{SBIPA}, followed by the monometallic Pd/C_{SBIPA}, PdAuNi/C_{SBEG}, and, finally, PdAuNi/$C_{3\text{-step}}$. Factors other than crystallite size can also contribute to peak broadening, e.g., the instrument employed and the lattice strain. However, the Scherrer equation (Equation (S3)) is known to provide a reliable approximation of the crystallite size. The large particle size of PdAuNi/$C_{3\text{-step}}$ could be attributed to its Au-like structure, which presents larger lattice and interplanar distances.

Table 1. Structural and morphological parameters of Pd/C_{SBIPA}, PdAuNi/C_{SBIPA}, PdAuNi/C_{SBEG}, and PdAuNi/$C_{3\text{-step}}$.

Catalyst	*2θ*°	FWHM°	*d*-Space (Å)	*a* (Å)	τ_{XRD} (nm)
Pd/C_{SBIPA}	39.8	2.19	2.26	3.92	4.3
PdAuNi/C_{SBIPA}	39.4	2.47	2.26	3.92	3.8
PdAuNi/C_{SBEG}	39.6	2.32	2.26	3.92	4.9
PdAuNi/$C_{3\text{-step}}$	38.5	1.11	2.33	4.03	8.9

The bulk elemental composition of the synthesized catalysts was investigated by ICP-OES, as illustrated in Table 2. For Pd/C_{SBIPA}, the identified Pd loading was 12 wt.%, equivalent to the theoretical value. For $PdAuNi/C_{SBIPA}$, $PdAuNi/C_{SBEG}$, and $PdAuNi/C_{3\text{-step}}$, Pd loadings of 9 wt.%, 16 wt.%, and 22 wt.% were identified, respectively.

Table 2. ICP-OES metal composition of Pd/C_{SBIPA}, $PdAuNi/C_{SBIPA}$, $PdAuNi/C_{SBEG}$, and $PdAuNi/C_{3\text{-step}}$.

Catalyst	Pd/wt.%	Au/wt.%	Ni/wt.%
Pd/C_{SBIPA}	12	-	-
$PdAuNi/C_{SBIPA}$	5.1	2.6	0.7
$PdAuNi/C_{SBEG}$	4.8	0.8	9.9
$PdAuNi/C_{3\text{-step}}$	7.5	5.5	9.3

While ICP-OES determines the whole composition of the catalysts, the catalytically active sites are not dispersed throughout the bulk of the material. Instead, interaction with reactants takes place at surface sites. Therefore, the surface-weighted technique of EDX was used to gain insights into the composition of the catalysts in the catalytically relevant surface region. Figure 2 shows EDX metal elemental maps of $PdAuNi/C_{SBEG}$.

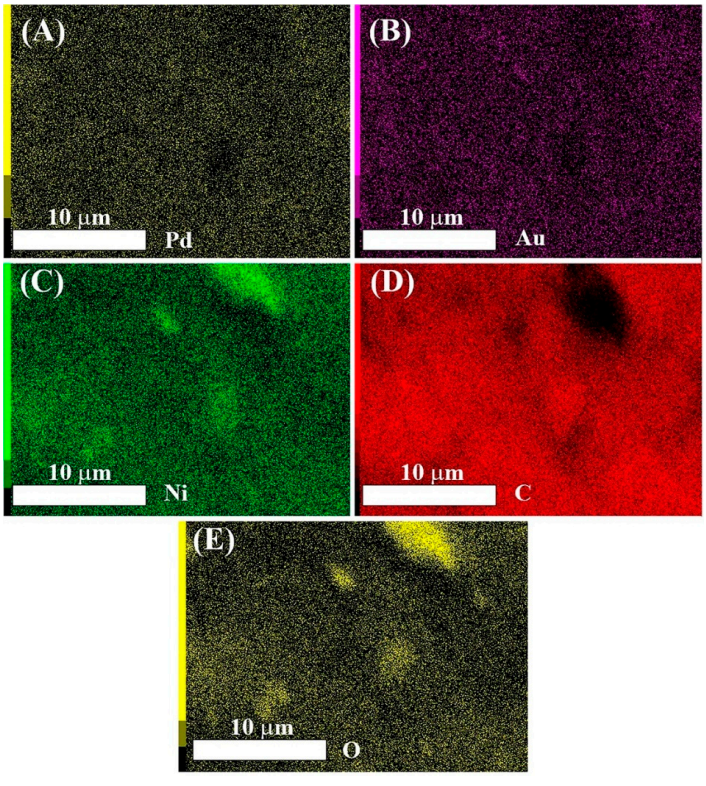

Figure 2. Elemental maps of (**A**) Pd, (**B**) Au, (**C**) Ni, (**D**) C, and (**E**) O obtained by EDX spectroscopy of $PdAuNi/C_{SBEG}$ at 10 kV.

While the Pd (A) and Au (B) maps show similar and relatively even distribution of both metals, the Ni map (C) shows three areas that were more densely populated with Ni species, indicating that Ni was not homogeneously distributed at the surface. The regions of high Ni density correspond to regions of low density in the C map (D) and in the O map

(E). This may suggest that some bulk segregation of $Ni(OH)_2$ had occurred, as supported by XRD data where a $Ni(OH)_2$ peak was observed, Figure 1.

Table 3 shows the quantitative composition data extracted from EDX in both weight and atomic percent for the three trimetallic catalysts investigated. This aimed to highlight the different surface metal segregation by applying two accelerating voltages: 10 kV and 20 kV, the latter providing greater surface penetration. Unlike Pd and Au, the atomic concentration of Ni at 10 kV was larger than that at 20 kV. This further confirms that Ni segregation to the catalyst surface occurred. EDX analyses revealed higher metal loading than either ICP-OES or the theoretical compositions, as the synthesis resulted in a heterogeneous composition throughout the carbon support, with metal preferentially located towards the surface, beneficial for catalysis.

Table 3. Quantitative EDX analysis of PdAuNi/C_{SBEG}, PdAuNi/$C_{3\text{-step}}$, and PdAuNi/C_{SBIPA} at 10 kV and 20 kV.

	PdAuNi/C_{SBEG}				**PdAuNi/$C_{3\text{-step}}$**				**PdAuNi/C_{SBIPA}**			
	10 kV		**20 kV**		**10 kV**		**20 kV**		**10 kV**		**20 kV**	
	wt.%	**at.%.**	**wt.%**	**at.%**	**wt.%**	**at.%.**	**wt.%**	**at.%**	**wt.%**	**at.%.**	**wt.%**	**at.%**
C	63.9	82.7	62.3	80.6	62.6	84.5	61.8	82.8	60.1	83.6	59.3	81.5
O	6.67	6.48	8.48	8.25	4.44	4.50	5.42	5.46	4.63	4.84	6.56	6.77
Ni	13.4	3.54	12.3	3.25	8.51	2.35	6.74	1.85	10.2	2.90	8.97	2.52
Pd	6.03	0.88	6.23	0.91	10.4	1.58	10.7	1.62	11.5	1.80	11.3	1.75
Au	3.82	0.30	3.93	0.31	7.96	0.66	8.17	0.67	7.92	0.67	7.56	0.63

Figure 3 shows the EDX maps of PdAuNi/C_{SBIPA}. Unlike PdAuNi/C_{SBEG}, the Au (A), Pd (B), and Ni (C) maps show that the three metals were co-located with high-density regions of one metal corresponding to high-density regions of the others. Areas of low metal density corresponded to density regions in the C map (D). This is anticipated, as at regions of low metal density, the bare C support was exposed at the surface. Although to a lesser extent than PdAuNi/C_{SBEG}, the quantitative data for PdAuNi/C_{SBIPA} (Table 3) indicated a slightly higher concentration of Ni at 10 kV (2.90 at.%) as compared to that at 20 kV (2.52 at.%), perhaps indicating some surface segregation of Ni for this material as well. Overall, PdAuNi/C_{SBIPA} showed relatively homogeneous metal distribution throughout the surface region, indicative of good mixing characteristics of the three metals in this case. This was further supported by the absence of any distinctive Ni peaks in this catalyst XRD pattern. Similar to PdAuNi/C_{SBIPA}, the EDX analysis of PdAuNi/$C_{3\text{-step}}$ revealed that Pd, Au, Ni, and C were co-located with each other (Figure S1), suggesting good mixing and little Ni segregation in this material.

Figure 4 shows representative TEM micrographs obtained for the Pd/C_{SBIPA}, PdAuNi/C_{SBIPA}, PdAuNi/C_{SBEG}, and PdAuNi/$C_{3\text{-step}}$ electrocatalysts, with additional TEM images being included in SI (Figures S2–S5). Examining the micrographs, the presence of highly dispersed metal nanoparticles on the carbon surface could be inferred. The very small particles indicated metal nanoparticles, while the large grey particles (40–60 nm) indicated the carbon aggregates. However, some particle aggregation and agglomeration could also be seen. This could be due to the synthesis method and/or being a monometallic system, which can promote particle growth and agglomeration more than a bimetallic or trimetallic one [56]. Comparing the trimetallic PdAuNi/C_{SBIPA} catalyst with the monometallic one prepared by applying the same protocol suggests that the latter explanation may apply in this case.

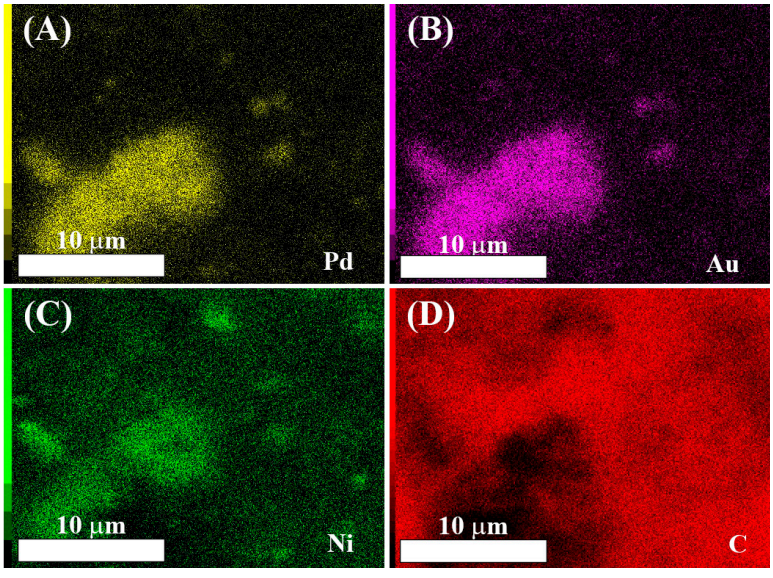

Figure 3. Elemental maps of (**A**) Pd, (**B**) Au, (**C**) Ni, and (**D**) C of PdAuNi/C_{SBIPA} obtained by EDX spectroscopy at 10 kV.

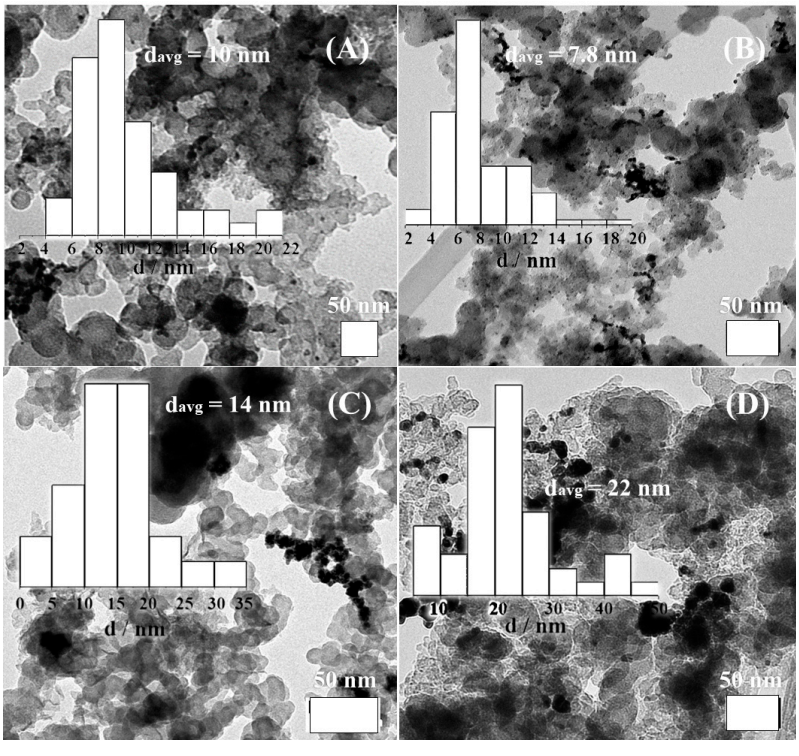

Figure 4. TEM micrographs and corresponding particle size distribution histograms of (**A**) Pd/C_{SBIPA}, (**B**) PdAuNi/C_{SBIPA}, (**C**) PdAuNi/C_{SBEG}, and (**D**) PdAuNi/$C_{3\text{-step}}$.

PdAuNi/C_{SBIPA} particles (1–6 nm, consistent with XRD analysis, Table 1) were very well dispersed, and less particle aggregation could be seen as compared to Pd/C. The reverse situation was noted for the PdAuNi/C_{SBEG}, which showed significant particle aggregation. Above those few carbon particles, high metal particle aggregation could be seen. This could be promoted by the $NaBH_4$-ethylene glycol reduction complex at 40 °C. Additionally, as discussed above with reference to the EDX map (Figure 3C), the high Ni content in this catalyst might contribute to this agglomeration, noting that Ni exists only in the form of $Ni(OH)_2$ (Figure 5).

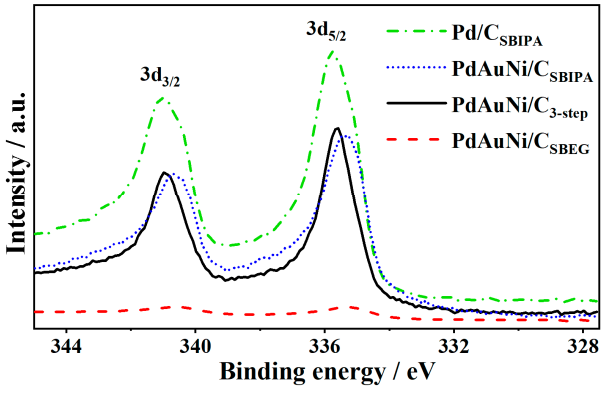

Figure 5. XPS spectra of Pd 3d in PdAuNi/C_{SBIPA}, Pd/C_{SBIPA}, PdAuNi/C_{SBEG}, and PdAuNi/$C_{3\text{-step}}$, showing Pd $3d_{3/2}$ and Pd $3d_{5/2}$ peaks.

The preparation method may also play a role in the promotion of agglomeration. For PdAuNi/C_{SBEG}, the metal precursors were initially mixed in ethylene glycol, followed by the slow addition of $NaBH_4$. Once the $NaBH_4$ addition commenced, the orange/brown solution turned black instantly, alongside the formation of bubbles. PdAuNi particles had most likely been reduced and segregated before the carbon support was added. For PdAuNi/$C_{3\text{-step}}$, on the other hand, Ni was initially reduced on the carbon surface (for 30 min), followed by Au (for 30 min), and finally Pd (for 30 min). As is clear from the XRD and EDX measurements, Ni segregation occurred once again, further verified by the observation of $Ni(OH)_2$ peaks, albeit in lower intensity than for PdAuNi/C_{SBEG}. Additionally, Au had most likely formed a core@shell structure with Pd, since the XRD pattern was more representative of Au than of Pd. Although to a lesser degree than PdAuNi/C_{SBEG}, significant particle aggregation was observed, and particle size was the largest in comparison to the other catalysts. Following PdAuNi/$C_{3\text{-step}}$, PdAuNi/C_{SBEG} particle size was larger than that of both Pd/C_{SBIPA} and PdAuNi/C_{SBIPA}. The PdAuNi particle sizes obtained were slightly smaller than previously reported for trimetallic systems [68,69].

Figure 5 shows the XPS measured data for the Pd 3d peak positions of the four catalysts. The molar Pd:Au:Ni ratio of PdAuNi/C_{SBIPA} equaled 64:17:19, while it was 5:1:94 and 58:6:36 for PdAuNi/C_{SBEG} and PdAuNi/$C_{3\text{-step}}$, respectively. This showed the abundant Pd presence on the surface of PdAuNi/$C_{3\text{-step}}$ and PdAuNi/C_{SBIPA} samples, while PdAuNi/C_{SBEG} contained mainly Ni (94 at.%) and only 6 at.% Pd and Au combined. Furthermore, it is noteworthy that the highest oxygen content (5.19 at.%) existed in PdAuNi/C_{SBEG}, likely a consequence of the presence of significant $Ni(OH)_2$ (2.19 at.%). The Pd 3d peak of Pd/C_{SBIPA} (Table S1 in SI) could be deconvoluted into a high-energy band corresponding to Pd $3d_{3/2}$ (340.73 eV) and a low-energy band corresponding to Pd $3d_{5/2}$ (335.43 eV). Those bands were shifted approximately 0.40 eV to higher binding energy compared to pure Pd, due to the interaction with the C support. Moreover, the Pd 3d binding energies of PdAuNi/C_{SBEG} and PdAuNi/C_{SBIPA} samples were shifted ~0.5 eV and 0.15 eV, respectively, to lower binding energies. On the contrary, Pd 3d of PdAuNi/$C_{3\text{-step}}$

was shifted 0.05 eV to binding energy higher than that of the Pd/C_{SBIPA} sample. Pd 3d peak positions are shown in Figure 5. Ni 2p and Au 4f were also shifted in the three trimetallic samples compared to pure Au and Ni, the binding energies of which were 84 eV and 855.6 eV ($Ni(OH)_2$), respectively. While the Ni peaks shifted towards higher binding energy compared to pure Ni, the reverse trend was observed for Au. The Ni 2p shift was estimated to be +0.3 eV, +0.7 eV, and +0.8 eV for PdAuNi/C_{SBIPA}, PdAuNi/C_{SBEG}, and PdAuNi/$C_{3\text{-step}}$, respectively. The Au 4f shift was −0.3 eV, −0.4 eV, and −0.2 eV for PdAuNi/C_{SBIPA}, PdAuNi/C_{SBEG}, and PdAuNi/$C_{3\text{-step}}$, respectively. The shift in the binding energy was indicative of a change in the adsorption behavior of the respective catalysts. The presence of Au and Ni potentially explains why PdO was not detected in the trimetallic sample, unlike in the monometallic one, which contained 20 wt.% of Pd as PdO. Adding both Au and Ni enhanced Pd air stability. The full XPS surveys are illustrated in Figure S6. The individual elemental (Pd 3d, Au 4f, and Ni 2p) XPS peaks are available in Table S1, which confirms that Pd and Au existed in the metallic state in the trimetallic samples, Pd existed in metallic and oxide form in the monometallic sample, and Ni predominantly existed as $Ni(OH)_2$. The Ni 2p peak in the PdAuNi/C_{SBIPA} sample contained some Ni metal alongside $Ni(OH)_2$, unlike PdAuNi/C_{SBEG} and PdAuNi/$C_{3\text{-step}}$. This further exemplifies the good mixing of the three metals obtained by the SBIPA protocol, which was corroborated by the XRD and EDX data.

PdAuNi/C_{SBEG} has furthermore achieved the highest shift of Pd 3d to the left, which was also the broadest from the four-sample Pd 3d peaks as reported for the addition of Ni to Pd [108]. Examining the Ni 2p peaks of the three trimetallic samples, two high-binding-energy satellite peaks were adjoined to the main peaks of Ni, which indicates Ni multi-electron excitations [59,96,111,112]. Additionally, in the case of PdAuNi/C_{SBEG} and PdAuNi/$C_{3\text{-step}}$ samples, the single pattern of two Ni 2p peaks suggests the presence of only one oxide species, $Ni(OH)_2$, in contrast to the findings of Ramulifho et al. [113]. In terms of co-reduction, Au is the easiest of the three metals to reduce, followed by Pd. On the contrary, Ni is the slowest to reduce [95,114]. Therefore, it may not be incorrect to assume that the surface of the trimetallic catalysts (especially PdAuNi/C_{SBEG}) was richest in Ni and poor in Au, which was evident from the XPS and EDX measurements. On the other hand, the core would be highly populated with Au and lacking a substantial Ni proportion.

3.2. Borohydride Oxidation Reaction Studies

The catalytic performance of the three PdAuNi/C electrocatalysts towards the BOR was initially investigated by scanning comparative CVs in 2 M NaOH with 0.03 M $NaBH_4$ and in pure 2 M NaOH. Along with evaluating the activity of the synthesized trimetallic catalysts, the response of monometallic Pd/C was also evaluated in order to better understand the role played by Au and Ni. The CVs of three catalysts as well as of monometallic Pd/C depicted in Figure 6A–C show the absence of any relevant anodic peaks in the BOR potential region in NaOH solution, implying that the current generated during CVs recorded in the presence of BH_4^- originated from its oxidation. Based on the shape of the CVs and similar OCP values of ca. −0.12 V, it could be assumed that the studied catalysts promoted similar reaction mechanisms. Similar OCP values were reported in other recent studies on BOR at Pd-containing materials [53,54]. Within the scanned potential range, CVs of three different catalysts showed two oxidation peaks in the positive scan, while an additional sharp oxidation peak was evident in the reverse scan. The first oxidation peak appeared as a wide oxidation hump at ca. 0.29 V for the PdAuNi/C_{SBEG} and PdAuNi/C_{SBIPA} catalysts, while in the case of PdAuNi/$C_{3\text{-step}}$, this peak was more pronounced and positioned at more positive potential (0.38 V). It is believed that this peak can be attributed to H_2 oxidation, which originates from the borohydride hydrolysis reaction, and to the initial oxidation of adsorbed BH_3OH^- [54]. The second anodic peak at ~0.8 V for all examined samples can be considered to originate from electrooxidation of BH_4^- as well as BH_3OH^- [48,54]. PdAuNi/C_{SBIPA} gave the best catalytic response,

reaching the peak current density of 46 mA cm^{-2} at 50 mV s^{-1}, a value considerably higher than those reached employing carbon-supported Pd-Cu [115], Pd-Au [116], and Au-Ni [117] alloy nanoparticles. Additionally, the oxidation peak on the cathodic scan in the potential window from 0.5 to 0.8 V for all three studied samples was most likely related to the oxidation of BH_3OH^- [118], which was formed during the anodic scan and stayed adsorbed on the oxidized electrode surface until it was reactivated by reduction of the surface oxides.

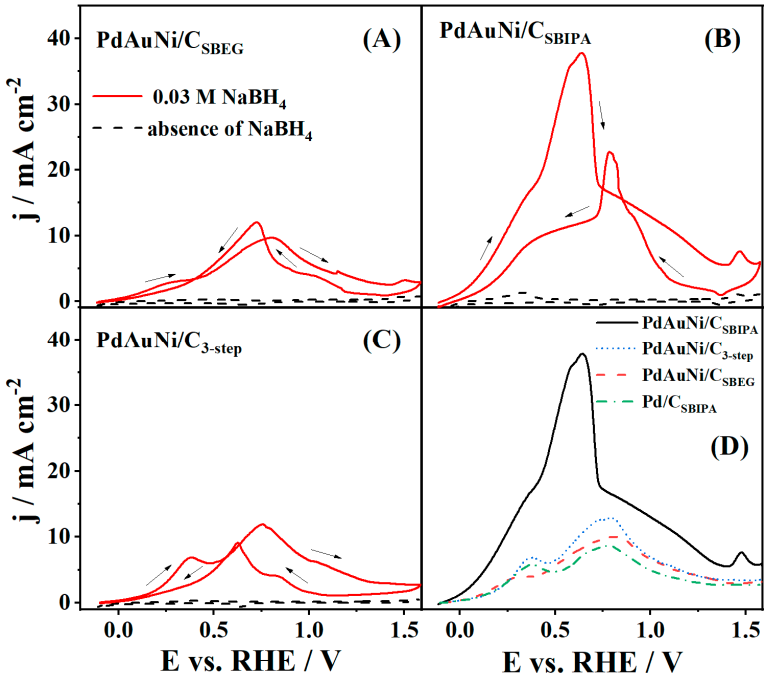

Figure 6. CVs (third cycle) in the absence (2 M NaOH) and presence (2 M NaOH + 0.03 M $NaBH_4$) of BH_4^- for (**A**) PdAuNi/C_{SBEG}, (**B**) PdAuNi/C_{SBIPA}, and (**C**) PdAuNi/$C_{3\text{-step}}$ electrocatalysts, and (**D**) comparative CVs of trimetallic and Pd/C_{SBIPA} monometallic catalysts in the presence of BH_4^-. CVs ran at 50 mV s^{-1} and 25 °C.

The catalytic performance of the synthesized materials was further compared with the response obtained for monometallic Pd/C_{SBIPA}. Figure 6D reveals the inferior catalytic activity of Pd/C_{SBIPA}. Introducing Au and Ni into Pd provided more active sites where BH_4^- adsorption could take place and as such, trimetallic catalysts were expected to exhibit higher activity towards BOR. Improved catalytic properties can be explained by the produced synergistic effect of combining Pd with Au, a metal that is relatively inert towards hydrolysis, and Ni, a 3d transition metal, and the resultant electronic effect. In terms of electronic interaction, as XPS results suggest, the addition of Ni may have influenced the atomic band structure of the other two metals. This can further lead to the reduced adsorption energy of BOR intermediates, thus preserving those active sites for BH_4^- adsorption and further encouraging BOR activity [119].

The PdAuNi/C_{SBIPA} highest catalytic activity most likely resulted from the absence of segregation of Ni. This enabled an improved degree of alloying in comparison with the other two studied catalysts, as confirmed by XRD results. Additionally, the enhanced catalytic activity of PdAuNi/C_{SBIPA} could also be associated with the better dispersed multi-metallic particles of smaller average size, confirmed by TEM analysis and the re-

spective EDX elemental maps. Smaller particle size and interparticle distance produced larger surface area and, therefore, were deemed beneficial for catalytic reactions. However, caution must be practiced as Antolini et al. [120] reviewed that decreasing the particle size below 5 nm and interparticle distance below 20 nm adversely impacts the reduction of oxygen, as well as reactions of ethanol and methanol oxidation on Pt surfaces. The situation would be worse for a highly aggregated particle system due to exceedingly smaller interparticle distance. That is a likely reason for the lower PdAuNi/C_{SBEG} performance in the present study. The CVs shown in Figure 6 are also available in specific current density (mA $mg_{metal}{}^{-1}$) in SI (Figure S7).

BOR kinetic parameters are summarized in Table 4 for each catalyst.

Table 4. Kinetic parameters for BOR at the four studied catalysts.

Catalyst	α	n	β	E_a/kJ mol^{-1}
PdAuNi/C_{SBEG}	0.60	2.8	0.91	34.0
PdAuNi/C_{SBIPA}	0.75	7.1	1.00	16.7
PdAuNi/$C_{3\text{-step}}$	0.73	7.4	1.12	29.9
Pd/C_{SBIPA}	0.70	1.2	0.94	28.9

For all samples, an upward trend of current density with increasing polarization rate, as well as a small shift in the position of the characteristic $BH_4{}^-$ oxidation peak to more positive potentials were observed. Figure 7A illustrates this behavior for PdAuNi/C_{SBIPA} as the best material. This allowed for the determination of the charge transfer coefficient (α) values using the expression describing the peak potential dependence on the logarithm of polarization rate (E_p vs. ln ν) for irreversible processes [12,121]. The values were found to be relatively similar for all studied catalysts (Table 4), with PdAuNi/C_{SBIPA} showing the highest α value. High values indicate that BOR at examined electrocatalysts was an irreversible and diffusion-controlled process. The obtained values are comparable to the ones reported for catalysts containing Pd, Au, and Ni [12,25,47,79,100,121].

In the case of PdAuNi/C_{SBIPA} (Figure 7B), a significant increase in anodic current densities when recording the CVs starting from 0.01 M to 0.12 M $NaBH_4$ concentration was evident. The CVs revealed that the anodic current density value amounted to 8.5 mA cm^{-2} for the lowest concentration (0.01 M), while a value nine times higher was achieved for the highest $NaBH_4$ concentration. The observed trend corresponded to enhanced mass transfer, and this behavior agrees with previous reports employing Au-, Pd-, and/or Ni-based electrocatalysts [48,78,79,122,123]. In addition, the oxidation process started at lower potentials but reached its maximum at more positive potential values. The order of reaction (β) values was obtained using ln j vs. ln c plot slope and ranged from 0.91 for PdAuNi/C_{SBEG} to 1.12 for PdAuNi/$C_{3\text{-step}}$.

CVs obtained at elevated temperatures also exhibited higher current densities for all studied electrocatalysts. This behavior was expected, since higher temperatures lead simultaneously to a decrease in solution viscosity, resulting in a higher $BH_4{}^-$ diffusion coefficient, and faster electron transfer kinetics. By constructing the Arrhenius plots [121], depicted in the inset of Figure 7C, and applying the Arrhenius equation, the values of the apparent activation energy, $E_a{}^{app}$, were estimated. PdAuNi/C_{SBIPA} showed the lowest value of 16.7 kJ mol^{-1}, while the highest value of this parameter was observed for PdAuNi/C_{SBEG} (34 kJ mol^{-1}). Similar values were reported for mono- and bimetallic noble metal or/and transition metal-containing materials. For instance, BOR at carbon-supported Pd catalyst (prepared using different synthesis methods and types of carbon support) [53,124] has been shown to proceed with activation energy ranging from as low as 10 kJ mol^{-1} to 26 kJ mol^{-1}. Moreover, $E_a{}^{app}$ of BOR at a commercially available Pt/C [22] catalyst was reported to have a value of 34 kJ mol^{-1}, while alloying with transition metals (Co and Ni) resulted in lower values (25 and 20 kJ mol^{-1}, respectively).

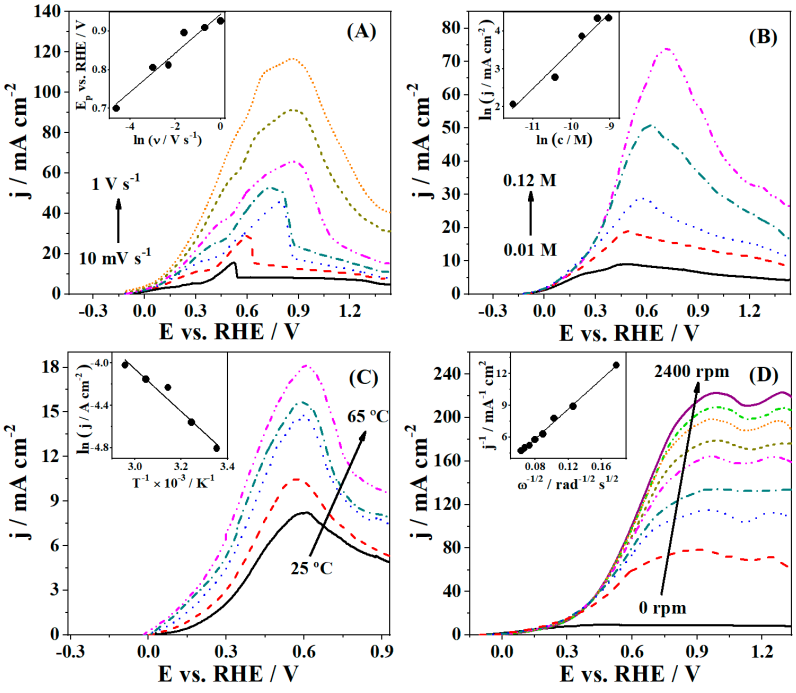

Figure 7. CVs of PdAuNi/C_{SBIPA} at (**A**) different scan rates, ν, and the derived E_p vs. ln ν plots (inset), (**B**) different $NaBH_4$ concentrations and the derived ln j vs. ln c plots (inset), (**C**) different temperatures and the derived Arrhenius plots (inset), and (**D**) LSVs of PdAuNi/C_{SBIPA} at 10 mV s^{-1} and different rotation rates and the derived Koutecky–Levich plot (inset). The electrolyte solution used was 0.03 M $NaBH_4$ + 2 M NaOH, polarization rate was 50 mV s^{-1}, with room temperature (25 °C), unless otherwise noted.

The reaction kinetics were additionally examined using RDE LSVs, and polarization curves were obtained; the corresponding j^{-1} vs. $\omega^{-1/2}$ plot for the currents taken at 0.9 V (inset) is shown in Figure 7D. From the slope of j^{-1} vs. $\omega^{-1/2}$ plots and using the Koutecky–Levich equation, n values were obtained [125]. The shift of half-wave potential with an increase of the electrode rotation speed confirmed the irreversibility of the reaction.

The n values for PdAuNi/$C_{3\text{-step}}$ and PdAuNi/C_{SBIPA} electrocatalysts (7.4 and 7.1, respectively) were determined to nearly match the theoretical value of 8, while significantly lower values were obtained for the other two materials (2.8 and 1.2 for PdAuNi/C_{SBEG} and Pd/C_{SBIPA}, respectively). Although in terms of current densities, PdAuNi/$C_{3\text{-step}}$ showed significantly lower values than PdAuNi/C_{SBIPA}, the highest n value could be explained by Au@Pd (core@shell) structure formation previously identified in the XRD analysis. Such a structure makes the behavior of the catalyst more Au-like due to the core position of those nanoparticles and as such, less active toward the BH_4^- hydrolysis reaction [12,100,126]. The lower faradaic efficiency of PdAuNi/C_{SBEG} and Pd/C_{SBIPA} was most likely a consequence of the higher hydrolysis rates at those two electrocatalysts. Obtained n values for PdAuNi/C_{SBEG} and Pd/C_{SBIPA} are similar to the ones obtained for other Pd-containing materials reported in previous studies. For instance, Martins et al. [54] reported n values of 2 and 5.6 during BOR at Pd nanoparticles with two different types of biobased carbon supports. For other Pd-based catalysts, depending on $NaBH_4$ concentration, n values between 2 and 6 [53,118] were obtained, indicating hydrolysis occurrence in parallel with the oxidation of BH_4^-. Song et al. [127] recently reported high BOR current densities for a ternary CuPdNi electrode, but at high overpotentials and an n value of 4.9, far from those obtained for the two best catalysts in this work. Alloying Pd

with Au resulted in n ~6, as reported by Simões et al. [57], also lower than values than obtained herein for PdAuNi/C_{SBEG} and Pd/C_{SBIPA}. Figure 7 is also available in specific current density (Figure S8 of SI).

3.3. Fuel Cell Testing

Figure 8 (available in SI in specific current density, Figure S9) depicts the polarization and power density curves of a single cell with PdAuNi/C_{SBIPA} anode operating at two different temperatures, 25 and 75 °C, along with anode and cathode potentials measured during the cell operation and experimentally measured cell voltage. The cathode potential measured in zero current regime (open-circuit conditions) at 25 °C was almost identical to the equilibrium potential of H_2O_2 reduction given in Equation (4) (E^0 = 1.78 V), suggesting direct H_2O_2 reduction. As for the cell operating at elevated temperature (75 °C), this value was slightly less positive, as expected, implying H_2O_2 disproportionation was followed by O_2 reduction to a certain extent [18,21]. On the other hand, the anode potential measured during the experiment was significantly higher than the equilibrium potential for BOR described by Equation (1), implying that the anodic process also involved side reactions, such as oxidation of H and BH_3OH^- generated during spontaneous hydrolysis of BH_4^- [128]. Moreover, from Figure 8B,C, a small difference between cell voltage, E_{cell}, and the calculated potential difference of the half-reactions, E_c–E_a, could be observed, which revealed minor resistance of system components.

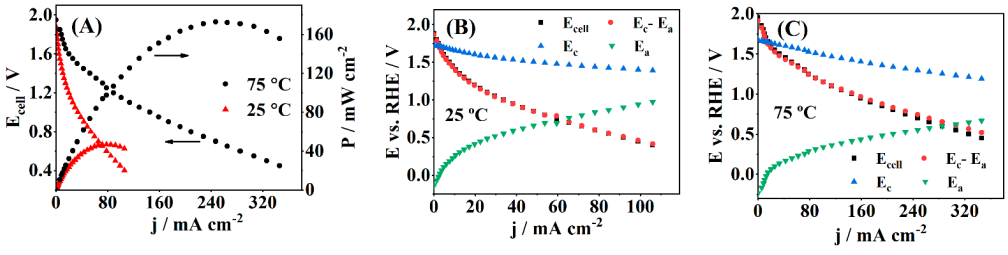

Figure 8. (**A**) Polarization and power density curves at 25 and 75 °C for a DBPFC using a PdAuNi/C_{SBIPA} anode and a Pt cathode. The cathode and anode potentials, their potential difference, and E_{cell} are also represented at (**B**) 25 °C and (**C**) 75 °C.

Considering the pH values of electrolytes, the theoretical voltage value of such fuel cells was expected to be close to 3 V. However, the cell polarization curves show an OCV value of ~1.9 V at both temperatures. This fluctuation in OCV value was mainly triggered by the mixed potential occurrence on the anodic side and it agrees with the reports from the literature for DBPFCs studies performed under conditions similar to the ones reported herein [18,125,128]. After the initial voltage decay due to activation losses, cell voltage continued to decrease linearly with current density, while mass transport effects were not evident. The power density value reached its maximum of 47.5 mW cm^{-2} at 0.6 V and 78 mA cm^{-2}. As expected, at an elevated temperature of 75 °C, the kinetics of both fuel cell reactions (BOR and HPRR) was faster, and a significant improvement in cell performance was displayed. The maximum value of power density that was obtained at this temperature was almost four times higher than that at 25 °C, amounting to 175 mW cm^{-2}. This value was exhibited at a cell voltage value of 0.7 V, while current density reached 247 mA cm^{-2}. The comparison of the DBPFC results obtained herein with the ones from the literature is shown in Table 5.

Table 5. Comparison of the DBPFC parameters obtained in this work with those reported in similar studies using Pd, Au, Ni, and their alloys.

Anode	Cathode	Fuel	Oxidant	T/°C	OCV/V	P/mW cm^{-2}	$E_{cell,\ peak}$/V	Ref.
$PdAuNi/C_{SBIPA}$	Pt	1 M $NaBH_4$ + 4 M NaOH	5 M H_2O_2 + 1.5 M HCl	25 75	1.90 1.90	47.5 175	0.60 0.70	This work
Au/C	Pt	0.5 M $NaBH_4$ + 2 M NaOH	4.5 M H_2O_2 + 2 M HCl	20	1.41	8.72	0.42	[119]
AuCu/C	Pt	0.5 M $NaBH_4$ + 2 M NaOH	4.5 M H_2O_2 + 2 M HCl	20	1.50	31.3	0.49	[119]
AuNi/C	Pt	0.5 M $NaBH_4$ + 2 M NaOH	4.5 M H_2O_2 + 2 M HCl	20	1.59	40.6	0.57	[119]
$Au_{1.5}NiCu/C$	Pt	0.5 M $NaBH_4$ + 2 M NaOH	4.5 M H_2O_2 + 2 M HCl	20	1.62	47.4	0.70	[119]
Au_2NiCu/C	Pt	0.5 M $NaBH_4$ + 2 M NaOH	4.5 M H_2O_2 + 2 M HCl	20	1.78	60.5	0.88	[119]
Au/C	Au/C	1 M $NaBH_4$ + 3 M NaOH	2 M H_2O_2 + 0.5 M H_2SO_4	25	1.87	28.2	0.59	[129]
$Au_{45}Co_{55}/C$	Au/C	1 M $NaBH_4$ + 3 M NaOH	2 M H_2O_2 + 0.5 M H_2SO_4	25	1.92	66.5	0.77	[129]
Ni@Pd/PANI [1]	Pt/C	1 M $NaBH_4$ + 2 M NaOH	2 M H_2O_2 + 1.5 M HCl	60	1.76	120	0.61	[130]
PtNi/C	Pt/C	1 M $NaBH_4$ + 2 M NaOH	2 M H_2O_2 + 0.5 M H_2SO_4	60	1.77	107	0.82	[131]
Pd/MWCNT	Pt/MWCNTs [2]	5 wt.% $NaBH_4$ + 10 wt.% NaOH	5 wt.% H_2O_2 + 5 wt.% H_2PO_4	25	1.80	119	0.58	[128]

[1] Ni@Pd (core@shell structure) supported on polyaniline (PANI). [2] Pt supported on multiwalled carbon nanotubes (MWCNTs).

PdAuNi/C_{SBIPA} exhibited the best performance among the presented electrocatalysts, even when compared with the typical (and expensive) electrocatalysts exclusively composed of noble metals (e.g., Pd [128], Au/C [129]). It shows that the alloying effect, especially between noble and low-cost metals, is one of the best ways to decrease the price of electrocatalysts while increasing their catalytic activity. In fact, the highest activity of PdAuNi/C_{SBIPA} towards BOR, i.e., the most pronounced synergistic effect, might be due to the complete mixing of three metals by the SBIPA procedure, as indicated by XRD analysis. Furthermore, XRD and XPS analysis indicated the decrease of adsorbate-Pd bond strength that could lead to faster release and subsequent oxidation of the reaction intermediates. Thus, PdAuNi/C_{SBIPA} was demonstrated to be 1.5 and 1.6 times more active (in terms of current density) for BOR than Ni@Pd/PANI [130] and PtNi/C [131] electrocatalysts, which reflects the advantage of using a trimetallic alloy, probably due to the mentioned synergic effect. Carbon-supported $Au_xNi_yCu_z$ trimetallic electrocatalysts [119] exhibited better results than PdAuNi/C_{SBIPA} at high Au amounts (Au_2NiCu). For the other compositions, PdAuNi/C_{SBIPA} was demonstrated to be a more effective anode, showing that the affinity between the metals is crucial to promote a notable alloying effect.

4. Conclusions

PdAuNi carbon-supported trimetallic catalysts were successfully synthesized by three different routes. A PdAuNi/C_{SBIPA} catalyst, synthesized via reduction using a $NaBH_4$-2-propanol complex, presented the best alloying effect, while the other two materials showed the presence of segregated Ni species, as confirmed by XRD, TEM, and XPS analyses. The results obtained from CV and LSV measurements revealed that the catalysts performed well towards BOR. The PdAuNi/C_{SBIPA} catalyst exhibited the highest activity, evidenced by the high number of exchanged electrons amounting to 7.1, and the lowest apparent activation energy (ca. 16.7 kJ mol^{-1}). Furthermore, DBPFC operating at two different temperatures (25 and 75 °C) employing a PdAuNi/C_{SBIPA} anode showed a maximum power density of 47.5 mW cm^{-2} at 25 °C, with a significant improvement with a temperature increase and peak power density of 175 mW cm^{-2} at 75 °C. Considering the economic benefits of alloying and using support materials, and the results obtained herein, it can be concluded that PdAuNi/C_{SBIPA} is an interesting candidate for the application in DBPFC as anode material.

Supplementary Materials: The following are available online at https://www.mdpi.com/article/10.3390/nano11061441/s1, Figure S1: (A) Pd, (B) Au, and (C) Ni elemental maps of PdAuNi/$C_{3\text{-step}}$ obtained by EDX spectroscopy at 20 kV, Figure S2: TEM images of Pd/C_{SBIPA} electrocatalyst, Figure S3: TEM image of PdAuNi/C_{SBIPA} electrocatalyst, Figure S4: TEM image of PdAuNi/C_{SBEG} electrocatalyst, Figure S5: TEM images of PdAuNi/$C_{3\text{-step}}$ electrocatalyst, Figure S6: XPS survey spectra of Pd/C_{SBIPA}, PdAuNi/C_{SBIPA}, PdAuNi/C_{SBEG}, and PdAuNi/$C_{3\text{-step}}$, Figure S7: CVs (third cycle) in 2 M NaOH + 0.03 M $NaBH_4$ for (A) PdAuNi/C_{SBEG}, (B) PdAuNi/C_{SBIPA}, and (C) PdAuNi/$C_{3\text{-step}}$ electrocatalysts and (D) comparative CVs of trimetallic and Pd/C_{SBIPA} monometallic catalysts. CVs run at 50 mV s^{-1} and 25 °C, Figure S8: CVs of PdAuNi/C_{SBIPA} at (A) different scan rates, ν, and the derived E_p vs. ln ν plots (inset), (B) different $NaBH_4$ concentrations and the derived ln j vs. ln c plots (inset), (C) different temperatures and the derived Arrhenius plots (inset), and (D) LSVs of PdAuNi/C_{SBIPA} at 10 mV s^{-1} and different rotation rates and the derived Koutecky–Levich plot (inset). The electrolyte solution used was 0.03 M $NaBH_4$ + 2 M NaOH, polarization rate was 50 mV s^{-1}, and room temperature (25 °C), unless otherwise noted, Figure S9: (A) Polarization and power density curves at 25 and 75 °C for a DBPFC using a PdAuNi/C_{SBIPA} anode and a Pt cathode. The cathode and anode potentials, their potential difference, and E_{cell} are also represented at (B) 25 °C and (C) 75 °C., Table S1: XPS elemental peaks of Pd 3d, Au 4f, and Ni 2p in Pd/C_{SBIPA}, PdAuNi/C_{SBIPA}, PdAuNi/C_{SBEG}, and PdAuNi/$C_{3\text{-step}}$.

Author Contributions: Conceptualization, C.A.C.S., B.Š., J.M., and D.M.F.S.; formal analysis, A.M.A.E., G.B., and R.C.P.O.; investigation, A.M.A.E. and G.B.; writing—original draft preparation, A.M.A.E., G.B., R.C.P.O., and C.A.C.S.; writing—review and editing, J.M., B.Š., and D.M.F.S., visualization, A.M.A.E., R.C.P.O. and D.M.F.S.; supervision, J.M., B.Š., and D.M.F.S. All authors have read and agreed to the published version of the manuscript.

Funding: This research was funded by a Newton-Mosharafa Scholarship NMJ8/15 (A. Elsheikh) and by the Portuguese Foundation for Science and Technology (FCT, Portugal) through a research grant within project UID/CTM/04540/2013 (G. Backović), a research contract in the scope of programmatic funding UIDP/04540/2020 (D.M.F. Santos), a Ph.D. grant SFRH/BD/137470/2018 (R.C.P. Oliveira), and contract no. IST-ID/156/2018 (B. Šljukić).

Data Availability Statement: The data presented in this study are available on request from the corresponding author.

Conflicts of Interest: The authors declare no conflict of interests. The funders had no role in the design of the study; in the collection, analyses, or interpretation of data; in the writing of the manuscript, or in the decision to publish the results.

References

1. Larminie, J.; Dicks, A. *Fuel Cell Systems Explained*, 3rd ed.; John Wiley & Sons Ltd.: London, UK, 2018. [CrossRef]
2. Kreuer, K.D. Fuel Cells, Introduction. In *Fuel Cells*; Kreuer, K.D., Ed.; Springer: New York, NY, USA, 2013. [CrossRef]
3. Maiyalagan, T.; Saji, V.S. *Electrocatalysts for Low Temperature Fuel Cells*; Wiley-VCH Verlag GmbH & Co. KGaA: Weinheim, Germany, 2017. [CrossRef]
4. Akay, R.G.; Yurtcan, A.B. *Direct Liquid Fuel Cells: Fundamentals, Advances and Future*, 1st ed.; Academic Press: Cambridge, MA, USA, 2020. [CrossRef]
5. Demirci, U.B. Direct borohydride fuel cell: Main issues met by the membrane–electrodes-assembly and potential solutions. *J. Power Sources* **2007**, *172*, 676–687. [CrossRef]
6. Indig, M.E.; Snyder, R.N. Sodium Borohydride, An Interesting Anodic Fuel (1). *J. Electrochem. Soc.* **1962**, *109*, 1104–1106. [CrossRef]
7. Vielstich, W.; Lamm, A.; Gasteiger, H. *Handbook of Fuel Cells: Fundamentals, Technology, Applications, 4 Volume Set*; John Wiley & Sons, Inc.: Hoboken, NJ, USA, 2003.
8. Ma, J.; Choudhury, N.A.; Sahai, Y. A comprehensive review of direct borohydride fuel cells. *Renew. Sustain. Energy Rev.* **2010**, *14*, 183–199. [CrossRef]
9. de Leon, C.P.; Walsh, F.; Pletcher, D.; Browning, D.; Lakeman, J. Direct borohydride fuel cells. *J. Power Sources* **2006**, *155*, 172–181. [CrossRef]
10. Ong, B.; Kamarudin, S.; Basri, S. Direct liquid fuel cells: A review. *Int. J. Hydrogen Energy* **2017**, *42*, 10142–10157. [CrossRef]
11. Rostamikia, G.; Janik, M.J. Direct borohydride oxidation: Mechanism determination and design of alloy catalysts guided by density functional theory. *Energy Environ. Sci.* **2010**, *3*, 1262–1274. [CrossRef]
12. Santos, D.M.F.; Sequeira, C.A.C. Cyclic voltammetry investigation of borohydride oxidation at a gold electrode. *Electrochim. Acta* **2010**, *55*, 6775–6781. [CrossRef]
13. Lima, F.H.; Pasqualeti, A.M.; Concha, M.B.M.; Chatenet, M.; Ticianelli, E.A. Borohydride electrooxidation on Au and Pt electrodes. *Electrochim. Acta* **2012**, *84*, 202–212. [CrossRef]
14. Arevalo, R.L.; Escaño, M.C.S.; Wang, A.Y.-S.; Kasai, H. Structure and stability of borohydride on Au(111) and Au3M(111) (M = Cr, Mn, Fe, Co, Ni) surfaces. *Dalton Trans.* **2013**, *42*, 770–775. [CrossRef]
15. He, P.; Wang, Y.; Wang, X.; Pei, F.; Wang, H.; Liu, L.; Yi, L. Investigation of carbon supported Au–Ni bimetallic nanoparticles as electrocatalyst for direct borohydride fuel cell. *J. Power Sources* **2011**, *196*, 1042–1047. [CrossRef]
16. Liu, J.; Zhao, Q.; Wu, C.; Wang, Y.; Wei, W.; Wang, X.; Yi, L. Performance improvement of activated nanoporous carbon supported gold catalyst as an anode for direct borohydride–hydrogen peroxide fuel cells. *RSC Adv.* **2014**, *4*, 17129–17135. [CrossRef]
17. Yi, L.; Liu, L.; Wang, X.; Liu, X.; Yi, W.; Wang, X. Carbon supported Pt–Sn nanoparticles as anode catalyst for direct borohydride–hydrogen peroxide fuel cell: Electrocatalysis and fuel cell performance. *J. Power Sources* **2013**, *224*, 6–12. [CrossRef]
18. Oliveira, R.C.P.; Milikić, J.; Daş, E.; Yurtcan, A.B.; Santos, D.M.F.; Šljukić, B. Platinum/polypyrrole-carbon electrocatalysts for direct borohydride-peroxide fuel cells. *Appl. Catal. B Environ.* **2018**, *238*, 454–464. [CrossRef]
19. Freitas, K.S.; Concha, B.M.; Ticianelli, E.A.; Chatenet, M. Mass transport effects in the borohydride oxidation reaction—Influence of the residence time on the reaction onset and faradaic efficiency. *Catal. Today* **2011**, *170*, 110–119. [CrossRef]
20. Olu, P.-Y.; Barros, C.R.; Job, N.; Chatenet, M. Electrooxidation of NaBH4 in Alkaline Medium on Well-defined Pt Nanoparticles Deposited onto Flat Glassy Carbon Substrate: Evaluation of the Effects of Pt Nanoparticle Size, Inter-Particle Distance, and Loading. *Electrocatalysis* **2014**, *5*, 288–300. [CrossRef]
21. Šljukić, B.; Milikić, J.; Santos, D.M.F.; Sequeira, C.A.C.; Macciò, D.; Saccone, A. Electrocatalytic performance of Pt–Dy alloys for direct borohydride fuel cells. *J. Power Sources* **2014**, *272*, 335–343. [CrossRef]

22. Šljukić, B.; Milikić, J.; Santos, D.M.F.; Sequeira, C.A.C. Carbon-supported Pt0.75M0.25 (M=Ni or Co) electrocatalysts for borohydride oxidation. *Electrochim. Acta* **2013**, *107*, 577–583. [CrossRef]
23. Concha, B.M.; Chatenet, M. Direct oxidation of sodium borohydride on Pt, Ag and alloyed Pt–Ag electrodes in basic media. *Electrochim. Acta* **2009**, *54*, 6130–6139. [CrossRef]
24. Gyenge, E.; Atwan, M.; Northwood, D. Electrocatalysis of Borohydride Oxidation on Colloidal Pt and Pt-Alloys (Pt-Ir, Pt-Ni, and Pt-Au) and Application for Direct Borohydride Fuel Cell Anodes. *J. Electrochem. Soc.* **2006**, *153*, A150–A158. [CrossRef]
25. Santos, D.M.F.; Šljukić, B.; Amaral, L.; Macciò, D.; Saccone, A.; Sequeira, C.A.C. Nickel and Nickel-Cerium Alloy Anodes for Direct Borohydride Fuel Cells. *J. Electrochem. Soc.* **2014**, *161*, F594–F599. [CrossRef]
26. Hosseini, M.G.; Abdolmaleki, M.; Ashrafpoor, S. Electrocatalytic Oxidation of Sodium Borohydride on a Nanoporous Ni/Zn-Ni Electrode. *Chin. J. Catal.* **2012**, *33*, 1817–1824. [CrossRef]
27. Santos, D.M.F.; Sequeira, C.A.C. Zinc Anode for Direct Borohydride Fuel Cells. *J. Electrochem. Soc.* **2010**, *157*, B13–B19. [CrossRef]
28. Vinayan, B.P.; Jafri, R.I.; Nagar, R.; Rajalakshmi, N.; Sethupathi, K.; Ramaprabhu, S. Catalytic activity of platinum–cobalt alloy nanoparticles decorated functionalized multiwalled carbon nanotubes for oxygen reduction reaction in PEMFC. *Int. J. Hydrogen Energy* **2012**, *37*, 412–421. [CrossRef]
29. Rao, C.S.; Singh, D.; Sekhar, R.; Rangarajan, J. Pt–Co electrocatalyst with varying atomic percentage of transition metal. *Int. J. Hydrogen Energy* **2011**, *36*, 14805–14814. [CrossRef]
30. Tegou, A.; Papadimitriou, S.; Mintsouli, I.; Armyanov, S.; Valova, E.; Kokkinidis, G.; Sotiropoulos, S. Rotating disc electrode studies of borohydride oxidation at Pt and bimetallic Pt–Ni and Pt–Co electrodes. *Catal. Today* **2011**, *170*, 126–133. [CrossRef]
31. Šljukić, B.; Santos, D.M.F. Direct Borohydride Fuel Cells. In *Direct Liquid Fuel Cells: Fundamentals. Advances and Future*, 1st ed.; Akay, R.G., Yurtcan, A.B., Eds.; Academic Press: Cambridge, MA, USA, 2020; pp. 203–232. [CrossRef]
32. Chatenet, M.; Lima, F.H.B.; Ticianelli, E.A. Gold is not a Faradaic-Efficient Borohydride Oxidation Electrocatalyst: An Online Electrochemical Mass Spectrometry Study. *J. Electrochem. Soc.* **2010**, *157*, B697–B704. [CrossRef]
33. Braesch, G.; Bonnefont, A.; Martin, V.; Savinova, E.R.; Chatenet, M. Borohydride oxidation reaction mechanisms and poisoning effects on Au, Pt and Pd bulk electrodes: From model (low) to direct borohydride fuel cell operating (high) concentrations. *Electrochim. Acta* **2018**, *273*, 483–494. [CrossRef]
34. Tamašauskaitė-Tamašiūnaitė, L.; Radomskis, A.; Antanavičiūtė, K.; Jablonskienė, J.; Balciunaite, A.; Žielienė, A.; Naruškevičius, L.; Kondrotas, R.; Norkus, E. Graphene supported platinum–cobalt nanocomposites as electrocatalysts for borohydride oxidation. *Int. J. Hydrogen Energy* **2014**, *39*, 4282–4290. [CrossRef]
35. He, P.; Wang, X.; Liu, Y.; Liu, X.; Yi, L. Comparison of electrocatalytic activity of carbon-supported Au–M (M = Fe, Co, Ni, Cu and Zn) bimetallic nanoparticles for direct borohydride fuel cells. *Int. J. Hydrogen Energy* **2012**, *37*, 11984–11993. [CrossRef]
36. Modibedi, R.M.; Masombuka, T.; Mathe, M. Carbon supported Pd–Sn and Pd–Ru–Sn nanocatalysts for ethanol electro-oxidation in alkaline medium. *Int. J. Hydrogen Energy* **2011**, *36*, 4664–4672. [CrossRef]
37. Antolini, E. Palladium in fuel cell catalysis. *Energy Environ. Sci.* **2009**, *2*, 915–931. [CrossRef]
38. Huang, Y.; Guo, Y.; Wang, Y.; Yao, J. Synthesis and performance of a novel PdCuPb/C nanocatalyst for ethanol electrooxidation in alkaline medium. *Int. J. Hydrogen Energy* **2014**, *39*, 4274–4281. [CrossRef]
39. Zheng, Y.; Qiao, J.; Yuan, J.; Shen, J.; Wang, A.-J.; Huang, S. Controllable synthesis of PtPd nanocubes on graphene as advanced catalysts for ethanol oxidation. *Int. J. Hydrogen Energy* **2018**, *43*, 4902–4911. [CrossRef]
40. Yang, G.; Zhou, Y.; Pan, H.-B.; Zhu, C.; Fu, S.; Wai, C.M.; Du, D.; Zhu, J.-J.; Lin, Y. Ultrasonic-assisted synthesis of Pd–Pt/carbon nanotubes nanocomposites for enhanced electro-oxidation of ethanol and methanol in alkaline medium. *Ultrason. Sonochemistry* **2016**, *28*, 192–198. [CrossRef] [PubMed]
41. Brouzgou, A.; Podias, A.; Tsiakaras, P. PEMFCs and AEMFCs directly fed with ethanol: A current status comparative review. *J. Appl. Electrochem.* **2013**, *43*, 119–136. [CrossRef]
42. Santos, D.M.F.; Sequeira, C.A.C. Sodium borohydride determination by measurement of open circuit potentials. *J. Electroanal. Chem.* **2009**, *627*, 1–8. [CrossRef]
43. Hong, J.; Fang, B.; Wang, C.; Currie, K. Zn-Air Fuel Cell/Battery Hybrid Power Sources with Addition of Borohydride. *ECS Trans.* **2006**, *3*, 89–99. [CrossRef]
44. Hong, J.; Fang, B.; Wang, C.; Currie, K. Intrinsic borohydride fuel cell/battery hybrid power sources. *J. Power Sources* **2006**, *161*, 753–760. [CrossRef]
45. Wang, X.; Xia, Y. Electrocatalytic performance of PdCo–C catalyst for formic acid oxidation. *Electrochem. Commun.* **2008**, *10*, 1644–1646. [CrossRef]
46. Sheng, G.; Chen, J.; Ye, H.; Hu, Z.; Fu, X.-Z.; Sun, R.; Huang, W.; Wong, C.-P. Hollow PdCo alloy nanospheres with mesoporous shells as high-performance catalysts for methanol oxidation. *J. Colloid Interface Sci.* **2018**, *522*, 264–271. [CrossRef]
47. Martins, M.; Šljukić, B.; Metin, Ö.; Sevim, M.; Sequeira, C.A.C.; Şener, T.; Santos, D.M.F. Bimetallic PdM (M = Fe, Ag, Au) alloy nanoparticles assembled on reduced graphene oxide as catalysts for direct borohydride fuel cells. *J. Alloys Compd.* **2017**, *718*, 204–214. [CrossRef]
48. Martins, M.; Metin, Ö.; Sevim, M.; Šljukić, B.; Sequeira, C.A.C.; Sener, T.; Santos, D.M.F. Monodisperse Pd nanoparticles assembled on reduced graphene oxide-Fe_3O_4 nanocomposites as electrocatalysts for borohydride fuel cells. *Int. J. Hydrogen Energy* **2018**, *43*, 10686–10697. [CrossRef]

49. Simões, M.; Baranton, S.; Coutanceau, C. Electrooxidation of Sodium Borohydride at Pd, Au, and Pd_XAu_{1-x} Carbon-Supported Nanocatalysts. *J. Phys. Chem. C* **2009**, *113*, 13369–13376. [CrossRef]
50. Jimenez, I.M.; Janik, M.; De Leon, C.P.; Walsh, F. Pd–Ir alloy as an anode material for borohydride oxidation. *J. Power Sources* **2014**, *269*, 498–508. [CrossRef]
51. Grimmer, C.; Grandi, M.; Zacharias, R.; Cermenek, B.; Weber, H.; Morais, C.; Napporn, T.W.; Weinberger, S.; Schenk, A.; Hacker, V. The electrooxidation of borohydride: A mechanistic study on palladium (Pd/C) applying RRDE, 11B-NMR and FTIR. *Appl. Catal. B Environ.* **2016**, *180*, 614–621. [CrossRef]
52. Šljukić, B.; Martins, M.; Kayhan, E.; Balčiūnaitė, A.; Şener, T.; Sequeira, C.A.C.; Santos, D.M.F. SnO_2-C supported PdNi nanoparticles for oxygen reduction and borohydride oxidation. *J. Electroanal. Chem.* **2017**, *797*, 23–30. [CrossRef]
53. Milikić, J.; Ćirić-Marjanović, G.; Mentus, S.; Santos, D.M.F.; Sequeira, C.A.C.; Šljukić, B. Pd/c-PANI electrocatalysts for direct borohydride fuel cells. *Electrochim. Acta* **2016**, *213*, 298–305. [CrossRef]
54. Martins, M.; Šljukić, B.; Sequeira, C.A.C.; Metin, Ö.; Erdem, M.; Sener, T.; Santos, D.M.F. Biobased carbon-supported palladium electrocatalysts for borohydride fuel cells. *Int. J. Hydrogen Energy* **2016**, *41*, 10914–10922. [CrossRef]
55. Uosaki, K. *Electrochemical Science for a Sustainable Society: A Tribute to John O'M Bockris*, 1st ed.; Springer International Publishing: New York, NY, USA, 2017. [CrossRef]
56. Lv, H.; Sun, L.; Zou, L.; Xu, D.; Yao, H.; Liu, B. Size-dependent synthesis and catalytic activities of trimetallic PdAgCu mesoporous nanospheres in ethanol electrooxidation. *Chem. Sci.* **2019**, *10*, 1986–1993. [CrossRef] [PubMed]
57. Amin, R.; Hameed, R.A.; El-Khatib, K.; Youssef, M.E. Electrocatalytic activity of nanostructured Ni and Pd–Ni on Vulcan XC-72R carbon black for methanol oxidation in alkaline medium. *Int. J. Hydrogen Energy* **2014**, *39*, 2026–2041. [CrossRef]
58. Obradović, M.; Stančić, Z.; Lačnjevac, U.; Radmilovic, V.; Gavrilović-Wohlmuther, A.; Gojković, S. Electrochemical oxidation of ethanol on palladium-nickel nanocatalyst in alkaline media. *Appl. Catal. B Environ.* **2016**, *189*, 110–118. [CrossRef]
59. Dutta, A.; Datta, J. Energy efficient role of Ni/NiO in PdNi nano catalyst used in alkaline DEFC. *J. Mater. Chem. A* **2014**, *2*, 3237–3250. [CrossRef]
60. Shen, S.; Zhao, T.S.; Xu, J.; Li, Y. High performance of a carbon supported ternary PdIrNi catalyst for ethanol electro-oxidation in anion-exchange membrane direct ethanol fuel cells. *Energy Environ. Sci.* **2011**, *4*, 1428–1433. [CrossRef]
61. Yurderi, M.; Bulut, A.; Zahmakiran, M.; Kaya, M. Carbon supported trimetallic PdNiAg nanoparticles as highly active, selective and reusable catalyst in the formic acid decomposition. *Appl. Catal. B Environ.* **2014**, *160*, 514–524. [CrossRef]
62. Zhu, W.; Ke, J.; Wang, S.-B.; Ren, J.; Wang, H.-H.; Zhou, Z.-Y.; Si, R.; Zhang, Y.-W.; Yan, C.-H. Shaping Single-Crystalline Trimetallic Pt–Pd–Rh Nanocrystals toward High-Efficiency C–C Splitting of Ethanol in Conversion to CO_2. *ACS Catal.* **2015**, *5*, 1995–2008. [CrossRef]
63. Hu, S.; Munoz, F.; Noborikawa, J.; Haan, J.; Scudiero, L.; Ha, S. Carbon supported Pd-based bimetallic and trimetallic catalyst for formic acid electrochemical oxidation. *Appl. Catal. B Environ.* **2016**, *180*, 758–765. [CrossRef]
64. Sharma, G.; Kumar, D.; Kumar, A.; Al-Muhtaseb, A.H.; Pathania, D.; Naushad, M.; Mola, G.T. Revolution from monometallic to trimetallic nanoparticle composites, various synthesis methods and their applications: A review. *Mater. Sci. Eng. C* **2017**, *71*, 1216–1230. [CrossRef]
65. Ulas, B.; Caglar, A.; Sahin, O.; Kivrak, H. Composition dependent activity of PdAgNi alloy catalysts for formic acid electrooxidation. *J. Colloid Interface Sci.* **2018**, *532*, 47–57. [CrossRef]
66. Beyhan, S.; Léger, J.-M.; Kadırgan, F. Understanding the influence of Ni, Co, Rh and Pd addition to PtSn/C catalyst for the oxidation of ethanol by in situ Fourier transform infrared spectroscopy. *Appl. Catal. B Environ.* **2014**, *144*, 66–74. [CrossRef]
67. Shang, C.; Hong, W.; Wang, J.; Wang, E. Carbon supported trimetallic nickel–palladium–gold hollow nanoparticles with superior catalytic activity for methanol electrooxidation. *J. Power Sources* **2015**, *285*, 12–15. [CrossRef]
68. Dutta, A.; Datta, J. Outstanding Catalyst Performance of PdAuNi Nanoparticles for the Anodic Reaction in an Alkaline Direct Ethanol (with Anion-Exchange Membrane) Fuel Cell. *J. Phys. Chem. C* **2012**, *116*, 25677–25688. [CrossRef]
69. Su, P.-C.; Chen, H.-S.; Chen, T.-Y.; Liu, C.-W.; Lee, C.-H.; Lee, J.-F.; Chan, T.-S.; Wang, K.-W. Enhancement of electrochemical properties of Pd/C catalysts toward ethanol oxidation reaction in alkaline solution through Ni and Au alloying. *Int. J. Hydrogen Energy* **2013**, *38*, 4474–4482. [CrossRef]
70. Lu, L.; Kang, J. Amperometric nonenzymatic sensing of glucose at very low working potential by using a nanoporous PdAuNi ternary alloy. *Microchim. Acta* **2018**, *185*, 111. [CrossRef] [PubMed]
71. Bulut, A.; Yurderi, M.; Kaya, M.; Aydemir, M.; Baysal, A.; Durap, F.; Zahmakiran, M. Amine-functionalized graphene nanosheet-supported PdAuNi alloy nanoparticles: Efficient nanocatalyst for formic acid dehydrogenation. *New J. Chem.* **2018**, *42*, 16103–16114. [CrossRef]
72. Li, S.; Lai, J.; Luque, R.; Xu, G. Designed multimetallic Pd nanosponges with enhanced electrocatalytic activity for ethylene glycol and glycerol oxidation. *Energy Environ. Sci.* **2016**, *9*, 3097–3102. [CrossRef]
73. Chatenet, M.; Molina-Concha, M.; Diard, J.-P. First insights into the borohydride oxidation reaction mechanism on gold by electrochemical impedance spectroscopy. *Electrochim. Acta* **2009**, *54*, 1687–1693. [CrossRef]
74. Nagle, L.C.; Rohan, J. Nanoporous gold anode catalyst for direct borohydride fuel cell. *Int. J. Hydrogen Energy* **2011**, *36*, 10319–10326. [CrossRef]

75. Tegou, A.; Armyanov, S.; Valova, E.; Steenhaut, O.; Hubin, A.; Kokkinidis, G.; Sotiropoulos, S. Mixed platinum–gold electrocatalysts for borohydride oxidation prepared by the galvanic replacement of nickel deposits. *J. Electroanal. Chem.* **2009**, *634*, 104–110. [CrossRef]
76. Parrour, G.; Chatenet, M.; Diard, J.-P. Electrochemical impedance spectroscopy study of borohydride oxidation reaction on gold—Towards a mechanism with two electrochemical steps. *Electrochim. Acta* **2010**, *55*, 9113–9124. [CrossRef]
77. Santos, D.M.F.; Sequeira, C.A.C. Chronopotentiometric Investigation of Borohydride Oxidation at a Gold Electrode. *J. Electrochem. Soc.* **2010**, *157*, F16–F21. [CrossRef]
78. Zhang, D.; Cheng, K.; Shi, N.; Guo, F.; Wang, G.; Cao, D. Nickel particles supported on multi-walled carbon nanotubes modified sponge for sodium borohydride electrooxidation. *Electrochem. Commun.* **2013**, *35*, 128–130. [CrossRef]
79. Santos, D.M.F.; Šljukić, B.; Amaral, L.; Milikić, J.; Sequeira, C.A.C.; Macciò, D.; Saccone, A. Nickel–rare earth electrodes for sodium borohydride electrooxidation. *Electrochim. Acta* **2016**, *190*, 1050–1056. [CrossRef]
80. Oshchepkov, A.G.; Braesch, G.; Ould-Amara, S.; Rostamikia, G.; Maranzana, G.; Bonnefont, A.; Papaefthimiou, V.; Janik, M.J.; Chatenet, M.; Savinova, E.R. Nickel Metal Nanoparticles as Anode Electrocatalysts for Highly Efficient Direct Borohydride Fuel Cells. *ACS Catal.* **2019**, *9*, 8520–8528. [CrossRef]
81. Chen, A.; Ostrom, C. Palladium-Based Nanomaterials: Synthesis and Electrochemical Applications. *Chem. Rev.* **2015**, *115*, 11999–12044. [CrossRef]
82. Zhang, Z.; Dong, Y.; Wang, L.; Wang, S. Scalable synthesis of a Pd nanoparticle loaded hierarchically porous graphene network through multiple synergistic interactions. *Chem. Commun.* **2015**, *51*, 8357–8360. [CrossRef] [PubMed]
83. Corradini, P.G.; Pires, F.I.; Paganin, V.A.; Perez, J.; Antolini, E. Effect of the relationship between particle size, inter-particle distance, and metal loading of carbon supported fuel cell catalysts on their catalytic activity. *J. Nanoparticle Res.* **2012**, *14*, 1–9. [CrossRef]
84. Modibedi, R.M.; Mehlo, T.; Ozoemena, K.I.; Mathe, M. Preparation, characterisation and application of Pd/C nanocatalyst in passive alkaline direct ethanol fuel cells (ADEFC). *Int. J. Hydrogen Energy* **2015**, *40*, 15605–15612. [CrossRef]
85. Kim, P.; Joo, J.B.; Kim, W.; Kim, J.; Song, I.K.; Yi, J. NaBH4-assisted ethylene glycol reduction for preparation of carbon-supported Pt catalyst for methanol electro-oxidation. *J. Power Sources* **2006**, *160*, 987–990. [CrossRef]
86. Henrique, R.S.; Ayoub, J.M.S.; Piasentin, R.M.; Linardi, M.; Santos, M.C. Preparation of $Pt/C\text{-}In_2O_3.SnO_2$ electrocatalysts by borohydride reduction process for ethanol electro-oxidation. *Int. J. Electrochem. Sci.* **2012**, *7*, 2036–2046. [CrossRef]
87. Assumpção, M.; da Silva, S.; De Souza, R.; Buzzo, G.; Spinacé, E.; Santos, M.; Neto, A.; Silva, J. Investigation of PdIr/C electrocatalysts as anode on the performance of direct ammonia fuel cell. *J. Power Sources* **2014**, *268*, 129–136. [CrossRef]
88. Miller, S.D.; İnoğlu, N.; Kitchin, J. Configurational correlations in the coverage dependent adsorption energies of oxygen atoms on late transition metal fcc(111) surfaces. *J. Chem. Phys.* **2011**, *134*, 104709. [CrossRef]
89. Counsell, J.D.P. Surface Science Studies of Adsorption and Reactivity of Pd (111) and Au-Pd (111). Ph.D. Thesis, Cardiff University, Cardiff, Wales, UK, 2010.
90. Naresh, N.; Wasim, F.G.S.; Ladewig, B.P.; Neergat, M. Removal of surfactant and capping agent from Pd nanocubes (Pd-NCs) using tert-butylamine: Its effect on electrochemical characteristics. *J. Mater. Chem. A* **2013**, *1*, 8553–8559. [CrossRef]
91. Zhang, X.-J.; Zhang, J.-M.; Zhang, P.-Y.; Li, Y.; Xiang, S.; Tang, H.-G.; Fan, Y.-J. Highly active carbon nanotube-supported Ru@Pd core-shell nanostructure as an efficient electrocatalyst toward ethanol and formic acid oxidation. *Mol. Catal.* **2017**, *436*, 138–144. [CrossRef]
92. Qiu, X.; Dai, Y.; Tang, Y.; Lu, T.; Wei, S.; Chen, Y. One-pot synthesis of gold–palladium@palladium core–shell nanoflowers as efficient electrocatalyst for ethanol electrooxidation. *J. Power Sources* **2015**, *278*, 430–435. [CrossRef]
93. Zhou, W.; Lee, J.Y. Highly active core–shell Au@Pd catalyst for formic acid electrooxidation. *Electrochem. Commun.* **2007**, *9*, 1725–1729. [CrossRef]
94. Akhairi, M.; Kamarudin, S. Catalysts in direct ethanol fuel cell (DEFC): An overview. *Int. J. Hydrogen Energy* **2016**, *41*, 4214–4228. [CrossRef]
95. Feng, Y.-Y.; Liu, Z.-H.; Xu, Y.; Wang, P.; Wang, W.-H.; Kong, D.-S. Highly active PdAu alloy catalysts for ethanol electro-oxidation. *J. Power Sources* **2013**, *232*, 99–105. [CrossRef]
96. Feng, Y.; Bin, D.; Yan, B.; Du, Y.; Majima, T.; Zhou, W. Porous bimetallic PdNi catalyst with high electrocatalytic activity for ethanol electrooxidation. *J. Colloid Interface Sci.* **2017**, *493*, 190–197. [CrossRef]
97. Akhtar, K.; Khan, S.A.; Khan, S.B.; Asiri, A.M. Scanning Electron Microscopy: Principle and Applications in Nanomaterials Characterization. In *Handbook of Materials Characterization*; Akhtar, K., Khan, S.A., Khan, S.B., Asiri, A.M., Eds.; Springer International Publishing: Bassel, Switzerland, 2018; pp. 113–145. [CrossRef]
98. Pasqualeti, A.M.; Olu, P.-Y.; Chatenet, M.; Lima, F.H.B. Borohydride Electrooxidation on Carbon-Supported Noble Metal Nanoparticles: Insights into Hydrogen and Hydroxyborane Formation. *ACS Catal.* **2015**, *5*, 2778–2787. [CrossRef]
99. Santos, D.M.F.; Saturnino, P.; Lobo, R.F.M.; Sequeira, C.A.C. Direct borohydride/peroxide fuel cells using Prussian Blue cathodes. *J. Power Sources* **2012**, *208*, 131–137. [CrossRef]
100. Santos, D.M.F.; Sequeira, C.A.C. Effect of Membrane Separators on the Performance of Direct Borohydride Fuel Cells. *J. Electrochem. Soc.* **2011**, *159*, B126–B132. [CrossRef]
101. Lam, B.T.X.; Chiku, M.; Higuchi, E.; Inoue, H. Preparation of PdAg and PdAu nanoparticle-loaded carbon black catalysts and their electrocatalytic activity for the glycerol oxidation reaction in alkaline medium. *J. Power Sources* **2015**, *297*, 149–157. [CrossRef]

102. Zhang, S.; Qing, M.; Zhang, H.; Tian, Y. Electrocatalytic oxidation of formic acid on functional MWCNTs supported nanostructured Pd–Au catalyst. *Electrochem. Commun.* **2009**, *11*, 2249–2252. [CrossRef]
103. Liu, C.; Liu, R.-H.; Sun, Q.-J.; Chang, J.-B.; Gao, X.; Liu, Y.; Lee, S.-T.; Kang, Z.-H.; Wang, S.-D. Controlled synthesis and synergistic effects of graphene-supported PdAu bimetallic nanoparticles with tunable catalytic properties. *Nanoscale* **2015**, *7*, 6356–6362. [CrossRef]
104. Geraldes, A.N.; da Silva, D.F.; Pino, E.S.; da Silva, J.C.M.; de Souza, R.F.B.; Hammer, P.; Spinacé, E.V.; Neto, A.O.; Linardi, M.; dos Santos, M.C. Ethanol electro-oxidation in an alkaline medium using Pd/C, Au/C and PdAu/C electrocatalysts prepared by electron beam irradiation. *Electrochim. Acta* **2013**, *111*, 455–465. [CrossRef]
105. Zhang, G.; Wang, Y.; Wang, X.; Chen, Y.; Zhou, Y.; Tang, Y.; Lu, L.; Bao, J.; Lu, T. Preparation of Pd–Au/C catalysts with different alloying degree and their electrocatalytic performance for formic acid oxidation. *Appl. Catal. B Environ.* **2011**, *102*, 614–619. [CrossRef]
106. Dutta, A.; Mondal, A.; Broekmann, P.; Datta, J. Optimal level of Au nanoparticles on Pd nanostructures providing remarkable electro-catalysis in direct ethanol fuel cell. *J. Power Sources* **2017**, *361*, 276–284. [CrossRef]
107. Qin, Y.-H.; Jiang, Y.; Niu, D.-F.; Zhang, X.-S.; Zhou, X.-G.; Niu, L.; Yuan, W.-K. Carbon nanofiber supported bimetallic PdAu nanoparticles for formic acid electrooxidation. *J. Power Sources* **2012**, *215*, 130–134. [CrossRef]
108. Yin, Z.; Chi, M.; Zhu, Q.; Ma, D.; Sun, J.; Bao, X. Supported bimetallic PdAu nanoparticles with superior electrocatalytic activity towards methanol oxidation. *J. Mater. Chem. A* **2013**, *1*, 9157–9163. [CrossRef]
109. Zhang, Z.; Xin, L.; Sun, K.; Li, W. Pd–Ni electrocatalysts for efficient ethanol oxidation reaction in alkaline electrolyte. *Int. J. Hydrogen Energy* **2011**, *36*, 12686–12697. [CrossRef]
110. Holade, Y.; Sahin, N.E.; Servat, K.; Napporn, T.W.; Kokoh, K.B. Recent Advances in Carbon Supported Metal Nanoparticles Preparation for Oxygen Reduction Reaction in Low Temperature Fuel Cells. *Catalysts* **2015**, *5*, 310–348. [CrossRef]
111. Zhu, C.; Wen, D.; Oschatz, M.; Holzschuh, M.; Liu, W.; Herrmann, A.-K.; Simon, F.; Kaskel, S.; Eychmüller, A. Kinetically Controlled Synthesis of PdNi Bimetallic Porous Nanostructures with Enhanced Electrocatalytic Activity. *Small* **2015**, *11*, 1430–1434. [CrossRef] [PubMed]
112. Chen, W.; Zhang, Y.; Wei, X. Catalytic performances of PdNi/MWCNT for electrooxidations of methanol and ethanol in alkaline media. *Int. J. Hydrogen Energy* **2015**, *40*, 1154–1162. [CrossRef]
113. Ramulifho, T.; Ozoemena, K.I.; Modibedi, R.M.; Jafta, C.J.; Mathe, M. Electrocatalytic oxidation of ethylene glycol at palladium-bimetallic nanocatalysts (PdSn and PdNi) supported on sulfonate-functionalised multi-walled carbon nanotubes. *J. Electroanal. Chem.* **2013**, *692*, 26–30. [CrossRef]
114. Chen, L.Y.; Chen, N.; Hou, Y.; Wang, Z.C.; Lv, S.H.; Fujita, T.; Jiang, J.H.; Hirata, A.; Chen, M. Geometrically Controlled Nanoporous PdAu Bimetallic Catalysts with Tunable Pd/Au Ratio for Direct Ethanol Fuel Cells. *ACS Catal.* **2013**, *3*, 1220–1230. [CrossRef]
115. Behmenyar, G.; Akın, A.N. Investigation of carbon supported Pd–Cu nanoparticles as anode catalysts for direct borohydride fuel cell. *J. Power Sources* **2014**, *249*, 239–246. [CrossRef]
116. Park, S.Y.; Lee, D.-W.; Park, I.S.; Hong, Y.-K.; Park, Y.-M.; Lee, K.-Y. The effective bimetallic component of Pd–Au/C for electrochemical oxidation of borohydrides. *Curr. Appl. Phys.* **2010**, *10*, S40–S43. [CrossRef]
117. He, P.; Wang, X.; Liu, Y.; Yi, L.; Liu, X. Reverse micelle synthesis of AuNi alloy as electrocatalyst of borohydride oxidation. *Int. J. Hydrogen Energy* **2012**, *37*, 1254–1262. [CrossRef]
118. Yang, J.Q.; Liu, B.H.; Wu, S. Carbon-supported Pd catalysts: Influences of nanostructure on their catalytic performances for borohydride electrochemical oxidation. *J. Power Sources* **2009**, *194*, 824–829. [CrossRef]
119. Duan, D.; Yin, X.; Wang, Q.; Liu, S.; Wang, Y. Performance evaluation of borohydride electrooxidation reaction with ternary alloy Au–Ni–Cu/C catalysts. *J. Appl. Electrochem.* **2018**, *48*, 835–847. [CrossRef]
120. Antolini, E. Structural parameters of supported fuel cell catalysts: The effect of particle size, inter-particle distance and metal loading on catalytic activity and fuel cell performance. *Appl. Catal. B Environ.* **2016**, *181*, 298–313. [CrossRef]
121. Bard, A.J.; Faulkner, L.R. *Electrochemical Methods: Fundamentals and Applications*, 2nd ed.; John Wiley & Sons, Inc.: New York, NY, USA, 2001. [CrossRef]
122. Wei, J.; Wang, X.; Wang, Y.; Chen, Q.; Pei, F.; Wang, Y. Investigation of carbon-supported Au hollow nanospheres as electrocatalyst for electrooxidation of sodium borohydride. *Int. J. Hydrogen Energy* **2009**, *34*, 3360–3366. [CrossRef]
123. Wang, K.; Lu, J.; Zhuang, L. A Current−Decomposition Study of the Borohydride Oxidation Reaction at Ni Electrodes. *J. Phys. Chem. C* **2007**, *111*, 7456–7462. [CrossRef]
124. Hosseini, M.G.; Abdolmaleki, M. Synthesis and characterization of porous nanostructured Ni/PdNi electrode towards electrooxidation of borohydride. *Int. J. Hydrogen Energy* **2013**, *38*, 5449–5456. [CrossRef]
125. Oliveira, R.C.P.; Vasić, M.; Santos, D.M.F.; Babić, B.; Hercigonja, R.; Sequeira, C.A.C.; Šljukić, B. Performance assessment of a direct borohydride-peroxide fuel cell with Pd-impregnated faujasite X zeolite as anode electrocatalyst. *Electrochim. Acta* **2018**, *269*, 517–525. [CrossRef]
126. Yi, L.; Song, Y.; Wang, X.; Yi, L.; Hu, J.; Su, G.; Yi, W.; Yan, H. Carbon supported palladium hollow nanospheres as anode catalysts for direct borohydride-hydrogen peroxide fuel cells. *J. Power Sources* **2012**, *205*, 63–70. [CrossRef]

127. Song, C.; Wang, G.; Li, B.; Miao, C.; Ma, K.; Zhu, K.; Cheng, K.; Ye, K.; Yan, J.; Cao, D.; et al. A novel electrode of ternary CuNiPd nanoneedles decorated Ni foam and its catalytic activity toward $NaBH_4$ electrooxidation. *Electrochim. Acta* **2019**, *299*, 395–404. [CrossRef]
128. Oh, T.H.; Jang, B.; Kwon, S. Performance evaluation of direct borohydride–hydrogen peroxide fuel cells with electrocatalysts supported on multiwalled carbon nanotubes. *Energy* **2014**, *76*, 911–919. [CrossRef]
129. Pei, F.; Wang, Y.; Wang, X.; He, P.; Chen, Q.; Wang, X.; Wang, H.; Yi, L.; Guo, J. Performance of supported Au–Co alloy as the anode catalyst of direct borohydride-hydrogen peroxide fuel cell. *Int. J. Hydrogen Energy* **2010**, *35*, 8136–8142. [CrossRef]
130. Mahmoodi, R.; Hosseini, M.G.; Rasouli, H. Enhancement of output power density and performance of direct borohydride-hydrogen peroxide fuel cell using Ni-Pd core-shell nanoparticles on polymeric composite supports (rGO-PANI) as novel electrocatalysts. *Appl. Catal. B Environ.* **2019**, *251*, 37–48. [CrossRef]
131. Hosseini, M.; Mahmoodi, R.; Amjadi, M.S. Carbon supported Ni_1Pt_1 nanocatalyst as superior electrocatalyst with increased power density in direct borohydride-hydrogen peroxide and investigation of cell impedance at different temperatures and discharging currents. *Energy* **2017**, *131*, 137–148. [CrossRef]

nanomaterials

MDPI

Article

Hydrogen Nanometrology in Advanced Carbon Nanomaterial Electrodes

Rui Lobo [1,2,*], Noe Alvarez [3] and Vesselin Shanov [4]

[1] Laboratory of Nanophysics/Nanotechnology and Energy (N2E), Center of Technology and Systems (CTS-UNINOVA), NOVA School of Science & Technology, FCT-NOVA, Universidade NOVA de Lisboa, 2829-516 Caparica, Portugal
[2] Department of Physics, NOVA School of Science & Technology, FCT-NOVA, Universidade NOVA de Lisboa, 2829-516 Caparica, Portugal
[3] Department of Chemistry, University of Cincinnati, Cincinnati, OH 45221, USA; noe.alvarez@uc.edu
[4] Department of Chemical and Environmental Engineering, University of Cincinnati, Cincinnati, OH 45221, USA; shanovvn@ucmail.uc.edu
* Correspondence: rfl@fct.unl.pt; Tel.: +351-934463400

Abstract: A comparative experimental study between advanced carbon nanostructured electrodes, in similar hydrogen uptake/desorption conditions, is investigated making use of the recent molecular beam-thermal desorption spectrometry. This technique is used for monitoring hydrogen uptake and release from different carbon electrocatalysts: 3D-graphene, single-walled carbon nanotube networks, multi-walled carbon nanotube networks, and carbon nanotube thread. It allows an accurate determination of the hydrogen mass absorbed in electrodes made from these materials, with significant enhancement in the signal-to-noise ratio for trace hydrogen avoiding recourse to ultra-high vacuum procedures. The hydrogen mass spectra account for the enhanced surface capability for hydrogen adsorption in the different types of electrode in similar uptake conditions, and confirm their enhanced hydrogen storage capacity, pointing to a great potential of carbon nanotube threads in replacing the heavier metals or metal alloys as hydrogen storage media.

Keywords: hydrogen storage; nanometrology; carbon nanotubes; graphene; nanotubes thread; desorption spectrometry

Citation: Lobo, R.; Alvarez, N.; Shanov, V. Hydrogen Nanometrology in Advanced Carbon Nanomaterial Electrodes. *Nanomaterials* **2021**, *11*, 1079. https://doi.org/10.3390/nano11051079

Academic Editor: Diego Cazorla-Amorós

Received: 13 March 2021
Accepted: 20 April 2021
Published: 22 April 2021

1. Introduction

The development of a sustainable energy system is one of the most important challenges today and electrocatalytic hydrogen evolution is one of the most important ways to develop a sustainable energy system based on hydrogen technologies [1]. Together with suitable safe storage methods, this will pave the way for making this light fuel gas a sustainable energy source. Among electrochemical energy conversion advances, hydrogen energy is considered the most powerful candidate to alternate fossil energy due to its clean, renewable, and environmentally friendly properties and high energy density [2–4]. Despite the fact that in electrocatalytic water splitting the Pt cathode with near-zero overpotential is considered the most effective catalytic cathode, it has a high cost and platinum is a scarce resource [5]. With the purpose of seeking a low-cost and efficient catalytic cathode, many materials have been extensively explored by several authors.

Currently, many studies have been devoted to the use of hydrogen storage solids as active materials for application in fuel cells, and as a means of intermittency mitigation in energy supplies, with the aim of carbonic neutrality and renewable clean energy as urgent objectives. Activated carbons are ineffective in hydrogen storage systems because only a small fraction of pores in their pore-size distributions are small enough to interact strongly with hydrogen molecules at the gas phase. For small-sized systems, surface- or interface-related sites assume crucial importance and can change the overall solubility of hydrogen. Thus, for improving the kinetic characteristics of hydrogen storage in materials,

great attention has been paid to thermal desorption studies and calibration [6–8]. Thermal desorption spectrometry (TDS) assures a good accuracy in monitoring hydrogen absorbed in solid materials [9], and it is suitable for monitoring hydrogen evolution following the application of a thermal ramp, in contrast to the determination of static sorption isotherms. The use of a mass spectrometer allows evolved gas species to be identified, whereas the other methods are non-selective. The binding energy of adsorbed molecules varies with the nature of the adsorbate/surface materials, and desorption temperature gives information on the binding energy [10,11].

An additional goal consists of looking for low weight and high performance hydrogen active storage media made from carbon nanomaterial assemblies. Several carbon nanomaterial assembly-based electrodes are used in this work for comparing their relative performance. With this purpose in mind, the recent molecular-beam thermal desorption spectrometry (MB-TDS) is used in this work [12]. This technique is a variant of thermal desorption spectrometry which has been developed to detect the hydrogen release by the lowest amounts of solid samples, with several advantages [12–16].

2. Materials and Methods

A tuned desorption spectrum for hydrogen typically displays peaks caused by desorption with an origin on different adsorbed phases, and the total desorbed quantity of hydrogen is determined from the integral of the mass spectrometer signal, providing it can be adequately calibrated [12]:

$$n_T = \int_{t_0}^{t_1} n(t)dt \quad (1)$$

where n_T represents the number of moles of desorbed hydrogen and n(t) the molar hydrogen desorption rate as a function of time.

Within the range of temperatures used in this work (below 400 K) hydrogen desorption from chemisorbed sites in the material is not detected and so one can simplify the non-equilibrium kinetics of the global desorption process by the following three elementary steps:

(i) $(C–H)_{ads} \rightarrow H(lat)$
(ii) $H(lat) \rightarrow H(s)$
(iii) $H(s) + H(s) \rightarrow H_2(g)$ where H(s) are hydrogen atoms on the surface of the material grains or nano-regions of the material, H(lat) are hydrogen atoms inside the material lattice but outside the chemisorption centers, and $(C–H)_{ads}$ are the physisorbed hydrogen atoms on active sites. The second stage is diffusion-limited, and from the condition of maximum desorption at $T = T_m$, one gets:

$$\ln\left(\frac{T_m^2}{\beta}\right) \approx \frac{E_a^{dif}}{k_B T(T_m)} \quad (2)$$

where ${E_a}^{dif}$ is the diffusion activation energy, k_B the Boltzmann constant, and β the heating rate.

The activation energy of desorption E_d can then be determined from the linear dependence of $\ln(\beta/{T_m}^2)$ on $1/T_m$ and from these considerations, it is then possible to confirm or not, if desorption is a diffusion-controlled process [17,18].

Pumping out the heated oven (with the sample inside), and considering that desorption activation energy, E_d it is possible to show that desorption activation energy can be obtained from the experimental MB-TDS desorption curves making use of the equation [19]:

$$\ln\left(\frac{\beta}{T_m^2}\right) = -\frac{E_d}{RT_m} + \ln\frac{RB}{E_d} \quad (3)$$

where B stands for the Arrhenius pre-exponential factor, and R is the universal gas constant.

Molecular-beam thermal desorption mass spectrometry is applied to the determination of electrochemical hydrogen uptake and release by the samples. The MB-TDS apparatus has already been described elsewhere [12] and is merely schematically displayed in Figure 1, where a composite molecular beam of known intensity is produced from the degassing solid sample at a certain temperature inside the oven.

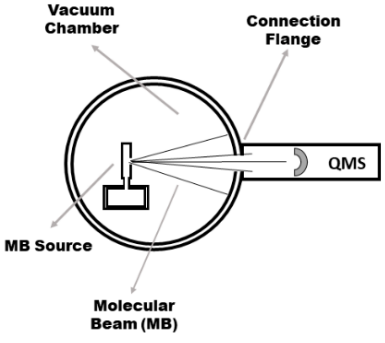

Figure 1. Top view of the molecular-beam thermal desorption spectrometry (MB-TDS) configuration.

By tuning the mass spectrometer to the hydrogen gas, one can monitor its evolution in time, thus measuring the amount of hydrogen desorbed from the sample. The effusion beam can be geometrically defined as well as its fraction detected by the quadrupole mass spectrometer (QMS) located in the forward direction (Figure 1).

Values of the order of 1 °C min^{-1} have typically been used for the heating rate of each sample. The hydrogen partial pressure background variation can be described by a temporal decay [12,13].

By subtracting the residual hydrogen gas background (measured without the beam) from the total amount of hydrogen impinging in the quadrupole spectrometer, one can compute the real amount of hydrogen coming from the sample [12,13]. The ratio of the hydrogen background partial pressure variations, for the situations of heating-on and heating-off, lead to the simple following expression [12]:

$$\frac{N_0 + N_b}{N_0} = 1 + \frac{A_b}{A_0} \quad (4)$$

N and A stand, respectively, for the number of hydrogen molecules and the area under the desorption curve, with the subscripts "0" and "b" assigned respectively to the situations "without the beam" and "with the beam".

Before introducing a sample in the oven of the MB-TDS apparatus, it needs to be submitted to hydrogen uptake, and this is done by electrochemical hydrogen charging. This procedure requires a previously experimental preparation of cathodes, which is summarized here for different carbon nanomaterials.

(i) Graphene

Graphene structures have received considerable interest due to their outstanding properties such as interconnected porous structures, enormous specific surface area, good mechanical stability, and flexibility to tailor their surface chemistry [20–22].

A 3D-graphene in the form of a pellet, possesses a monolithic structure with high electrical conductivity (148 S cm^{-1}), well-controlled mesopore size (~2 nm), and good electromechanical properties. Details about the synthesis and characterization of 3D graphene have been published by our group elsewhere [23–26]. In brief, 3D graphene pellet is synthesized by chemical vapor deposition (CVD), using nickel powder as a catalyst, and it can be further processed into a graphene paper by pressing. It possesses electrical conductivity of above 1100 S cm^{-1} and exhibits breaking stress of about 20 MPa.

Since Ni is catalytic, the etching with HCl was active for one hour, which is believed to be time enough to assure a complete depletion of Ni contamination. There was no determination of the Ni that remained.

The morphology of graphene with high surface roughness could contribute to a good adhesion with any substrate of practical interest due to the existence of van der Waals forces. Figure 2a displays a scanning electron microscopy (SEM) image of the 3D graphene pellet and Figure 2b shows Raman spectra of the same sample conducted at different spots.

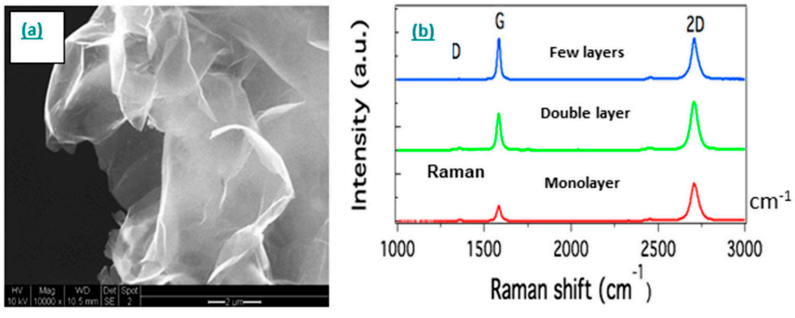

Figure 2. (**a**) Scanning electron microscope (SEM) of 3D graphene pellet; (**b**) Raman spectroscopy of 3D graphene pellet conducted at altered spots on the sample, revealing a different number of graphene layers within the probed flakes.

After etching the Ni catalyst with HCl acid, the graphene pellet obtained was transferred onto a Kapton (polyimide) film and dried at 40 °C. A good adhesion between graphene and Kapton substrate was created due to van der Waals forces and the unique morphology of the 3D graphene. The graphene pellet with the dimension 5 mm × 5 mm was connected to a silver wire using silver conductive epoxy, which was then coated with non-conductive epoxy. After drying overnight at room temperature, the working electrode was ready for use.

(ii) Single-walled carbon nanotube networks

Uniform thin films of single-walled carbon nanotube (SWCNT) networks of varying densities have been fabricated at room temperature by vacuum filtration. A dilute suspension of purified rice nanotubes in chloroform is sonicated, and then vacuum filtered through an alumina membrane (Whatman, Maidstone, UK, 20 nm pore size) in a short time (few seconds). As the solvent passes through the pores, the nanotubes are trapped on the surface of the filter, forming an interconnected mesh. Its density (nanotubes/area) can be selected by controlling the volume of the dilute suspension filtered through the membrane. The fast vacuum filtering process prevents tube flocculation, and then one proceeds with the transfer of the film to another surface by membrane dissolution. The film can be made free-standing over an aperture (25 mm^2) by making the transfer to a Teflon substrate with a hole, over which the film is laid before membrane dissolution in sodium hydroxide aqueous solution. Measurements of the sheet conductance have shown that it increases with the network density. This is expected since through percolation a significant number of both metallic and semiconducting nanotubes operate as electrical conducting pathways. For an SWNT (single-walled carbon nanotube) sheet made from 20 mL of a solution of carbon nanotubes in chloroform with the concentration of 0.2 mg L^{-1} the measured DC electrical conductance was about 7×10^{-6} S cm^{-2}. Finally, the free-standing film obtained is transferred on to a Kapton film and dried which is put in adhesion contact with it through the hole. Its atomic force microscopic topographical image is shown in Figure 3. The SWNTs network with the dimension 5 mm × 5 mm was connected to a silver wire using silver conductive epoxy, which was then coated with non-conductive epoxy. After drying at room temperature, the electrode was ready for use.

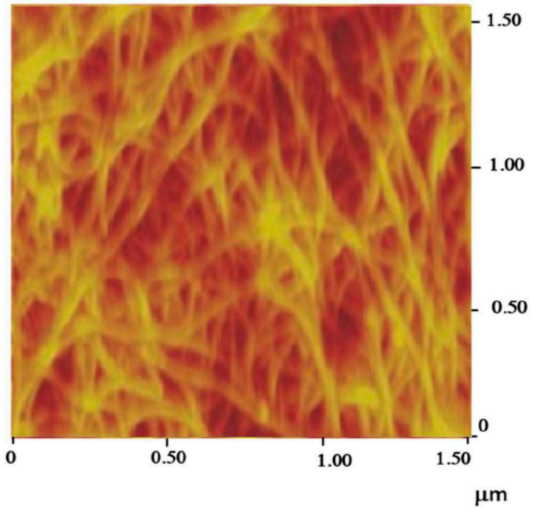

Figure 3. Atomic force microscopy (AFM) image of SWCNT network transferred to a film surface.

(iii) Multi-walled carbon nanotube networks

Vertically aligned multi-walled carbon nanotube (MWCNT) arrays were synthesized using CVD and were then removed from the catalyst substrate in a procedure described elsewhere [27] and transferred to a glass substrate. With a small roller of Teflon, the carbon nanotube (CNT) carpet is smashed against the substrate surface and converted into a free-standing film which is then submitted to the analogous previous procedures (i and ii) to build the electrode.

(iv) Carbon nanotube thread

MWNTs (multiple-walled carbon nanotubes) thread dry spinning starts with the synthesis of vertically aligned CNTs which have the ability to assemble themselves into films or ribbons, and subsequent threads [28]. Catalyst film thickness and CNT synthesis parameters have been studied [27]. The as-synthesized CNT arrays are completely detached from their substrates during synthesis and they are fully spinnable which allows monitoring the diameter of CNT threads [28]. Different twist angles from the same array width were obtained by varying the draw and rotational speed allowing a thread to be prepared by this method [29]. Figure 4 displays SEM images of the material.

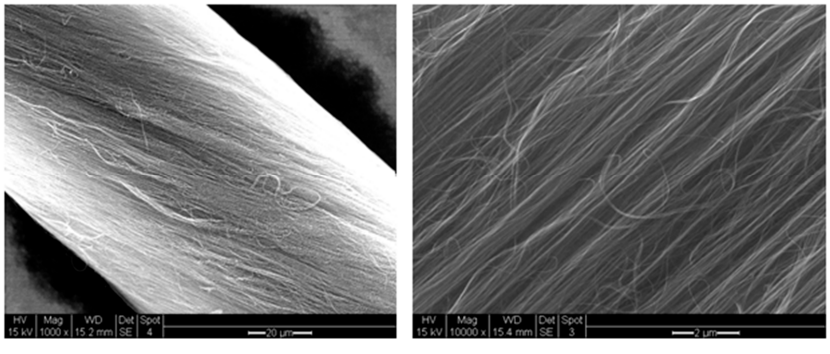

Figure 4. SEM images of carbon nanotube thread.

A CNT pristine thread with 35 μm diameter and 2 cm long was connected to a copper wire using silver conductive epoxy. After that, it was coated with a polystyrene solution (15 wt% in toluene) and air-dried at 50 °C. Following, the CNT thread was aspirated into a glass capillary and the end of the glass capillary was sealed with a hot glue gun. Last, the polystyrene-coated CNT thread electrode was cut off at the end with a sharp blade. In this way, only the end of the CNT thread was exposed.

Usually, electrochemical hydrogen charging and discharging curves are recorded (by galvanostatic or voltammetry techniques) in order to estimate the electrochemical hydrogen storage capacity [30]. In this work, the hydrogen uptake in the nanostructured carbon electrodes was undertaken in a galvanostatic way, and the release of hydrogen was measured with the MB-TDS technique.

During electro-reduction (i.e., the process of insertion into nanoporous carbon), hydrogen could be stored by cathodic decomposition of water in both NaOH and H_2SO_4 aqueous solutions. Applying a negative polarization to the carbon electrode, hydrated Na^+ and H_3O^+ cations are adsorbed, respectively, in the alkaline and acidic medium, forming the well-known electric double layer. Once the electrode potential becomes lower than the equilibrium redox potential, hydrogen in the zero-oxidation state is formed by the reduction of water in the case of alkaline solution (or of hydronium ions H_3O^+ in the acidic medium). In the next step, hydrogen is expected to be physically adsorbed onto the carbon surface giving rise to H_{ad} [31].

It is worth noting that typical impurities of NaOH and H_2SO_4 are catalytic, and so we used, respectively, NaOH reagent grade, ≥98%, pellets (anhydrous), and H_2SO_4 99.999%.

The total amount of hydrogen adsorbed, (i.e., storage capacity), depends essentially on the kinetics of hydrogen diffusion and incorporation into the nanopores. At low overvoltage, the diffusion of H_{ad} proceeds slower than the reduction step of water or H_3O^+, then H_{ad} participated in chemical (Tafel) or electrochemical (Heyrovsky) recombination reactions, which result in the evolution of di-hydrogen. This latter case takes place with an H_2SO_4 medium, and it has been shown that hydrogen is poorly adsorbed, easily giving rise to molecular hydrogen evolution. In contrast, with the NaOH electrolyte, due to the high value of polarization, carbon demonstrates a noticeable hydrogen capacity. Hence, the electro-reduction of water in the basic medium allows higher hydrogen pressure to be reached than in the conventional gas phase technique [31]. Hydrogen produced from electrolysis during charging of the cell partly entered the working electrode and the rest was released as gas. The operation is interrupted after a rapid generation of hydrogen gas bubbles is observed, suggesting that storage was complete [30].

Electrolysis can be used practically to charge the material. Electrochemical hydrogen charging and discharging curves are recorded (by galvanostatic or voltammetry techniques) in order to estimate the electrochemical hydrogen storage capacity. In this work, the hydrogen uptake in the nanostructured carbon electrodes was done in a galvanostatic way, and the release of hydrogen was measured with the MB-TDS technique. A pure platinum anode was used for charging (at room temperature and atmospheric pressure) the working cathodes (already mentioned) of the electrolytic cell, through one molar NaOH electrolyte solution. All the samples were submitted to an identical constant applied voltage of 1.0 V in one hour. This was done at a constant applied voltage only after a significant increase in the electrolyte resistance had occurred. The cell contained an aqueous electrolyte of NaOH at a concentration of 1 M, and an electric current of 133 mA was imposed for 60 min.

This galvanostatic procedure is common to the following four cathodes: graphene, single-walled and multi-walled carbon nanotube networks, and carbon nanotube thread. After the electrochemical charging, each sample was dried in a desiccator under a vacuum (Figure S1).

Regarding sample (iv), coaxial cylindrical stainless steel was used as the anode in a similar electrolyte solution and similar hydrogen electrochemical charging conditions.

The samples were weighed in a Kern ABT-101 analytical balance before and after the electrochemical hydrogen uptake. The relative weight increases were: 9% for the MWNT

thread; 8% for Pd; 6% for graphene; 4% for the SWNTs network and 2% for the MWNTs network. The differences in weight are in the order of a few units of milligrams.

Each of the hydrogenated samples was then submitted to the already described MB-TDS procedure, allowing interpretation of desorption spectra in a similar way to the well-known temperature programmed desorption spectroscopy [9,32–34]. By subtracting the residual hydrogen background pressure, measured without beam taken in similar experimental conditions, one can compute the total amount of hydrogen contained in the samples, from the area of the respective MB-TDS experimental curves (Figure 5) [34].

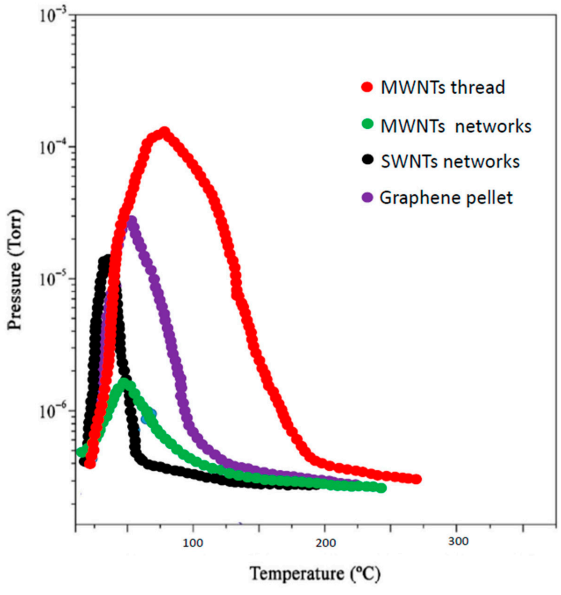

Figure 5. MB-TDS spectra were taken at a heating rate of 1 °C/min.

This way one can obtain the ratio E_d/R and from that by subtracting the corresponding background pressure, one can obtain the area A_b below them. This area is related to the number of hydrogen molecules N_b detected with the QMS, by the expression [34]

$$N_0 + N_b = (A_0 + A_b)\frac{N_A S}{RT} \quad (5)$$

where S is the pumping speed and N_A the Avogadro number.

To estimate the total amount of hydrogen desorbed from the samples, the number of hydrogen molecules still needs to be corrected with the geometrical fraction of the hydrogen beam effectively "seen" by the QMS detector and the ionization efficiency of this detector as well [34]. An efficiency of about 70% is expected, given the QMS catalog technical specifications [12]. Also, from the geometrical configuration, one can estimate a fraction of 20% of the beam that effectively impinges on the QMS detector. From the combination of these two attenuation effects, a reduction factor in the order of 10 in the molecular flux impinging the detector is expected [12]. The hydrogen masses detected can then be computed, and not surprisingly, they are only in agreement with the relative weight increased values (previously recorded in the experimental part), if they are multiplied by a factor of 10, which is exactly the experimental attenuation factor already mentioned. The total amount of hydrogen content for each of the samples could then be computed from the MB-TDS spectrum, which offers an alternative way to avoid misleading weight results in the case of minimal amounts of hydrogen uptake [34].

3. Results and Discussion

From the relative corrected area of the spectra given in Figure 5, it is found that they reasonably agree with the expected relative weight increases already mentioned in the experimental part:

MWNT thread = 9% → Graphene = 6% → SWNT network = 4% → MWNT network = 2%

The wt% of hydrogen absorbed in carbon nanostructures is likely to be proportional to their respective specific surface areas [35], and in fact, the above sequential order seems to be explained by this argument, as from all the carbonaceous samples, the carbon nanotube thread and the graphene pellet have the higher values of specific surface areas. This has been observed for materials with a surface area lower than 1000 m^2/g [35]. However, for adsorbents with high surface area, some theoretical studies point to a relevant influence of the pore size distribution [36].

These advanced carbon nanostructures are very promising for hydrogen storage technological applications since they are much lighter than alternative metals (as palladium) or metal hydrides in metal alloys.

Recording MB-TDS spectra with different scan rates (0.5 K min^{-1}, 1.0 K min^{-1} and 2.0 K min^{-1}), and fitting linear plots to the experimental points (β_i, T_{mi}), one could find the corresponding desorption energies [32–34]:

Graphene = 5.4 kJ/mol → MWNT network = 18.3 kJ/mol → SWNT network = 20.2 kJ/mol → MWNT thread = 22.1 kJ/mol

Figures 6 and 7, respectively, display, those spectra and corresponding plots, for the case of the MWNT thread. Carbon materials usually display a high cycle life of hydrogen uptake/release and are lighter and mostly environmentally friendly, in comparison with pure metals or metal hydrides. The electrochemical hydrogen storage capacity of carbon materials exceeding 1.5 wt% at ambient conditions allows them to be viewed as a potential anode material in replacement of some pure metals or metallic alloys [37].

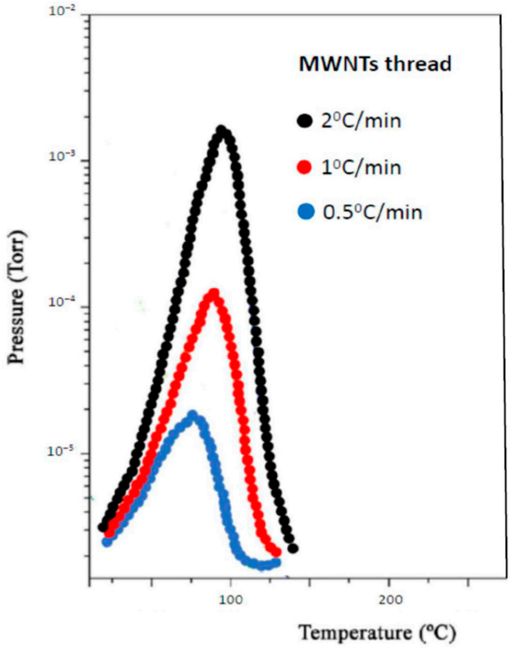

Figure 6. MB-TDS spectra of hydrogenated MWNT thread, taken at three different heating rates.

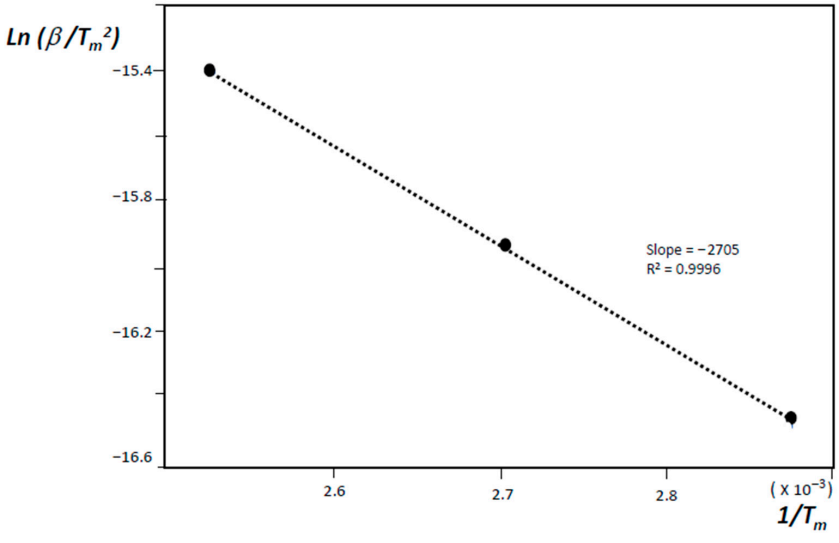

Figure 7. Fitting of a linear plot to the experimental points (β_i,T_{mi}) obtained for hydrogenated MWNT thread.

The hydrogen storage in CNTs is the result of the combined action of physisorption and chemisorption. The hydrogen storage capacity of carbon materials mainly depends upon surface area, which is affected by micropore size distribution that counts for the presence of narrow micropores. Based on theoretical studies, some authors have found a strong structural dependence on hydrogen adsorption in carbon-based materials (especially CNT), and defects affect their adsorption capacity.

Many researchers have carried out experimental research and theoretical analysis on hydrogen storage in carbon nanotubes (CNTs), but the results are very inconsistent [38]. Hydrogen electro-sorption on carbon materials is a complex process, involving the overlapping of hydrogen ad-atoms formation and storage. If carried out under the same electrochemical conditions, this combined process depends on the porous structure and surface chemistry of the sorbent material as well as its electrical properties. The highest efficiency is achieved if the carbon materials are very amorphous and have a hierarchical micro/mesopore structure [39]. One can assume that electrochemical charging consists of two steps: (1) basic charging, which proceeds with increased H_{ad} coverage of the outer surface of the porous material; and (2) a surcharge, consisting in continuous saturation of less accessible narrow micropores with hydrogen when H coverage of the outer surface is high enough [37].

The electrochemical charge-discharge mechanism in SWCNT paper electrodes is known to be controlled by a proton diffusion process, and somewhere in between a physical process (as in pure carbon nanotubes) and a chemical process (as in metal hydride electrodes). It consists of a charge transfer reaction (reduction/oxidation) and a diffusion step (diffusion) [40].

Electrochemical studies have also revealed that oriented mesoporous carbon shows better electrochemical storage of hydrogen compared to ordinary activated carbon [41]. For large diameter single-walled carbon nanotubes (SWCNTs), a hydrogen storage capacity of 4.2% weight (i.e., hydrogen to carbon atom ratio of 0.52), has been achieved (at room temperature and under the pressure of 10 MPa), and 3.3% by weight could be released at ambient pressure and room temperature, while the release of the residual stored hydrogen (0.9 wt%) required some heating of the sample [42]. The following experimentally measured hydrogen storage capacities of carbon nanotubes have been reported: SWCNT (8 wt%),

Li-doped MCWNT (20 wt%), Well-aligned MCWNT (3 wt%). The accuracy of the method used for the determination of hydrogen electrosorption ability is limited mainly by the accuracy of sample mass determination [43].

Temperature programmed desorption data for hydrogen absorbed in SWNTs using gas-phase loading revealed activated desorption energy of about 19.6 kJ mol^{-1} [44]. This value is close to that obtained in this work for the SWNT network which confirms the absorption performance of SWNT assemblies by two different techniques.

In the case of physical absorption, the desorption activation energy corresponds to the heat of adsorption, and such observed highly bound physisorbed di-hydrogen is consistent with adsorption within the SWNTs cavities, indicating that the inner parts of the tube become accessible after heating under vacuum [44]. The value of the activated desorption energy found for the SWNT network sample is very close to the value obtained by using hydrogenated SWNTs in the gas phase.

Since the hydrogen evolution reaction would have a large overpotential on the basal plane of graphene, the reaction most likely occurs either on edge functional groups or on metallic impurities, so it will be necessary to characterize the samples much more thoroughly, with this thought in mind. Also, as the hydrogen evolution reaction is facile on Pt it is dangerous to use a Pt anode because, during electrolysis, Pt dissolves and goes into solution, redepositing on the cathode and possibly enhancing the catalysis. In future works, it will be recommended to check the effect of using a non-catalytic anode material.

Hydrogen can be physisorbed in carbon nanotubes bundles on various sites such as external wall surface, grooves, and interstitial channels. Therefore, it can have a large energy density (as required for mobile applications). It is also known that by tuning the adsorption conditions hydrogen can be either chemisorbed or physisorbed on carbon nanotubes. The adsorption of atomic hydrogen is highly unfavorable on the basal plane of graphene and would require specific sites, probably metallic. However, in the MB-TDS experiments, our mass spectrometer is unable to distinguish between adsorbed molecular and atomic hydrogen. For that, a QMS with improved mass resolution will be needed.

4. Conclusions

Results reported here stand for the analytical determination of absorbed/adsorbed hydrogen using a specific type of thermal desorption spectroscopy in conjunction with mass spectrometry (MB-TDS). This technique is revealed to be a powerful procedure for monitoring, in real-time and in situ, the hydrogen release from different advanced carbon nano-electrocatalysts, and for a comparative quantitative analysis of this trace element among them (the amounts are below the detection limit of a microbalance).

The hydrogen storage in CNTs is the result of the combined action of physisorption and chemisorption. It has been demonstrated that the maximal degree of nanotube hydrogenation depends on the nanotube diameter, and for the diameter values around 2.0 nm, nanotube-hydrogen complexes with close to 100% hydrogenation exist and are stable at room temperature. This means that specific carbon nanotubes can have a hydrogen storage capacity of more than 7 wt% through the formation of reversible C–H bonds.

The results point to the use of inter-tube sites in carbon nanostructures for storing hydrogen by a physisorption mechanism. Temperatures of hydrogen desorption as high as about 350 K has been achieved, possibly due to the availability of 'sub-nanometer' sized spaces [45].

This study is one step further in comparing advanced carbon nanostructured electrodes for similar hydrogen uptake/desorption conditions and confirms the expectations about their enhanced hydrogen storage capacity.

The MWNT thread displays the largest desorption energy among them and possesses a set of suitable properties for making it an excellent candidate for electrocatalyst for hydrogen evolution.

The results of this investigation on the H_2-storage ability of various carbon-based nanomaterials indicate that MWNT thread material has the highest wt% of H_2 absorbed

as high as 9% compared to 6%, 4%, and 2% for graphene, SWNT network, and MWNT network, respectively. This confirms that the hydrogen storage capacity of carbon materials depends on the surface area. As a suggestion for further work to be pursued, it will be interesting to establish the relationship of the H_2 capacity against the surface areas as well as pore volumes of the corresponding materials. The availability of BET data on surface area and pore volumes for all the studied materials eventually will illustrate such correlation, albeit the N_2-adsorption-desorption isotherm data are not able to directly reflect the H_2 storage ability of the materials (N_2 isotherm can provide a positive trend for the capacity ability toward hydrogen molecules). Future studies on surface modification and composite structure are expected to be carried out, in the search to improve the electrocatalytic performance by overcoming the limitations of active sites, intrinsic catalytic activity, and inter-yard conductivity. In-depth research on these issues can provide a clue for improvement of the efficiency in electrocatalytic hydrogen evolution and a deep insight into the catalytic mechanism.

Supplementary Materials: The following are available online at https://www.mdpi.com/article/10.3390/nano11051079/s1, Figure S1: Galvanostatic charge of hydrogen in the four studied nanostructured carbon cathodes, in NaOH 1 M solution.

Author Contributions: Conceptualization, R.L.; methodology, R.L.; investigation, R.L.; resources, V.S. and N.A.; supervision, R.L. All authors have read and agreed to the published version of the manuscript.

Funding: This work is financed by national funds registered in the budget of FCT-Foundation for Science and Technology within the scope of the Research Unit CTS-Center for Technology and Systems, under the reference UIDB/00066/2020. FCT-MCTES Portugal through SFRH/BSAB/135131/2017 is also gratefully acknowledged.

Acknowledgments: Facilities used at University of Cincinnati are gratefully acknowledged.

Conflicts of Interest: The authors declare no conflict of interest.

References

1. Wang, Z.; Mi, B. Environmental Applications of 2D Molybdenum Disulfide (MoS_2) Nanosheets. *Environ. Sci. Technol.* **2017**, *51*, 8229–8244. [CrossRef] [PubMed]
2. Gu, M.; Choi, J.; Lee, T.; Park, M.; Shin, I.-S.; Hong, J.; Lee, H.-W.; Kim, B.-S. Diffusion controlled multilayer electrocatalysts via graphene oxide nanosheets of varying sizes. *Nanoscale* **2018**, *10*, 16159–16168. [CrossRef]
3. Lin, L.; Zhou, W.; Gao, R.; Yao, S.; Zhang, X.; Xu, W.; Zheng, S.; Jiang, Z.; Yu, Q.; Li, Y.-W.; et al. Low-temperature hydrogen production from water and methanol using Pt/α-MoC catalysts. *Nat. Cell Biol.* **2017**, *544*, 80–83. [CrossRef]
4. Wang, J.; Cui, W.; Liu, Q.; Xing, Z.; Asiri, A.M.; Sun, X. Recent Progress in Cobalt-Based Heterogeneous Catalysts for Electrochemical Water Splitting. *Adv. Mater.* **2016**, *28*, 215–230. [CrossRef]
5. Eftekhari, A. Electrocatalysts for hydrogen evolution reaction. *Int. J. Hydrogen Energy* **2017**, *42*, 11053–11077. [CrossRef]
6. Thornburg, N.A.; Abdelrehim, I.M.; Land, N.P. Kinetics of Propene Desorption from Pd(111) Studied by Thermal Desorption Spectroscopy and Laser-Induced Thermal Desorption with Fourier Transform Mass Spectrometry. *J. Phys. Chem. B* **1999**, *103*, 8894–8898. [CrossRef]
7. Zaluska, A.; Zaluski, L.; Ström–Olsen, J. Nanocrystalline magnesium for hydrogen storage. *J. Alloys Compd.* **1999**, *288*, 217–225. [CrossRef]
8. Castro, F.; Meyer, G.; Zampieri, G. Effects of sulfur poisoning on hydrogen desorption from palladium. *J. Alloys Compd.* **2002**, *330–332*, 612–616. [CrossRef]
9. Redhead, P. Thermal desorption of gases. *Vacuum* **1962**, *12*, 203–211. [CrossRef]
10. Huot, J.; Liang, G.; Schulz, R. Mechanically alloyed metal hydride systems. *Appl. Phys. A* **2001**, *72*, 187–195. [CrossRef]
11. Ballenweg, S.; Gleiter, R.; Krätschmer, W. Hydrogenation of buckminsterfullerene C60 via Hydrozirconation: A new way to organofullerenes. *Tetrahedron Lett.* **1993**, *34*, 3737–3740. [CrossRef]
12. Lobo, R.F.M.; Berardo, F.M.V.; Ribeiro, J.H.F. Molecular beam-thermal hydrogen desorption from palladium. *Rev. Sci. Instrum.* **2010**, *81*, 43103. [CrossRef]
13. Lobo, R.F.M.; Santos, D.M.F.; Sequeira, C.A.C.; Ribeiro, J.H.F. Molecular Beam-Thermal Desorption Spectrometry (MB-TDS) Monitoring of Hydrogen Desorbed from Storage Fuel Cell Anodes. *Materials* **2012**, *5*, 248–257. [CrossRef]
14. Merzlikin, S.V.; Borodin, S.; Vogel, D.; Rohwerder, M. Ultra high vacuum high precision low background setup with temperature control for thermal desorption mass spectroscopy (TDA-MS) of hydrogen in metals. *Talanta* **2015**, *136*, 108–113. [CrossRef]

15. Hanna, T.; Hiramatsu, H.; Sakaguchi, I.; Hosono, H. Highly hydrogen-sensitive thermal desorption spectroscopy system for quantitative analysis of low hydrogen concentration ($\sim 1 \times 10^{16}$ atoms/cm^3) in thin-film samples. *Rev. Sci. Instrum.* **2017**, *88*, 53103. [CrossRef]
16. Miyase, T.; Watanabe, K.; Sakaguchi, I.; Ohashi, N.; Domen, K.; Nomura, K.; Hiramatsu, H.; Kumomi, H.; Hosono, H.; Kamiya, T. Roles of Hydrogen in Amorphous Oxide Semiconductor In-Ga-Zn-O: Comparison of Conventional and Ultra-High-Vacuum Sputtering. *ECS J. Solid State Sci. Technol.* **2014**, *3*, Q3085–Q3090. [CrossRef]
17. Woodruff, D.P. *Modern Techniques of Surface Science*; Cambridge University Press (CUP): Cambridge, UK, 1994. [CrossRef]
18. Yates, J. *Solid State Physics: Methods of Experimental Physics*; Park, R., Lagally, M., Eds.; Academic Press: New York, NY, USA, 1985; Volume 22, ISBN-13: 978-0124759640.
19. Beeby, J.L. The theory of desorption. *Crit. Rev. Solid State Mater. Sci.* **1978**, *7*, 153–166. [CrossRef]
20. Chen, Z.; Ren, W.; Gao, L.; Liu, B.; Pei, S.; Cheng, H.-M. Three-dimensional flexible and conductive interconnected graphene networks grown by chemical vapour deposition. *Nat. Mater.* **2011**, *10*, 424–428. [CrossRef]
21. Chen, B.; Ma, Q.; Tan, C.; Lim, T.-T.; Huang, L.; Zhang, H. Carbon-Based Sorbents with Three-Dimensional Architectures for Water Remediation. *Small* **2015**, *11*, 3319–3336. [CrossRef]
22. Kabiri, S.; Tran, D.N.H.; Cole, M.A.; Losic, D. Functionalized three-dimensional (3D) graphene composite for high efficiency removal of mercury. *Environ. Sci. Water Res. Technol.* **2016**, *2*, 390–402. [CrossRef]
23. Hsieh, Y.-Y.; Zhang, L.; DeArmond, D.; Kanakaraj, S.N.; Adusei, P.K.; Alvarez, N.T.; Fang, Y.; Daum, J.; Shanov, V. Integrated graphene-sulfur cathode and separator with plasma enhancement for Li-S batteries. *Carbon* **2018**, *139*, 1093–1103. [CrossRef]
24. Zhang, L.; DeArmond, D.; Alvarez, N.T.; Malik, R.; Oslin, N.; McConnell, C.; Adusei, P.K.; Hsieh, Y.-Y.; Shanov, V. Flexible Micro-Supercapacitor Based on Graphene with 3D Structure. *Small* **2017**, *13*. [CrossRef]
25. Zhang, L.; DeArmond, D.; Alvarez, N.T.; Zhao, D.; Wang, T.; Hou, G.; Malik, R.; Heineman, W.R.; Shanov, V. Beyond graphene foam, a new form of three-dimensional graphene for supercapacitor electrodes. *J. Mater. Chem. A* **2015**, *4*, 1876–1886. [CrossRef]
26. Zhang, L.; Alvarez, N.T.; Zhang, M.; Haase, M.; Malik, R.; Mast, D.; Shanov, V. Preparation and characterization of graphene paper for electromagnetic interference shielding. *Carbon* **2015**, *82*, 353–359. [CrossRef]
27. Alvarez, N.T.; Miller, P.; Haase, M.; Kienzle, N.; Zhang, L.; Schulz, M.J.; Shanov, V. Carbon nanotube assembly at near-industrial natural-fiber spinning rates. *Carbon* **2015**, *86*, 350–357. [CrossRef]
28. Alvarez, N.T.; Miller, P.; Haase, M.R.; Lobo, R.; Malik, R.; Shanov, V. Tailoring physical properties of carbon nanotube threads during assembly. *Carbon* **2019**, *144*, 55–62. [CrossRef]
29. Jayasinghe, C.; Chakrabarti, S.; Schulz, M.J.; Shanov, V. Spinning yarn from long carbon nanotube arrays. *J. Mater. Res.* **2011**, *26*, 645–651. [CrossRef]
30. Oberoi, A.S.; Nijhawan, P.; Singh, P. A Novel Electrochemical Hydrogen Storage-Based Proton Battery for Renewable Energy Storage. *Energies* **2018**, *12*, 82. [CrossRef]
31. Jurewicz, K.; Frackowiak, E.; Béguin, F. Towards the mechanism of electrochemical hydrogen storage in nanostructured carbon materials. *Appl. Phys. A* **2004**, *78*, 981–987. [CrossRef]
32. King, D.A. Thermal desorption from metal surfaces: A review. *Surf. Sci.* **1975**, *47*, 384–402. [CrossRef]
33. O'Connor, D.; Sexton, A.; Smart, R. *Surface Analysis Methods in Materials Science*; Springer Science & Business Media: Berlin/Heidelberg, Germany, 2013; ISBN 978-3-662-02767.
34. Lobo, R.; Berardo, F.; Ribeiro, J. In-situ monitoring of lowermost amounts of hydrogen desorbed from materials. *Int. J. Hydrogen Energy* **2010**, *35*, 11405–11411. [CrossRef]
35. Schlapbach, L.; Züttel, A. Hydrogen-storage materials for mobile applications. *Nat. Cell Biol.* **2001**, *414*, 353–358. [CrossRef] [PubMed]
36. Kowalczyk, P.; Hołyst, R.; Terrones, M.; Terrones, H. Hydrogen storage in nanoporous carbon materials: Myth and facts. *Phys. Chem. Chem. Phys.* **2007**, *9*, 1786–1792. [CrossRef] [PubMed]
37. Jurewicz, K. Influence of charging parameters on the effectiveness of electrochemical hydrogen storage in activated carbon. *Int. J. Hydrogen Energy* **2009**, *34*, 9431–9435. [CrossRef]
38. Mohan, M.; Sharma, V.K.; Kumar, E.A.; Gayathri, V. Hydrogen storage in carbon materials—A review. *Energy Storage* **2019**, *1*, e35. [CrossRef]
39. Babel, K.; Janasiak, D.; Jurewicz, K. Electrochemical hydrogen storage in activated carbons with different pore structures derived from certain lignocellulose materials. *Carbon* **2012**, *50*, 5017–5026. [CrossRef]
40. Lyu, J.; Kudiiarov, V.; Lider, A. An Overview of the Recent Progress in Modifications of Carbon Nanotubes for Hydrogen Adsorption. *Nanomaterials* **2020**, *10*, 255. [CrossRef]
41. Guo, Z.; Ng, S.H.; Wang, J.; Huang, Z.; Liu, H.K.; Too, C.O.; Wallace, G.G. Electrochemical Hydrogen Storage in Single-Walled Carbon Nanotube Paper. *J. Nanosci. Nanotechnol.* **2006**, *6*, 713–718. [CrossRef]
42. Liu, C.; Fan, Y.Y.; Liu, M.; Cong, H.T.; Cheng, H.M.; Dresselhaus, M.S. Hydrogen Storage in Single-Walled Carbon Nanotubes at Room Temperature. *Science* **1999**, *286*, 1127–1129. [CrossRef]
43. Liu, D.; Zeng, C.; Tang, H.; Zheng, D.; Li, R.; Qu, D.; Xie, Z.; Lei, J.; Xiao, L.; Qu, D. Electrochemical Hydrogen Storage in a Highly Ordered Mesoporous Carbon. *Front. Energy Res.* **2014**, *2*, 1–6. [CrossRef]

44. Dillon, A.; Jones, K.; Bekkedahl, T.; Klangt, C.; Bethunet, D.; Heben, M. Storage of hydrogen in single-walled carbon nano-tubes. *Nature* **1997**, *386127*, 377–378. [CrossRef]
45. Shiraishi, M.; Takenobu, T.; Yamada, A.; Ata, M.; Kataura, H. Hydrogen storage in single-walled carbon nanotube bundles and peapods. *Chem. Phys. Lett.* **2002**, *358*, 213–218. [CrossRef]

nanomaterials

MDPI

Article

Hydrogen Uptake and Release in Carbon Nanotube Electrocatalysts

Rui Lobo [1,2,*], Jorge Ribeiro [1] and Filipe Inok [1]

[1] Laboratory of Nanophysics/Nanotechnology and Energy (N2E), Center of Technology and Systems (CTS-UNINOVA), Universidade Nova de Lisboa, 2829–516 Caparica, Portugal; jhfribeiro71@gmail.com (J.R.); afbi@campus.fct.unl.pt (F.I.)

[2] Department of Physics, Nova School of Science & Technology, Nova University of Lisbon, 2829–516 Caparica, Portugal

* Correspondence: rfl@fct.unl.pt; Tel.: +351-934463400

Abstract: The recent technique of molecular beam-thermal desorption spectrometry was used here for monitoring hydrogen uptake and release from carbon nanotube networks, after electrochemical hydrogen uptake. This way, an accurate determination of the hydrogen mass absorbed in electrodes made from those assemblies can be achieved by significantly improving the signal-to-noise ratio. The hydrogen desorption mass spectra account for the enhanced surface capability for hydrogen adsorption in the electrodes and enable a comparison with the performance of a palladium electrode in similar conditions. A comparative study involving different carbon nanotube electrodes, in similar hydrogen uptake/desorption conditions, clearly confirmed the expectations about their enhanced hydrogen storage capacity and points to the great potential of carbon nanotube assemblies in replacing the heavier metal alloys as electrocatalysts.

Keywords: carbon nanotube networks; electrocatalysis; desorption spectrometry; hydrogen storage

Citation: Lobo, R.; Ribeiro, J.; Inok, F. Hydrogen Uptake and Release in Carbon Nanotube Electrocatalysts. *Nanomaterials* **2021**, *11*, 975. https://doi.org/10.3390/nano11040975

Academic Editor: Domenica Tonelli

Received: 5 March 2021
Accepted: 7 April 2021
Published: 10 April 2021

1. Introduction

Hydrogen technology is expected to boost the efficiency of natural resources management, with fuel cells as one of the most promising technologies to reduce the emissions of greenhouse gases. Looking for lighter and cheaper electrodes and safer hydrogen storage media are relevant requirements to allow a widespread use of hydrogen as fuel, which is a recognized and promising sustainable energy source. Amongst the various problems that exist in the successful materialization of a hydrogen fuel-based economy, the formulation of a safe, economical, and efficient hydrogen storage method poses a relevant challenge. Keeping hydrogen within solid media assures high safety operation conditions and has several other advantages compared with pressurized or liquified techniques of transportation. To date, many studies have been conducted on the use of hydrogen storage solids as active materials for use in fuel cells and as a means of periodically mitigating energy supplies to achieve the urgent goals of carbon neutrality and clean renewable energy. An optimum hydrogen storage sponge material must display high hydrogen capacity per unit mass and unit volume (determining the amount of available energy), low dissociation temperature, low heat of formation (minimizing the energy necessary for hydrogen release), low heat dissipation during hydrogen uptake, reversibility, fast kinetics, high stability, material cost, and weightlessness. Carbon nanotubes appear to meet most of these criteria, and in this experimental work, they were studied alongside palladium, which is a proven reference material due to its superior hydrogen storage performance at room temperature and pressure conditions.

One desire to pursue is improving the kinetic properties of the hydrogen storage of materials; this way, special focus is given to studies on thermal desorption as well as

calibration [1–3]. Appropriate experimental techniques to study the basic physical processes involved in desorption are crucial. Of these, TDS (thermal desorption spectrometry) ensures good accuracy in monitoring hydrogen uptake in solids. They have high sensitivity and selectivity methods in studying the gas desorption of materials [4]. They form a sufficient means to monitor the evolution of hydrogen after the use of a heat ramp, in contrast with the methods of obtaining static sorption isotherms.

The binding energy of the molecules to be absorbed varies depending on the nature of the adsorbate/surface materials, and the desorption temperature provides information on that energy [5,6]. A relevant improvement when performed by QMS (quadrupole mass spectrometry) is the small sizes and weights of the samples that one intends to use. Additionally, choosing materials with high specific surfaces (which readily absorb different gases), conventional gravimetric methods can produce misleading measurements, and therefore the use of mass spectrometry ensures greater selectivity of identifiable evolving gas species.

An additional goal consists of looking for low-weight and high-performance hydrogen active storage media made from carbon nanomaterial assemblies. With this purpose in mind, different carbon nanomaterial assemblies-based electrodes were used in this work to compare their relative performance with a palladium electrode (as a typical hydrogen storage reference), in molecular-beam thermal desorption spectrometry (MB-TDS) [7]. As a variant of thermal desorption spectrometry, MB-TDS has been developed to detect the hydrogen release by lowermost amounts of solid samples [7,8]. It can be used successfully to measure amounts of hydrogen below the microbalance detection limit. Furthermore, it has several advantages over the conventional TDS method: real-time and in situ detection of trace hydrogen without prior calibration with a chemical standard [7,8] and the use of more laborious UHV (ultra-high-vacuum) techniques [9–11].

Amongst all of the emerging materials for solid-state hydrogen storage, nanostructure carbon materials (especially carbon nanotubes) have been receiving special attention. Single-wall carbon nanotubes can be assumed to form by rolling a single graphene sheet and due to several unique properties, they are envisaged as a very good medium for solid-state hydrogen storage. They are inert to surface contaminants and therefore less severe activation conditions are required. Additionally, in single-walled carbon nanotubes, all carbon atoms are exposed to the surface, which makes them the material with the highest surface-to-bulk atom ratio and therefore highly surface active. Furthermore, the densities of carbon nanotubes are considerably lower than that of metals, intermetallic-alloys and metal-organic frameworks. These nanomaterials are also known to possess large amounts of void spaces in the form of pores, which can accommodate large quantities of hydrogen.

The hydrogen storage in CNTs (carbon nanotubes) is the result of the combined action of physisorption and chemisorption. It has been demonstrated that the maximal degree of nanotube hydrogenation depends on the nanotube diameter, and for the diameter values around 2.0 nm nanotube-hydrogen complexes with close to 100% hydrogenation exist and are stable at room temperature. This means that specific carbon nanotubes can have a hydrogen storage capacity of more than 7 wt% through the formation of reversible C–H bonds.

The experiments on hydrogen adsorption in CNTs can, in general, be divided into two categories, depending on the method of storage: gas-phase hydrogen storage and electrochemical hydrogen storage. In gas-phase hydrogen storage techniques, a macroscopic sample of nanotubes is exposed to pure hydrogen gas under various temperature and equilibrium pressure conditions. The amount of hydrogen adsorbed by nanotubes is then measured gravimetrically using a microbalance. A more popular method of determining the amount of stored hydrogen is by volumetrically using Sieverts type volumetric apparatus. The latter technique involves the exposure of carbon nanotubes to hydrogen gas in a known volume and determining the storage capacity from the change in the free volume of the system upon exposure. With smaller quantities of sample, the gravimetric storage capacities can also be determined using temperature-programmed desorption or

thermogravimetric analysis. The second method of storing hydrogen in carbon nanotubes is electrochemical. To do this, the electrochemical cell is constructed with carbon nanotubes (CNTs) as the working electrode, Pt as the counter electrode, and an appropriate electrolyte. In such a system, hydrogen is stored in the CNT electrode by the reduction of water at a suitable potential. A storage equivalent of a discharge capacity of 110 mAh/g can be obtained when hydrogen is stored electrochemically. Though pristine-carbon nanotubes exhibit remarkable hydrogen storage capacity at cryogenic temperatures, their storage capacity diminishes to less than 1.0 wt% at room temperature.

Electrochemical hydrogen storage compared to other methods of hydrogen storage is very promising since it can be conducted at low temperature and pressure and with a high degree of reversibility (available hydrogen stored this way in materials can build supercapacitors with very high specific capacitance: up to 4×10^3 F g^{-1}).

Porous materials such as carbon materials, zeolites, and metal-organic frameworks, which physically adsorb H_2 molecules on the walls of the micropores, are one of the representative families of hydrogen-storage materials. Due to the weak interaction between hydrogen and the host materials, such porous materials can store sufficient amounts of hydrogen mostly at low temperatures and/or under high pressure. Another family comprises materials that chemically absorb H atoms internally, forming chemical bonds such as metal-hydrides.

Understanding the principal steps involved in H adsorption on the metal surface, followed by its interfacial transfer into the metal bulk, is of significance in metal-hydride science. Basic aspects of hydrogen physisorption and chemisorption under low-pressure gas-phase conditions, the adsorption sites of the physisorbed H_2 and the chemisorbed H as well as surface-chemical and surface-electronic state of chemisorbed H are fairly well understood. In the case of the H_2 molecule approaching the metallic surface at higher temperatures than those characteristics of physisorption, a distinct interaction pattern sets in. This results in strong (chemical) interactions between the metal surface and the H_2 molecule. The chemical interactions with the surface lead to dissociation of the H molecule into atomic H and practically instantaneous formation of a surface bond with the substrate:

$$H_2 \rightarrow 2\,H^*$$

$$2\,H^* + 2\,M \rightarrow 2\,M - H$$

The Pd–H system is one of the best-known metal–hydrogen systems. Palladium has a simple face-centered cubic (fcc) structure and can reversibly absorb and desorb hydrogen at ambient conditions. The Pd–H system has been extensively studied as a prototypical hydrogen-storage system. When Pd is exposed to hydrogen gas, H_2 molecules dissociate into atomic H on the surface of Pd; then the H atoms diffuse into bulk and occupy the interstitial sites of the (fcc) Pd lattice. The Pd–H system is known to have two distinct phases at ambient conditions, depending on the temperature and the hydrogen gas pressure. The hydrogen-absorption process of bulk Pd is divided mainly into three steps. The first step is the dissociation of hydrogen molecules into atoms on the surface of Pd (1→2). The second step is the penetration of the dissociated H atoms into the subsurface (2→3). The third step is a diffusion of H atoms into sites in the Pd lattice to form the hydride (Pd–H) (3→4). The effect of the dissociation process of hydrogen molecules into atoms on the Pd surface is negligibly small at 300 K (1→2). Therefore, the diffusion of the atoms from the surface to the subsurface (2→3) is considered to be the rate-limiting step for the H-absorption speed.

2. Materials and Methods

In TDS, the temperature of the sample surface is usually controlled linearly (constant heating rate), and when working at a high enough vacuum pumping speed, the desorption rate from the sample is proportional to the pressure. Furthermore, during desorption, the

determination of various adsorption and desorption parameters is based on the analysis of the hydrogen partial pressure–temperature curves (desorption spectra).

For desorption kinetics of the first order, the rate of desorption (r_d) of hydrogen molecules from an adsorbent surface, is given by:

$$r_d = -\frac{d\theta}{dt} = k_d\theta = v\theta exp\left(-\frac{E_d}{k_B T}\right) \quad (1)$$

where θ is the adsorbate coverage; k_d is desorption rate constant; v is the pre-exponential frequency factor (typically of the order of vibrational frequency in the range 10^{12}–10^{13} s^{-1}); E_d is the activation energy of desorption; and k_B the Boltzmann constant.

A desorption spectrum that represents desorption rate versus temperature typically displays peaks corresponding to desorption of different adsorbed phases. The physisorbed phases usually give rise to peaks generally below 400 K, while chemisorbed ones desorb at higher temperatures. Therefore, a TDS spectrum delivers a quick overview at which temperature the desorption takes place and displays peak(s) centered at value(s) of temperature, T_m, where $d^2N/dt^2 = 0$; with N representing here the number of hydrogen molecules. Given that $(dN/dt) = (dN/dT)\ \beta$, where β is the heating rate, then for desorption kinetics of first order, one gets for $T = T_m$:

$$\frac{E_d}{k_B T_m^2} = \frac{v}{\beta} exp\left(-\frac{E_d}{k_B T_m}\right) \quad (2)$$

This allows determining E_d from a semi-log linear plot, since β and T_m are the measurable parameters. Physical adsorption is a non-activated process, and so $E_d = E_b$, where E_b is the binding energy of the adsorbate to the surface. The constancy of the frequency factor can be assumed only for small desorbing molecules (as hydrogen).

The number of desorbed hydrogen moles, n_T, can be determined from the integral of the mass spectrometer signal, providing it can be adequately calibrated [7]:

$$n_T = \int_{t_0}^{t_1} n(t)dt \quad (3)$$

where $n(t)$ represents the molar hydrogen desorption rate as a function of time.

With the range of temperatures used in this work (below 400 K), hydrogen desorption from chemisorbed sites is not detected and so one can simplify the non-equilibrium kinetics of the global desorption process by the following three elementary steps:

(i) $(C–H)_{ads} \rightarrow H(lat)$
(ii) $H(lat) \rightarrow H(s)$
(iii) $H(s) + H(s) \rightarrow H_2(g)$

where H(s) stands for hydrogen atoms on the surface of the material nano-regions; H(lat) are hydrogen atoms inside the material lattice (but outside the chemisorption centers); and $(C–H)_{ads}$ are the physisorbed hydrogen atoms on active sites. The second step is limited by diffusion, which means that it is the step that determines the rate of the entire process.

In first-order kinetics, the diffusion-controlled desorption rate is given by:

$$r_d(t) = -\frac{dN(t)}{dt} = k_d(T(t))N(t) = k_d^0 exp\left(-\frac{E_a^{dif}}{k_B T(t)}\right)N(t) \quad (4)$$

where $N(t)$ stands for the average amount of the adsorbate in diffusion; ${E_a}^{dif}$ is the diffusion activation energy; and ${k_d}^0$ is related with the diffusivity pre-exponential factor D_0 by:

$$k_d^0 = \frac{1}{\tau_0} \approx \frac{D_0}{l^2} \quad (5)$$

Here, l and τ_0 represent, respectively, the diffusion characteristic length and the relaxation time for hydrogen removal. It can be also shown that:

$$l \approx \frac{\Delta T \, D_0(T_{max})}{\beta} \tag{6}$$

where ΔT stands for the full width at half maximum of the TDS peak.

From the condition of maximum desorption at $T = T_m$ (i.e., $\partial r_d / \partial T = 0$,) one gets:

$$\frac{T_m^2}{\beta} = \frac{E_a^{dif}}{k_B T(T_m)} \tag{7}$$

This equation shows a similarity with the equation for $k_d[T(t)]$, and from these considerations, it is possible to graphically confirm if desorption is a diffusion-controlled process or not [12–14]. The activation energy of desorption E_d can be obtained from the linear dependence of $ln({T_m}^2/\beta)$ versus $1/T_m$.

Quantitative determination of TDS requires an ulterior signal calibration measurement of hydrogen, which normally involves measuring the desorption spectrum of a reference sample (with known hydrogen content), which must maintain chemical stability, be neither hygroscopic nor vaporizable, over a temperature range (e.g., TiH_2). An error of $\pm 5\%$ in the weight of desorbed hydrogen between one and six mg in TiH_2 was estimated [13].

Molecular beam thermal desorption mass spectrometry (MB-TDS) was used here to determine the electrochemical capture and release of the hydrogen in the samples, and the apparatus has already been described elsewhere [7] (shown only schematically in Figure 1). A composite molecular jet of known intensity is produced through a well-defined geometric hole, with the origin in the solid sample from which degassing takes place at a certain oven temperature.

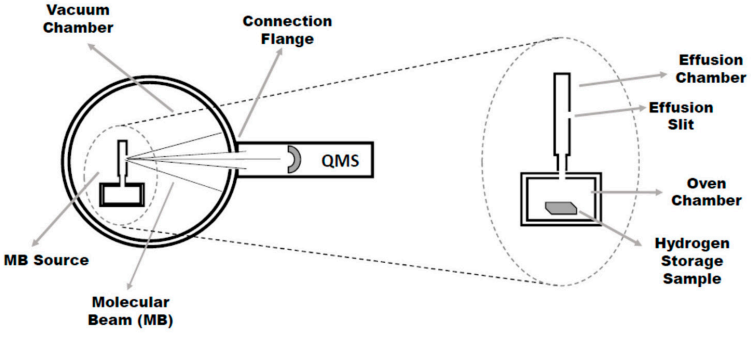

Figure 1. Molecular Beam-Thermal Desorption Spectrometry (MB-TDS)configuration (top view).

The recording of the hydrogen partial pressures with the quadrupole mass spectrometer (QMS) tuned to the hydrogen gas as a function of temperature and time allows for the amount of hydrogen desorbed to be measured. The scanning of temperatures is assured by a programmable-controlled heated system. Collisions between the molecules within the beam and those of the residual gas are prevented due to the combination of low pressure (high-vacuum conditions) with the low density of the beam. Due to these operation conditions, it is possible to define exactly the geometry of the effusion beam as well as the fraction of it detected by the QMS (which stays in the forward direction).

Normally, the source is maintained at 20 °C above the temperature of the sample oven (to avoid clogging of the crack) and PID temperature controllers allow the use of different heating rates; typically values of the order of 1 °C min^{-1} are used. The background change of the partial pressure of hydrogen can be described by a time decay [7,8].

By pumping the heated furnace (with the sample inside), the desorption rate of hydrogen, dX/dt, can be expressed as a function of temperature T [15,16]:

$$\frac{dX}{dt} = B(1 - X) \exp\left(-\frac{E_d}{RT}\right) \tag{8}$$

and therefore

$$\frac{E_d}{R} = \frac{v}{C\beta} \exp\left(-\frac{E_d}{RT_m}\right) \tag{9}$$

Defining X by the ratio of the amount of hydrogen released from the solid sample and the total hydrogen intake, then B is the Arrhenius pre-exponential factor, R the universal gas constant, and C the initial hydrogen concentration. Assuming this, one can obtain the desorption activation energy, making use of the recorded MB-TDS desorption curves, through the equation:

$$\ln \frac{T_m^2}{\beta} = \frac{E_d}{RT_m} - \ln \frac{RB}{E_d} \tag{10}$$

In contrast to the conventional TDS technique, where it is not possible to discriminate the hydrogen contribution coming out of the source inner walls, using our MB-TDS apparatus, one can indeed quantify such degassing amount by comparing (at a rate of $1/60$ K s^{-1}) and in the absence of a sample, the normalized pressure hydrogen background decay behaviors in two different situations: heating-on and heating-off. This reflects the very high sensitivity of the MB-TDS technique [7,8], which avoids misleading results due to background variations in the partial pressure of the hydrogen residue. One can then subtract the residual hydrogen gas background (recorded without jet) from the total hydrogen impinged on the QMS, and so the actual amount of hydrogen in the sample can be calculated [7]:

$$\frac{N_0 + N_b}{N_0} = 1 + \frac{A_b}{A_0} \tag{11}$$

Here, N and A stand respectively for the number of hydrogen molecules and the area under the desorption curve, with the subscripts "0" and "b" assigned, respectively, to the situations "beam-off" and "beam-on". An improvement of the order of 20% in the signal-to-noise ratio for the trace hydrogen can be estimated through expression (11) because the role of the operating condition of the real molecular beam is being played by the "heating-on" curve.

Before introducing each of the samples in the oven of the MB-TDS apparatus, they need to be submitted to hydrogen uptake, and this was done by electrochemical hydrogen charging. This procedure requires a previous experimental preparation of cathodes, which is summarized here for single-walled carbon nanotube (SWNT) networks.

3. Results and Discussion

Uniform thin films of SWNT networks of varying densities were fabricated at room temperature by vacuum filtration. A dilute suspension of purified Rice nanotubes in chloroform is sonicated and then vacuum filtered through an alumina membrane (Whatman, Sigma-Aldrich, Darmstadt, Germany) 20 nm pore size) in a short time (few s). As the solvent passes through the pores, the nanotubes are trapped on the surface of the filter, forming an interconnected mesh. The film can be made free-standing over an aperture (25 mm^2) by making the transfer to a Teflon substrate with a hole, over which the film is laid before membrane dissolution in sodium hydroxide aqueous solution. The obtained free-standing film is transferred onto a Kapton film and dried, which is put in adhesion contact with it through the hole. Its atomic force microscopic topographical image is shown in Figure 2. The SWNT network with the dimension 5 mm $\times$ 5 mm was connected to a silver wire using silver conductive epoxy, which was then coated with non-conductive epoxy. After drying at room temperature, the electrode was ready for use.

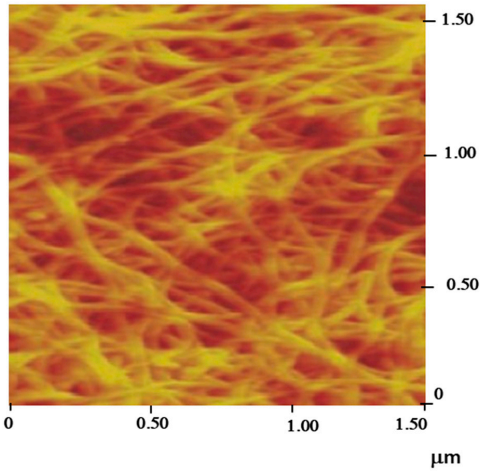

Figure 2. Atomic Force Microscopy image of a Single-walled carbon nanotube transferred film surface.

A pure platinum anode was used to charge the electrodes at one molar of NaOH electrolyte solution. The samples were submitted to the constant applied voltage (10 V during one h) accompanied by a significant increase in the electrolyte resistance. Additionally, and for comparison purposes, a cathode of pure palladium was used in the electrochemical cell together with the pure platinum anode, in the same above conditions.

Before and after the electrochemical hydrogen uptake, we used a Kern ABT-101 (Kern & Sohn, Balingen, Germany) analytical balance to weigh all the samples. This way, relative weight increases were recorded: 8% for Pd and 4% for the SWNT network. The MB-TDS procedure already described was then applied to each of the hydrogenated samples (using 1 °C min^{-1} for the heating rate). Figure 3 displays the desorption experimental spectra.

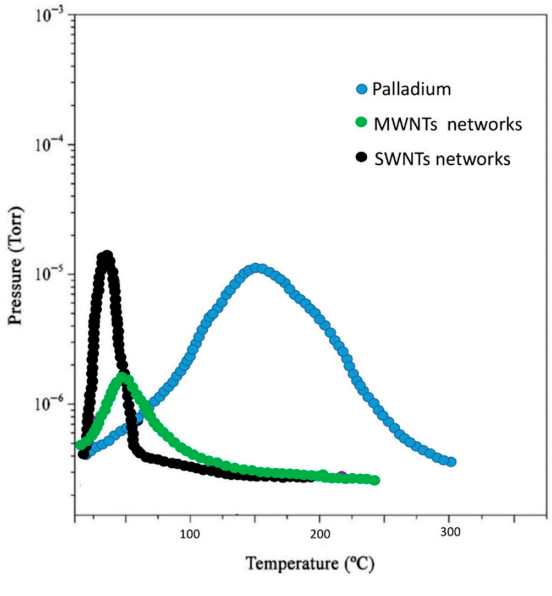

Figure 3. MB-TDS spectra were taken at a heating rate of 1 °C/min.

It is possible to compute the total hydrogen contained in each sample from the area of the respective MB-TDS recorded curve in Figure 3. This is done through the subtraction of the residual hydrogen background pressure (measured with the "beam-off") in identical experimental conditions. This way, each experimental desorption spectrum in Figure 3 can be fitted (due to the proportionality between X and the measured hydrogen pressure):

$$P = 1 - exp\left[\frac{G}{J}T^2 exp\left(\frac{-J}{T}\right)\right] \quad (12)$$

Here, $J = E_d/R$ and $G = -B/\beta$. This pressure reaches a maximum given by

$$P^{max} = 1 - exp\left[\frac{GJ}{4}exp(-2) + F\right] \quad (13)$$

where $F = ln\,(1 - P_0) - (J/G)\,T_0{}^2\,exp(-J/T_0)$, with P_0 and T_0 standing for, respectively, the hydrogen background pressure and room temperature at the instant just before the triggering of the heating- up. From this, one obtains the parameter J from the desorption spectra (Figure 3). Consequently, the area A_b below the recorded graphics is obtained through fitting the MB-TDS curves with Equation (12), and by subtracting the corresponding P_0. The area A_b mirrors the number of hydrogen molecules N_b detected with the QMS:

$$N_0 + N_b = (A_0 + A_b)\frac{N_A S}{RT} \quad (14)$$

where S represents pumping speed and N_A Avogadro number.

Furthermore, the number of hydrogen molecules still needs to be corrected due to experimental factors related to the QMS (geometrical fraction of the hydrogen jet effectively detected and its ionization efficiency). This allows for the subsequent estimation of the total amount of hydrogen released from each sample. Considering the QMS catalog technical specifications [7], an efficiency of about 70% is expected. Based on the geometric configuration conditions, it is possible to estimate 20% of the jet that effectively impinges the QMS. The combination of these two attenuation effects allowed us to estimate a reduction factor of the order of 10 in the molecular current that reaches the detector [7]. Thus, the true masses of hydrogen released from the samples can be calculated, and not surprisingly, they were in agreement with the relative weight increase values (previously recorded in the experimental part), only if they were multiplied by a factor of 10 (this is exactly the experimental attenuation factor already mentioned). In short, the total hydrogen content of each sample could then be calculated from the corresponding MB-TDS spectrum, providing an alternative way to avoid misleading weight results if hydrogen uptake is low.

From the relative corrected area of the spectra given in Figure 3, it was found that they agreed with the expected relative weight increases already mentioned:

Palladium = 8% → SWNT network = 4% → MWNT network = 2%

The wt% of hydrogen absorbed in carbon nanostructures is expected to be proportional to their respective specific surface areas [17], and in fact, the above experimental sequence seems likely to be explained by this argument, because the MWNT network had the highest value of the specific surface area.

By recording TDS spectra with other scan rates (2 K min^{-1} and 3 K min^{-1}) for each of the samples and fitting linear plots given by Equation (10) to the experimental points (β_i, T_{mi}), one could find the corresponding desorption energies E_d:

MWNT network = 18 kJ/mol → SWNT network = 20 kJ/mol → Palladium = 53 kJ/mol

This seems to reinforce the role of inter-tube sites in carbon nanostructures for storing hydrogen by a physisorption mechanism. Hydrogen desorption temperatures have reached as high as about 350 K, possibly due to the availability of "sub-nanometer" sized rooms [18].

The adsorption capacity is positively correlated with specific surface area and micropore volume. The hydrogen adsorption occurs inside and outside the tube, or at the gap of the array of bundles, and size, geometric, and arrangement of CNTs exert influence on hydrogen adsorption. Hydrogen can be physisorbed in carbon nanotubes bundles on various sites such as external wall surface, grooves, and interstitial channels. Therefore, it can a large energy density (as required for the mobile applications). It is also known that by tuning the adsorption conditions, hydrogen can either be chemisorbed or physisorbed on carbon nanotubes.

Usually, there are two hydrogen adsorption pathways in CNTs: the first is the physical adsorption of hydrogen molecules, which is favored at a high-pressure hydrogen atmosphere, and the second is electrochemical adsorption of hydrogen. Electrochemical hydrogen storage provides higher capacity at ambient temperature and atmospheric pressure than conventional hydrogen storage technology at low temperature and high pressure. Hydrogen storage takes place during the process of the electrolysis of water while protons become inserted into the host material. Carbonaceous materials with a mesoporous structure also demonstrate the capability of up-taking H_2 through the insertion of atomic H, which favors stabilization of the hydrogen absorbed.

For bulk palladium, it is known that a hydrogen molecule chemisorbs on the surface adsorption sites following dissociation into individual atoms even at low temperatures. After filling most of the surface sites, hydrogen atoms start to occupy the subsurface region, where the hydrogen atoms are bound weaker than the adsorbed atoms on the surface. Thus, hydrogen spontaneously desorbed is measured in TDS, together with hydrogen coming from activated desorption.

Although there are no catalytic properties ascribed to the allotropic forms of carbon, it is known to be an active catalyst in some oxidation reactions. Among their many other interesting properties, carbon nanotubes have been found to act as catalysts for some important chemical reactions including some that could be used to make cleaner fuels. Furthermore, the exceptional physical properties of carbon nanotubes such as large specific surface areas, excellent electron conductivity incorporated with good chemical inertness, and relatively high oxidation stability make it a promising support material for heterogeneous catalysis instead of the conventional alumina, silicon, or activated carbon supports. One or more kinds of catalysts can be loaded on the high surface area of the CNT nanomaterial, which serves as the support, to form a supported catalyst as a whole system. In a supported catalyst system, the significance of using the support is to increase the dispersion of the active phases, to have better control of the porous structure, to improve mechanical strength, to prevent sintering, and to assist catalysis.

The combination of physisorption in the nanocarbon porous material with chemisorption in chemical hydrides and the presence of a metal hydride are the key advantages of the proposed hydrogen sorbents with high stabilities, and high adsorption/desorption kinetics.

Hydrogen spillover arises in hydrogen catalyzed reactions on supported metal catalysts. Dihydrogen molecules dissociate on the metal part of the catalyst. Some hydrogen atoms remain attached to the metal, whilst others diffuse to the support.

An applicable spillover sorbent should: (a) permit the diffusion of H_2 or H atoms in a well-dispersed pore lattice, (b) have most of the interior pore surface area disposable to encounter with spillover H_2 or H, and (c) be lightweight to maximize the gravimetric hydrogen uptake. Thus, the hydrogen uptake in mesoporous carbon, which has a suitable surface area, and proper porosity and low density can be augmented substantially by hydrogen spillover.

4. Conclusions

This work reports an effective method for real-time quantitative analysis of hydrogen in different materials by using the MB-TDS technique. Several advantages such as time-efficiency and without using the calibration step can provide insight into researchers who want to quantitatively measure the hydrogen storage capacity. This MB-TDS methodology

can be used to detect the hydrogen adsorbed at different types of nanomaterials (metal oxides, layered double hydroxides, or nanoparticles with surface capping agent, i.e., several types of organic molecules could be adsorbed at the surface of nanomaterials during the electrocyclic tests), as long as they possess suitable thermal stability at the working temperatures of desorption.

MB-TDS has been proven to be an effective method for real-time quantitative analysis and in situ capture of hydrogen with any type of hydrogen storage material, even if the amount is below the microbalance detection limit. Additionally, to perform a quantitative analysis of hydrogen storage capacity, the device does not need to be calibrated by introducing a certain number of hydrogen molecules into the vacuum system, unlike in conventional TDS. Furthermore, it was not needed to work in an ultra-high vacuum, which would add more time-consuming and unnecessary procedures.

In contrast to activated carbons, carbon nanostructures are promising for hydrogen storage technological applications, since they are much lighter than alternative metals (as palladium) or metal hydrides in metal alloys. Activated carbons are not efficient enough as hydrogen capture systems because only a small fraction of the pores (from their pore size distribution) are small enough to interact strongly with the gas phase hydrogen molecules. For small-sized systems, surface- or interface-related sites assume crucial importance and can change the overall solubility of hydrogen.

Carbon nanotubes, due to their high surface area and chemical durability, have great potential as hydrogen adsorbents. They can adsorb hydrogen by physisorption and/or chemisorption mechanisms. Hydrogen can be physisorbed in carbon nanotube bundles on various sites such as external wall surface, grooves, and interstitial channels. Therefore, it can have a large energy density (as required for mobile applications). It is also known that by tuning the adsorption conditions, hydrogen can be either chemisorbed or physisorbed on carbon nanotubes.

However, in the MB-TDS experiments, our mass spectrometer was unable to distinguish between adsorbed molecular and atomic hydrogen. For that, a QMS with improved mass resolution will be needed.

This methodology offers several advantages, paving the way for future developments in comparing the intrinsic activity of nanomaterials because it allows for the combination of the mass of hydrogen monitoring with the electrochemical active surface area (ECSA) of the electrodes.

Author Contributions: Conceptualization, R.L.; Investigation, R.L., J.R. and F.I.; Supervision, R.L. All authors have read and agreed to the published version of the manuscript.

Funding: This research received no external funding.

Acknowledgments: This work was financed by national funds registered in the budget of FCT—Foundation for Science and Technology within the scope of the Research Unit CTS—Center for Technology and Systems, under the reference UIDB/00066/2020. FCT-MCTES Portugal through SFRH/BSAB/135131/2017 is also gratefully acknowledged.

Conflicts of Interest: The authors declare no conflict of interest.

References

1. Thornburg, N.; Abdelrehim, I.; Land, D. Kinetics of Propene Desorption from Pd (111) Studied by Thermal Desorption. *J. Phys. Chem. B* **1999**, *103*, 8894–8898. [CrossRef]
2. Zaluska, A.; Zaluski, L.; Ström-Olsen, J. Nanocrystalline magnesium for hydrogen storage. *J. Alloy. Compd.* **1999**, *288*, 217–225. [CrossRef]
3. Castro, F.; Meyer, G.; Zampieri, G. Effects of sulfur poisoning on hydrogen desorption from palladium. *J. Alloys Compd.* **2002**, *612*, 330–332. [CrossRef]
4. Redhead, P. Thermal desorption of gases. *Vacuum* **1962**, *12*, 203–211. [CrossRef]
5. Huot, J.; Liang, G.; Schulz, R. Mechanically alloyed metal hydride systems. *Appl. Phys. A Mater. Sci. Process.* **2001**, *72*, 187–195. [CrossRef]

6. Ballenweg, S.; Gleiter, R.; Krätschmer, W. Hydrogenation of buckminsterfullerene C_{60} via Hydrozirconation: A new way to organofullerenes. *Tetrahedron Lett.* **1993**, *34*, 3737–3740. [CrossRef]
7. Lobo, R.F.M.; Berardo, F.M.V.; Ribeiro, J.H.F. Molecular beam-thermal hydrogen desorption from palladium. *Rev. Sci. Instrum.* **2010**, *81*, 043103. [CrossRef] [PubMed]
8. Lobo, R.F.M.; Santos, D.M.F.; Sequeira, C.A.C.; Ribeiro, J.H.F. Molecular Beam-Thermal Desorption Spectrometry (MB-TDS) Monitoring of Hydrogen Desorbed from Storage Fuel Cell Anodes. *Materials* **2012**, *5*, 248–257. [CrossRef] [PubMed]
9. Merzlikin, S.V.; Borodin, S.; Vogel, D.; Rohwerder, M. Ultra high vacuum high precision low background setup with temperature control for thermal desorption mass spectroscopy (TDA-MS) of hydrogen in metals. *Talanta* **2015**, *136*, 108–113. [CrossRef] [PubMed]
10. Hanna, T.; Hiramatsu, H.; Sakaguchi, I.; Hosono, H. Highly hydrogen-sensitive thermal desorption spectroscopy system for quantitative analysis of low hydrogen concentration ($\sim 1 \times 10^{16}$ atoms/cm^3) in thin-film samples. *Rev. Sci. Instrum.* **2017**, *88*, 053103. [CrossRef] [PubMed]
11. Miyase, T.; Watanabe, K.; Sakaguchi, I.; Ohashi, N.; Domen, K.; Nomura, K.; Hiramatsu, H.; Kumomi, H.; Hosono, H.; Kamiya, T. Roles of Hydrogen in Amorphous Oxide Semiconductor In-Ga-Zn-O: Comparison of Conventional and Ultra-High-Vacuum Sputtering. *ECS J. Solid State Sci. Technol.* **2014**, *3*, Q3085–Q3090. [CrossRef]
12. Woodruff, D.P.; Delchar, T.A. *Modern Techniques of Surface Science*; Cambridge University Press: Cambridge, UK, 1994. [CrossRef]
13. Zeppelin, F. *Untersuchung der Desorptionskinetik von Metallhydriden*; Cuvillier Verlag: Göttingen, Germany; Max Planck Institut: Stuttgart, Germany, 2004.
14. Yates, J. *Solid State Physics: Methods of Experimental Physics*; Park, R., Lagally, M., Eds.; Academic Press: New York, NY, USA, 1985; Volume 22, ISBN-13: 978-0124759640.
15. Beeby, J. The theory of desorption. In *Critical Reviews in Solid State and Materials Sciences*; Vanselow, R., Ed.; CRC Press: Boca Raton, FL, USA, 1977; Volume 7, pp. 153–166. [CrossRef]
16. Chen, Z.; Ren, W.; Gao, L.; Liu, B.; Pei, S.; Cheng, H.-M. Three-dimensional flexible and conductive interconnected graphene networks grown by chemical vapour deposition. *Nat. Mater.* **2011**, *10*, 424–428. [CrossRef] [PubMed]
17. Schlapbach, L.; Züttel, A. Hydrogen-storage materials for mobile applications. *Nature* **2001**, *414*, 353–358. [CrossRef] [PubMed]
18. Shiraishi, M.; Takenobu, T.; Yamada, A.; Ata, M.; Kataura, H. Hydrogen storage in single-walled carbon nanotube bundles and peapods. *Chem. Phys. Lett.* **2002**, *358*, 213–218. [CrossRef]

nanomaterials

MDPI

Article

Synthesis of Highly Active Pd@Cu–Pt/C Methanol Oxidation Electrocatalysts via Continuous, Co-Electroless Deposition

Gregory L. Tate [1], Bahareh Alsadat Tavakoli Mehrabadi [1,2], Wen Xiong [1], Adam Kenvin [1] and John R. Monnier [1,*]

[1] Department of Chemical Engineering, University of South Carolina, Columbia, SC 29208, USA; gltate@email.sc.edu (G.L.T.); bahareh.mehrabadi@nikolamotors.com (B.A.T.M.); wxiong@email.sc.edu (W.X.); akenvin@email.sc.edu (A.K.)
[2] Research and Development, Nikola Motors, Phoenix, AZ 85040, USA
* Correspondence: monnier@cec.sc.edu; Tel.: +1-803-777-6813

Abstract: Controlled deposition of metals is essential for the creation of bimetallic catalysts having predictable composition and character. Continuous co-electroless deposition (co-ED) permits the creation of bimetallic catalysts with predictive control over composition. This method was applied to create a suite of Cu–Pt mixed-metal shell catalysts for use in methanol electrooxidation in direct methanol fuel cell applications (DMFCs). Enhanced performance of Cu–Pt compositions over Pt alone was predicted by existing computational studies in the literature. Experimental evidence from this study supports the bifunctional catalyst explanation for enhanced activity and confirms the optimum Cu:Pt ratio as Cu_3Pt for this methanol electrooxidation. This ability to control the composition of a bimetallic shell can be extended to other systems where the ratio of two metals is critical for catalytic performance.

Keywords: bifunctional catalyst; electroless deposition; fuel cells; heterogeneous catalysis; preparation

Citation: Tate, G.L.; Mehrabadi, B.A.T.; Xiong, W.; Kenvin, A.; Monnier, J.R. Synthesis of Highly Active Pd@Cu–Pt/C Methanol Oxidation Electrocatalysts via Continuous, Co-Electroless Deposition. *Nanomaterials* **2021**, *11*, 793. https://doi.org/10.3390/nano11030793

Academic Editors: Ioannis V. Yentekakis and César Augusto Correia de Sequeira

Received: 22 January 2021
Accepted: 15 March 2021
Published: 19 March 2021

1. Introduction

The move toward more environmentally sound transportation and portable power devices has been an important focus of research in recent years. Fuel cells have provided an alternative way to supply power since the 1960s [1]. However, there are bottlenecks, one being the low-energy density of hydrogen (10.8 MJ/m^3 at STP) and the challenges of storing, metering, and transporting a highly compressed and flammable gas [2]. A promising alternative technology is to replace H_2 with methanol as a hydrogen source. Methanol is much more energy-dense (18.1 GJ/m^3 at STP) than H_2 and exists as a "drop-in" fuel [2]. Existing gasoline metering and distribution can be converted to methanol without much difficulty.

Direct methanol fuel cells (DMFCs), however, also have limitations regarding their activity. The oxidation of methanol produces CO as an intermediate, and Pt strongly adsorbs CO. Thus, CO inhibits further MeOH oxidation placing an upper limit on the rate of MeOH oxidation [3,4].

There are three reactions that take place during methanol electrooxidation. The first reaction is the adsorption of methanol on Pt, where it decomposes into CO, donating $4e^-$ to the electrode and liberating $4H^+$ (Equation (1)). The second reaction is the decomposition of water on Pt to give OH and H^+ and one e^- (Equation (2)). The final reaction (Equation (3)) is the oxidation of CO with adsorbed OH to form CO_2, which easily desorbs to complete the catalytic cycle [3–7]:

$$CH_3OH + Pt \rightarrow Pt\text{-}CO + 4H^+ + 4e^- \quad (1)$$

$$H_2O + Pt \rightarrow Pt\text{-}OH + H^+ + e^- \quad (2)$$

$$\text{Pt-OH} + \text{Pt-CO} \rightarrow CO_2 + H^+ + 2\text{Pt} + e^- \quad (3)$$

At most operating conditions, the rate-determining step is generally accepted to be the oxidation of adsorbed CO. One of the methods to lower the inhibition effect of CO involves the addition of a second metal proximal to the active Pt component. Proper placement of the second metal can alter the electronic structure of Pt or provide a different catalytic site to introduce bifunctionality. It has been experimentally shown that the d-band of Pt can be altered by either lattice compression or expansion, which changes the adsorption strength of CO on Pt [8,9]. Bifunctionality involves the addition of a second metal in close proximity to Pt that functions as an adsorption site for the decomposition of H_2O to give $OH_{ads,}$ which can react with Pt-CO to form CO_2 by reaction (3) [5,10–12]. This bifunctional mechanism is believed to be responsible for the enhanced activity of the Ru–Pt system for methanol electrooxidation [11]. Indeed, the addition of ruthenium to platinum supported on carbon using electroless deposition methods has been shown [12,13] to be an effective method of dramatically increasing DMFC activity, corroborating the bifunctional mechanism proposed earlier by Watanabe [10–12], among others.

The key is to be able to control the amounts and locations of the two metal components to give the optimal effect. Typically, the most common method is co-impregnation, co-precipitation, or co-reduction of both metal salts on the carbon support [14]. With these procedures, there is no assurance that bimetallic particles are consistently formed or that the bimetallic particles have uniform compositions. Thus, analyses and performances of materials are based on average bulk compositions instead of true metal ratios at the bimetallic particle scale. To solve this, electroless deposition (ED) has been used to selectively deposit the second metal only on the surface of a pre-existing primary metal by catalytic activation of a reducing agent on the primary metal surface [10,13,15–20]. This process ensures that the secondary metal is deposited only on the primary metal and not on the support [15]. For example, in earlier work [12], bimetallic catalysts with different monolayer (ML) coverages of Ru on 20 wt % Pt/C were prepared by ED and evaluated for methanol electrooxidation. The Pt mass activity ($425 A/g_{Pt}$) of the sample with 0.5 ML Ru coverage (1.1 wt % Ru—surface Pt:Ru = 1:1) was seven times higher than a 20 wt % Pt/C catalyst and 3.5 times higher than a commercial catalyst with a 1:1 Pt: Ru bulk atomic ratio of 6.8 wt % Ru—13.2 wt % Pt/C. Additionally, the amount of Ru required for the highest activity was only 1.1 wt % Ru, compared to 6.8 wt % Ru for the commercial catalyst. The ability of ED to target Ru only on the Pt surface dramatically lowered Ru requirements.

In this study, we use electroless deposition to prepare Cu–Pt catalysts for methanol electrooxidation. However, rather than depositing Cu on a Pt surface, both Cu and Pt have been simultaneously co-deposited on a different core metal particle to create a mixed Pt–Cu shell on a primary metal core. In this process, two metal salts are simultaneously added along with a reducing agent to an ED bath containing a 5 wt % Pd/C base catalyst. The relative ratios of metal deposition are controlled by the intrinsic reduction potentials of the metal salts and the concentrations and pumping rates of the Cu and Pt salts. The reasons for codeposition are to prepare a more uniformly distributed, bimetallic layer to maximize bifunctionality and possibly improve stability. Further, it should be possible to use minimal amounts of each of the two metals to reduce the cost of synthesis. While this is not critical for Cu, it is clearly an important consideration for the much more expensive Pt component.

Cu–Pt alloys were selected because they have been studied both experimentally and computationally for MeOH electrooxidation and represent a good case for comparison. One of the benefits of using ED for the deposition of either single metals or deposition of two metals is the general versatility of this method. Experimental studies have shown increased activity for Cu–Pt alloys relative to either Pt or Cu catalysts [5]. It is also known that Cu dissociates H_2O and does not adsorb CO, and should provide a bifunctional site for OH_{ads} [21]. Additionally, computational literature has predicted that several Pt–X (X = Cu, Ru, Sn) alloys could provide lower overpotential for methanol electrooxidation compared to Pt alone [5]. Rossmeisl and Tritsaris [6] calculated that a Cu_3Pt surface moiety offers the lowest overpotential for MeOH electrooxidation. Since continuous codeposition should

permit very good control over the shell composition, Cu–Pt shells have been prepared over a range of Cu and Pt ratios to determine the optimum catalyst composition and whether experimental results are corroborated with computational predictions.

Any metal with sufficient ability to oxidize a reducing agent can be selected as a core metal, but for these studies, a commercial 5 wt % Pd/C (dispersion = 21.6%, average particle diameter = 5.2 nm) was selected as the core metal base catalyst (Engelhard 5 wt % Pd/CP56). Although the existence of ternary Pt–Cu–Pd alloys is argued in the literature, the low-temperature aqueous method of preparation is thought to preclude any bulk ternary alloy formation [22–25]. There is insufficient thermal energy to force alloying of the Cu–Pt shell with the bulk Pd core at room temperature. It is presumed that the shell contains Cu and Pt alone. Furthermore, of importance, palladium is known to be inactive for methanol electrooxidation under acidic conditions [26–29], ensuring that activity was only from the Pt–Cu shell and not the Pd core.

2. Materials and Methods

2.1. Catalyst Preparation

A series of Pt–Cu/Pd/C catalysts was prepared by continuous co-ED following the general procedures discussed in prior work [30]. The core catalyst on which the mixed-metal shell is deposited is commercial 5 wt % Pd/C (disp = 21.6% D = 5.2 nm) was used as received. In this case, a master 300 ppm $PtCl_6^{2-}$ solution was prepared. To this solution, a 5:1 molar equivalent of ethylenediamine (EN) as stabilizing agent to prevent the unwanted thermal reduction of $PtCl_6^{2-}$ (with the reducing agent) was added to the volume of the $PtCl_6^{2-}$ solution to be loaded into the syringe preceding the ED experiment. A 500 ppm copper solution was prepared fresh daily from $Cu(NO_3)_2{\cdot}6H_2O$. No complexing agent was added to this solution because of the lower reduction potential of Cu^{2+} compared to $PtCl_6^{2-}$ (E° = 0.34 V and E° = 0.72 V, respectively). Reducing agent selection was based on the work of Ohno [31] and Djokić [32]. Dilute aqueous hydrazine was selected as the reducing agent because of its facile oxidation over Pd, Pt, and Cu at slightly alkaline conditions and the "clean" nature of oxidation (N_2H_4 oxidizes into H_2O and N_2, whereas other reducing agents can leave decomposition products that can affect the ED process.) The amount of N_2H_4 was selected to be in excess of the electron requirements for all metal salts by a factor of 5:1 because the inherent instability of N_2H_4 results in H_2 evolution to give inefficient use during ED. The overall equations for continuous co-ED are listed as Equations (4)–(6) as proposed by Djokić [32]. N_2H_4 is initially adsorbed and dissociated on the Pd core to give four adsorbed H species, which in turn reduce $Pt(EN)_xCl_6^{2-}$ and Cu^{2+} leaving Pt^0 and Cu^0 on the surface (Equations (5) and (6)). As the reaction proceeds, N_2H_4 can be readily adsorbed and oxidized on deposited Pt^0 and Cu^0, providing additional locations for Cu or Pt salt reduction. The values of the oxidation and reduction potentials for each of the reactants indicate ED should readily occur:

$$N_2H_4 + Pd^0 \rightarrow N_2 + 4H_{ads}\ \text{(basic)} \quad E^\circ = +1.16\ V \tag{4}$$

$$Pt(EN)_xCl_6^{2-} + 4OH^- + 4H_{ads} \rightarrow Pt^0 + xEN + 6Cl^- + 4H_2O \quad E^\circ = +0.72\ V \tag{5}$$

$$Cu^{2+} + 2OH^- + 2H_{ads} \rightarrow Cu^0 + 2H_2O \quad E^\circ = +0.34\ V \tag{6}$$

To perform continuous co-ED, 500 mg of base catalyst was added to DI water in a disposable plastic beaker and pH was adjusted to 9 using a NaOH solution. All three microcontroller-driven syringe pumps were started simultaneously, and the molar rate of pumping was controlled by the concentration of the solution and individual pumping rates to give the desired ratios of Pt and Cu deposited on the core metal. A schematic of the experimental setup is shown in Figure 1. Three microcontroller-driven syringe pumps (New Era Pump Systems, NE-300, Farmingdale, NY, USA) were used to add each reagent separately at set rates (Cu salt, Pt salt, and N_2H_4). The ED bath was continually stirred, and pH was monitored throughout the reaction. The pH of the solution was adjusted by 0.1 M NaOH or HCl, if necessary, throughout the course of the experiment to

maintain pH = 9. In all cases, a combined Cu and Pt shell of five theoretical monolayers was targeted, although the actual coverage of the bimetallic shell depended on the actual amount of metal deposited. Active Pd surface area site concentration used for theoretical ML calculations was determined from H_2–O_2 titration (AutoChem II 2920 Chemisorption analyzer, Micromeritics, Norcross, GA, USA) of the Pd core catalyst. Aliquots (0.5 mL) of the ED bath were taken at preselected time intervals during the course of the experiment to determine the number of metal salts remaining in the solution (and by difference, the number of metals deposited on the base catalyst). After the deposition time was completed, the catalyst was vacuum filtered and rinsed with a large excess of DI water to remove unreduced metal ions, EN, and N_2H_4 (not likely to be present due to instability and non-selective evolution of H_2.) Aliquots were immediately analyzed by AAS (PerkinElmer AAnalyst 200, Waltham, MA, USA). All samples were dried overnight in flowing air at 25 °C and then stored in capped bottles.

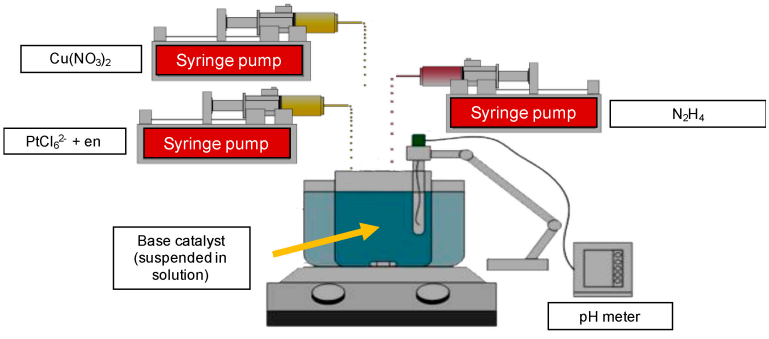

Figure 1. Image of the experimental setup for continuous co-electroless deposition (co-ED). New Era Pump Systems NE-300 pumps were used to add reagents during ED. A pH meter continuously monitored the pH of the ED bath. Bath temperature was maintained (in this case at 25 °C) but could be controlled up to 90 °C using a digital, PID heated stirrer to regulate temperature and stir the bath.

For comparison, a commercial 20 wt % Pt/XC72 sample was evaluated for methanol electrooxidation. This catalyst was evaluated as-received and characterized by STEM, XRD, and H_2–O_2 titration to give average diameter d: d(STEM) = 3 ± 1 nm, d(XRD) = 3.2 nm, and d(H_2–O_2 titration) = 6.1 ± 0.3 nm.

2.2. Characterization

Dried samples were analyzed by powder XRD (Rigaku Miniflex with D/tex Ultra 250 1D silicon strip detector, Tokyo, Japan) to determine whether Pt or Cu oxides were present. If bulk Pt or Cu oxides were present, it would suggest that uniform deposition did not occur during ED. Bulk Cu^0 particles at the nm scale would likely undergo facile oxidation to Cu_2O, while deposition of a mixed alloy Pt–Cu shell should inhibit the formation of a bulk Cu_2O phase. Further, the presence of crystalline Pt^0 and Cu^0 phases would also indicate segregation of the two components during co-ED.

Additionally, to quantify Pt site concentrations at the surface of the shell, H_2–O_2 titration (AutoChem II 2920 Chemisorption analyzer, Micromeritics, Norcross, GA, USA) was used to characterize all samples. All samples were exposed to a flowing stream of H_2 for 1 h at 45 °C. Following this, the sample was swept with flowing Ar for 1 h at the same temperature to remove any physically adsorbed H_2. The sample was next pre-covered with oxygen by flowing in 10% O_2/balance He for 30 min, and residual O_2 was removed by flowing in Ar for 30 min. Titration of the surface was done with 10% H_2/balance Ar pulses, dosed until the peak area did not change [33,34]. Uptake was determined by the summation of pulse area and gas loop volume. This procedure was repeated three times per sample to ensure reproducibility, with average values and standard deviation reported.

STEM imaging was performed on select samples to determine catalyst morphology and ensure core-shell structure with mixed Cu–Pt shell. A JEOL 2100 F 200 kV scanning transmission electron microscope(Tokyo, Japan) equipped with a CEOS Cs-corrector illumination source and Fischione Model 3000 high angle annular dark-field (HAADF, Export, PA, USA) detector was used for imaging. Minimization of line noise was accomplished by synchronized 60 Hz scanning, with 15.8 µs pixel dwell time.

No pretreatment, other than drying at room temperature in flowing air, was used before any characterization procedure.

2.3. Cyclic Voltammetry

Cyclic voltammetry (CV) procedures are largely repeated from previous work with a different catalyst system studying the same reaction [12]. Cyclic voltammetry studies were performed using a 5 mm diameter Pt disk coated with catalyst as the working electrode with a bare Pt wire used as the counter electrode. For the reference electrode, a Luggin capillary Hg/Hg_2SO_4 electrode was employed. To coat the working electrode, an ink was prepared by sonicating 10 mg of dry catalyst in a 10 mL solution consisting of a 1:1 volumetric ratio of isopropyl alcohol (IPA) and DI water, the electrode ink having a final catalyst concentration to solvent ratio of 1 g/L. To coat the working electrode, an 18.5 µL sample of the ink was added dropwise to the Pt disk. To secure the ink to the surface of the electrode, a 5 µL solution of 5 wt % Nafion: IPA was added atop the ink.

CV analyses were performed using an N_2-purged bath of 0.5 M H_2SO_4 and 1 M MeOH; all evaluations were performed at 25 °C. At bath conditions, the reference electrode had a potential of 0.682 V versus the standard hydrogen electrode (SHE) and all potentials reported are referenced to SHE value [35]. All catalysts were conditioned for 50 cycles before CV measurements at a rate of 50 mV/s from 0–1.2 V. CV measurements were performed from 0–1.2 V at a rate of 5 mV/s and repeated three times to ensure reproducibility. The average forward peak current (I_f) at ~0.85 V from these three trials was used to determine reported methanol electrooxidation activity.

3. Results

3.1. Preparation/Synthesis

The kinetics for two examples of co-electroless deposition are shown in Figure 2a,b. Figure 2a shows Cu and Pt deposition for the addition of equal molar concentrations of $PtCl_6^{2-}$ and Cu^{2+} over a 60 min time interval. The straight-line deposition rates over the full time interval indicate the formation of a shell with constant bimetallic composition. As stated earlier, a hydrazine solution at 5× molar excess was added from a third syringe. Approximately 50 µmol of each salt was added over a 60 min period, and then the bath was left in a batch mode for an additional 60 min. The results clearly show that $PtCl_6^{2-}$ is reduced much more rapidly than Cu^{2+}, possibly because of the higher reduction potential of $PtCl_6^{2-}$ compared to Cu^{2+}, although kinetics are favorable for both salts. From 60–120 min, there is a small amount of additional Cu deposition, indicating some residual N_2H_4 is left in the bath. The final composition of the bimetallic shell was $Cu_{0.23}Pt_1$ on 5 wt % Pd/carbon. Figure 2b shows ED kinetics for a bath selected to give a higher Cu:Pt ratio. In this case, 240 µmol and 80 µmol of Cu^{2+} and $PtCl_6^{2-}$, respectively, were added over a 60 min period to give a final composition of $Cu_{1.6}Pt_1$. Interestingly, there was an apparent induction period for deposition of Cu^0, while Pt was deposited at the outset. The Cu kinetic plot does show, however, that the analyzed Cu^{2+} in the bath agrees very well with the amount of Cu^{2+} syringe-pumped into the bath for the first 20 min interval. Similar experiments were conducted for different bath compositions, and the results are summarized in Table 1. In Table 1, the amounts of Pt and Cu deposited for all samples are shown to illustrate the range of these components in the shell layer. Since the complete deposition of both components did not occur at the deposition conditions that were used, a plot of target deposition vs. actual deposition was constructed and shown in Figure 2c to help select the concentrations to be used for a particular bimetallic shell composition.

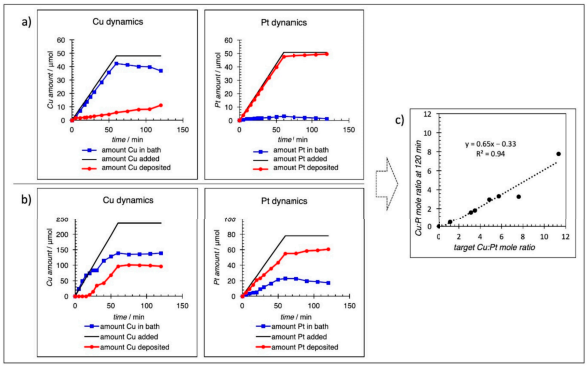

Figure 2. Deposition kinetics for a feed ratio of (**a**) 1:1 = Cu:Pt (**b**) 3:1 = Cu:Pt. The solid line indicates the total amount of metal added, the red line indicates metal deposited in the mixed shell, and the blue line indicates the metal salt remaining in the bath. Final shell composition was (**a**) Cu:Pt = 0.23:1 and (**b**) Cu:Pt = 1.6:1. Results from deposition kinetics shown for all materials made plotted (**c**) where the amount of Cu:Pt added by a syringe pump (target) is compared to the amount (Cu:Pt) actually deposited after 120 min. Linear regression is shown by the dashed line.

Table 1. Summary of catalysts prepared and tested with cyclic voltammetry. One ML is defined as the number of atoms required to cover the surface of the Pd core. The surface concentration of the Pd core was determined by H-titration of O-pre-covered Pd. Weight loadings of Pt and Cu refer to weight loadings of each metal added to the 5% Pd/C. The Pd loading was not factored into the Pt and Cu loadings. The concentration of Pt surface sites was determined from the H_2 titration of O-pre-covered Pt sites.

Empirical Formula	Pt (wt %)	Cu (wt %)	ML (Cu + Pt)	Number of Pt_s (10^{18} Sites × g^{-1} Cat)
$Cu_{0.2}Pt_1$	1.9	0.14	1.2	40
$Cu_{1.6}Pt_1$	2.4	1.2	3.1	17
$Cu_{1.7}Pt_1$	1.9	1.0	2.5	30
$Cu_{3.0}Pt_1$	2.3	2.2	4.5	21
$Cu_{3.3}Pt_1$	1.1	1.2	2.4	8.1
$Cu_{5.5}Pt_1$	0.90	1.8	3.3	4.8
$Cu_{6.1}Pt_1$	1.1	2.0	3.7	2.7

3.2. Physicochemical Characterization

XRD patterns of selected samples are shown in Figure 3. A Rigaku Miniflex XRD with an ultra-high sensitivity D/tex Ultra 250 1D silicon strip detector has sufficient sensitivity to determine the existence of crystalline structures at these low weight loadings, as evidenced from previous studies [36,37]. For all samples, neither Cu_2O peaks nor sharp Pt peaks indicative of larger Pt particles were detected, consistent with the assumption that the shell is a uniformly mixed alloy and that segregation into discrete Pt and Cu particles had not occurred. A broad peak does exist in the region between the (111) planes of Pt and Cu, and according to Vegard's law, the lattice parameter of a solution-phase alloy is a weighted composition of the individual constituents' lattice parameters. Thus, the peak lies in the expected region for a Cu–Pt shell [38]. Additionally, the peak broadening suggests very small domain sizes, in accordance with the maximum of ~5 ML shell metals deposited by continuous co-ED (Table 1). Shell thicknesses have been previously determined in our laboratory by Scherrer peak broadening for $Pt@Pt_2O_3$ species using this same technique; the diffuse broad peaks are an indication that the shell is, indeed, of mixed Cu–Pt character [39]. Additionally, the XRD patterns show that the base Pd peaks neither shift position (indicating no alloy formation with Pt or Cu according to Vegard's law) nor change in

shape (indicating no growth of the Pd core due to alloying). Thus, we can conclude that the base Pd/C catalyst is substantially unchanged by the co-ED procedure. A broad peak at $2\theta = 34^\circ$ in Figure 3c,d could be attributed to PdO. This peak decreases in intensity in Figure 3a,b. Oxidation of Pt nanoparticles supported on carbon under ambient conditions was shown by Banerjee et al. as a shell of Pt oxides over a core of Pt [39]. Given that the oxidation potential of Pd is greater than Pt, it is not unexpected to see surface oxidation [40]. PdO is readily reduced by N_2H_4 in the ED bath. Re-oxidation of exposed Pd post-ED could be one explanation for the reappearance of PdO in 3c.

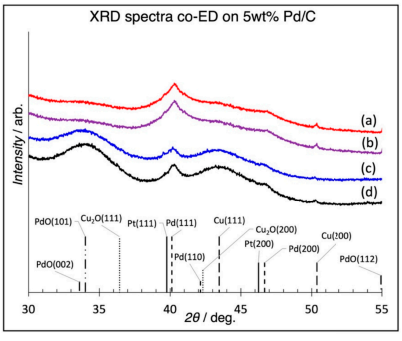

Figure 3. Powder XRD patterns of base $Cu_{5.8}Pt$ (**a**), $Cu_{3.3}Pt$ (**b**), $Cu_{0.18}Pt$ (**c**), and 5 wt % Pd/C catalyst (**d**). The absence of Cu_2O peaks supports the mixed Pt–Cu shell assignment. The unresolved, broad and diffuse peaks between Pt(111) and Cu(111) are consistent with mixed Cu–Pt alloy shell. The absence of Cu_2O, Cu^0, or Pt^0 peaks indicates no formation of these species and that phase segregation had not occurred.

Since Pt is the active site for methanol electrooxidation, it is helpful to determine the concentration of Pt surface in the samples using methods other than the electrochemical surface area. To determine the amount of exposed Pt, H_2 titration of O-pre-covered Pt was used [33,34]. Cu^0 is not active for H_2 titration at ambient conditions. Higher heating temperatures were not used to intentionally minimize the potential of Pt and Cu de-alloying in the shell and to prevent the high-temperature formation of Pt–Pd alloys (from the core). Pt and Pd readily form solid solutions across all compositions at elevated temperatures [41,42]. Ternary Pt–Cu–Pd alloys can potentially form at high-temperature; therefore, no high-temperature treatment was used to preserve the Cu–Pt shell/Pd core morphology [22–25]. The results from H_2 titration are shown in Figure 4. The uptake of H_2 decreases with higher Cu/Pt ratios as expected since surface Pt becomes more diluted by Cu, and Cu–O requires elevated temperatures for chemisorption. We also assume that no Pd sites are exposed for the Cu–Pt alloy, which may, in fact, not be the case for some compositions. If surface Pd is present, it will also be active for H_2 titration. In these cases, the Pt surface site concentration would be over-stated, and methanol oxidation activities relative to Pt surface areas would be under-calculated. Regardless, active site concentrations based on chemisorption are a way to standardize specific activities, which are typically done in conventional catalysis [43,44]. Additionally, there is good agreement in the literature between Pt surface area calculated by chemisorption methods and by H-stripping electrochemical methods [45,46].

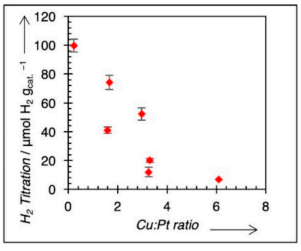

Figure 4. H_2 titration results for O-pre-covered catalysts. Values decline as Pt is diluted by Cu on the Pt–Cu surface.

Results from STEM *Z*-contrast imaging show a uniform distribution of Pt (individual bright spots) over a Pd core. Pd is medium gray, and Cu is dark gray in *Z*-contrast. The distribution of Pt in the shell looks to be both uniform and random. Figure 5a,b shows representative particles. Lattice fringes are present in both images, indicating the ordered Pd core, with a halo surrounding the core containing both bright specks, Pt, and dark gray, Cu. Lattice fringes were analyzed with FFT in ImageJ software, and d-spacing was measured to be 0.23 nm [47]. The known d-spacing for Pd(111) is 0.223 nm; this corroborates the statement that these lattice fringes arise from the Pd core. Figure 5c shows uniform speckling on several particles, indicating that co-ED produces uniform shells of randomly distributed Cu and Pt over Pd cores and that 5a and 5b are representative particles for the overall sample.

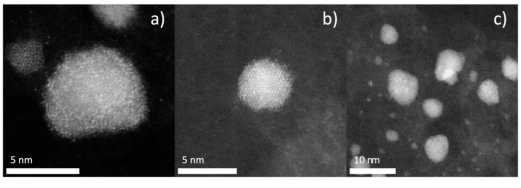

Figure 5. TEM images of $Cu_{3.3}Pt_1$ sample. *Z*-contrast imaging shows Pt as bright white spots, with Cu shown in darkest gray. The speckling of white spots in (**a**,**b**) show a uniform distribution of Pt in the shell, lattice fringes arise from ordered Pd core (d-spacing calculated from lattice fringes in images (**b**,**c**) equal 0.23 nm, corresponding to known d-spacing of Pd (111) diffraction, 0.223 nm) Uniform core-shell formation can be seen in image (**c**) showing even speckling across several particles.

3.3. Electrochemical Characterization

Cyclic voltammetry was conducted on all samples, and the results are included in Table 2. Each voltammogram shows two remarkable anodic peaks, one in the forward scan (I_f) and the other in the backward scan (I_b). The forward current, I_f at ~0.85 V, normalized to the mass of Pt (mass activity), was measured as the marker for MeOH electrooxidation activity, in accordance with prior literature [11,12]. Figure 6a,b shows two CV traces for two samples, $Cu_{0.23}Pt_1$ and $Cu_{1.6}Pt_1$, respectively. The forward peak current (I_f) and the backward peak current (I_b) were marked in Figure 6. Only the forward current (I_f) was used to determine the mass activity for MeOH electrooxidation in this study. According to Chung et al. [3], the backward oxidation (I_b) is not affected by the forward reaction; as a result, I_b cannot come from a forward scan intermediate. It was debated that in the backward direction, the surface is covered with Pt oxide, thus making I_b representative of reduction of a PtO_x surface, which must be stripped before methanol decomposition can occur [3]. Figure 7 shows mass activities plotted against shell composition for different Cu:Pt ratios. A maximum mass activity value is clearly observed at Cu:Pt = 3.0.

Table 2. Summary of CV results.

Empirical Formula	Peak Current (A × g^{-1} Pt)
Pt (commercial)	146
$Cu_{0.2}Pt_1$	57
$Cu_{1.6}Pt_1$	161
$Cu_{1.7}Pt_1$	238
$Cu_{3.0}Pt_1$	278
$Cu_{3.3}Pt_1$	228
$Cu_{5.5}Pt_1$	296
$Cu_{6.1}Pt_1$	150

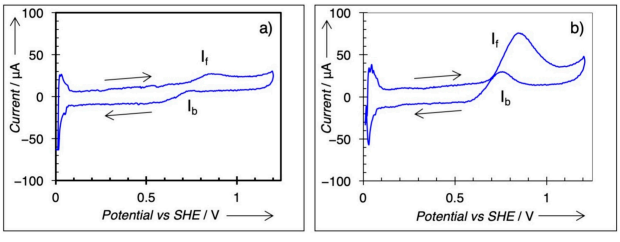

Figure 6. Cyclic voltammetry CV) traces for (**a**) $Cu_{0.23}Pt$ and (**b**) $Cu_{1.6}Pt$. Forward scan peak current (I_f) at 0.85 V used for comparison of catalysts. Cyclic voltammetry in 0.5 M H_2SO_4, 1 M methanol, scan rate 5 mV/s, at 25 °C.

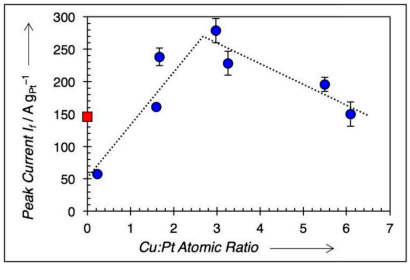

Figure 7. Mass activity of Pd@Cu–Pt/C catalysts prepared by continuous co-ED versus the atomic ratio of Cu and Pt in the shell. Dashed lines are linear regressions of the points to the left and right of peak (peak inclusive), added as a guide to the eye. Red square is a commercial 20 wt % Pt/XC-72 catalyst for comparison.

4. Discussion

The experimental results confirm that a shell composition of Cu:Pt ~3:1 is optimum for MeOH electrooxidation. There are two likely explanations. One explanation is that the addition of Cu to the shell modifies the electronic structure of Pt, specifically the d-band shape and location to the Fermi level, which can affect the strength of adsorption of intermediates, such as CO on the Pt surface. Both computational and experimental data have shown that CO adsorbs less strongly on Pt as the d-band center is shifted away from the Fermi level [8,9]. Both Pt and Cu exist as fcc metals but have different lattice parameters due to their different atomic radii in the fcc lattice. For the situation where Pt exists as an epitaxial overlayer on Cu, the first few Pt lattice layers undergo compression; the Pt–Pt and Cu–Cu bond distances, in bulk metal, are 2.77 Å and 2.56 Å, respectively. Experimentally, it has been shown that the more compressed the Pt overlayer, the weaker the binding energy of CO [8]. It is possible that the addition of Cu along with Pt in our bimetallic shell may function the same way, but not as a discrete epitaxial layer of Pt on Cu since both metals

were simultaneously deposited, but as a true mixed Pt–Cu alloy. Intuitively, the expectation is that the optimum composition would be Cu:Pt = 1:1 if this was the mechanism.

Second, the same is true if bifunctionality is the explanation for higher activities. In prior work for the ED of Ru on a commercial 20 wt % Pt/XC-72 catalyst, Ru–Pt catalysts with the loading of Ru on Pt = 0.5 ML were the optimum coverage of Ru [12]. This is consistent with a bifunctional and bimetallic Ru–Pt site where methanol is oxidized on Pt and a proximal Ru site activate H_2O to form Ru–OH to help remove CO as CO_2 (Equations (1)–(3) in this manuscript), which is supported by the disordered bimetallic alloy for the Ru–Pt system described by Watanabe [11]. A simple statistical model states the maximum number of Pt-Ru bonds exists at Pt:Ru = 1:1. For the Cu–Pt system, however, the maximum activity occurs at Cu:Pt = 3:1. In previous work by Rossmeisl, adlayers of Cu on a Pt surface performed best at a preparation giving θ_{Cu} = 0.5 ML, despite the computational models predicting optimum performance at Cu_3Pt; the authors attributed this to possible surface rearrangement to form Cu_3 trimers ($Cu_{3,tri}$) [5]. Other computational results have suggested that OH adsorption to Cu is most stable in the three-fold hollow made by $Cu_{3,tri}$, as opposed to linear Cu–OH adsorption [21].

To discount the possibility that increased activity is simply due to a higher number of surface Pt sites (Pt_s), mass normalized I_f (A/g cat) is plotted against Pt surface sites (µmol Pts/g cat) for each catalyst in Figure 8; the Pt_s values are taken from Table 1. The maximum activity is preserved at the Cu:Pt ratio ~3:1, and there is no clear positive trend relating Pt_s/g cat to mass activity, indicating that simply increasing the number of Pt_s does not account for the activity trends for among the catalysts prepared by continuous co-ED. We can now assume that the formation of $Cu_{3,tri}$–Pt ensembles are the preferred sites for MeOH electrooxidation and that the concentration of these $Cu_{3,tri}$–Pt pairs is highest for Cu_3Pt. There are also some $Cu_{3,tri}$ sites at different Cu:Pt ratios, which were also synthesized using co-ED. To determine the concentration of these sites, a simple model is used.

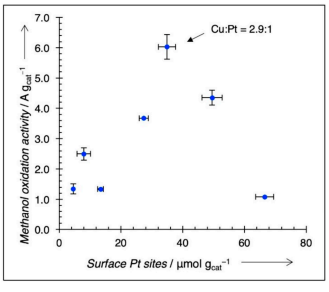

Figure 8. MeOH electrooxidation activity vs. a number of Pt surface sites (Pt_s). If increased activity is simply because there are more Pt surface sites, there should be an upward linear trend. However, this is not the case, and maximum activity is maintained at Cu_3Pt_1.

The unit cell for the surface of an fcc metal can be divided into a series of two-dimensional, four-atom primitive cells arranged in a parallelogram shape. If we assume random packing of deposited Cu and Pt atoms in the four-atom parallelogram, a simple probability for the population of these sites as independently occurring events can be used. The likelihood of depositing Cu or Pt at a lattice point is directly related to the ratio of the metals being deposited, or $P_{Cu} = X_{Cu} = N_{Cu}/(N_{Cu} + N_{Pt})$, where P_{Cu} is the probability of Cu being deposited, X_{Cu} is the atomic mole fraction of Cu being deposited, and N_{Cu} and N_{Pt} represent the molar amounts of Cu and Pt, respectively, being deposited; likewise, $P_{Pt} = X_{Pt} = N_{Pt}/(N_{Cu} + N_{Pt})$. There are 16 unique arrangements where 0, 1, 2, 3, or 4 Cu atoms can be placed in the primitive cell; four of these structures contain three Cu atoms, but only two of them have a $Cu_{3,tri}$ structure adjacent to a Pt atom, as shown in Figure 9, a graphical representation of this model. The probability of depositing 3 Cu atoms and 1 Pt atom in this primitive cell in the proper configuration is $P(Cu_{3,tri}–Pt) = 2 \bullet P_{Cu}^{\ 3} \bullet P_{Pt}$. Substituting

for an atomic fraction of Cu gives $P(Cu_{3,tri}–Pt) = 2 \bullet X_{Cu}{}^3 \bullet (1-X_{Cu})$. If we define r as the ratio of $N_{Cu}/N_{Pt} = X_{Cu}/X_{Pt}$ and rearrange, the equation gives the probability $P(Cu_{3,tri}–Pt) = 2 \bullet r^3/(1 + r)^4$. A plot of this probability for different ratios of Cu:Pt is shown in Figure 10 overlaid with the experimental mass activity results. Using $I_f = nFk_fC_O$ where n is a number of electrons removed during oxidation, k_f is a forward reaction (oxidation) constant, F is Faraday's constant, and C_O is the concentration of adsorbed methanol, then $C_O \propto X(Cu_{3,tri}–Pt)$ [48], which is proportional to the number of $Cu_{3,tri}$–Pt pairs. The shape of the curve for mass activity vs. calculated fraction of $Cu_{3,tri}$–Pt pairs are in good agreement, although there is some deviation at high Cu:Pt ratios. Using the same justification as Watanabe, the bifunctional mechanism of the $Cu_{3\ tri}$–Pt site for MeOH electrooxidation is warranted [11]. Since codeposition of Cu and Pt on the Pd, core takes place at 25 °C, and there is no high-temperature annealing after preparation of the catalyst, we can also logically assume that the positions of Cu and Pt in the fcc lattice are random (as shown by STEM images, in Figure 5) and stable during electrooxidation. In summary, the method of continuous co-ED of both Pt and Cu components in specific ratios and in a controlled manner has resulted in the synthesis of advanced, direct methanol fuel cell catalysts. It also has provided one of the few cases where direct comparisons can be made to test the predictive capabilities of computation-based studies for this important reaction.

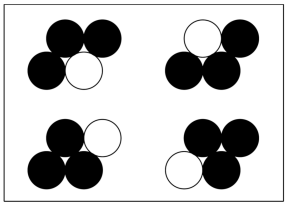

Figure 9. Positions for deposition of three Cu atoms (black) in a four atom fcc primitive cell. Only the bottom two structures have the single Pt atom (white) adjacent to a $Cu_{3,tri}$ with three-fold hollow.

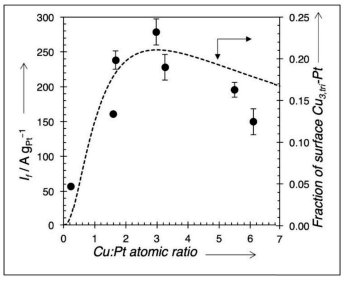

Figure 10. Calculated fraction (dashed line) of surface composed of $Cu_{3,tri}$–Pt pairs versus Cu:Pt ratio in shell overlaid with Pt mass activity for CH_3OH electrooxidation.

5. Conclusions

Continuous co-ED provides a way to make shells of mixed-metal composition with highly controlled ratios of constituent metals. This technique was successfully applied for the creation of methanol electrooxidation catalysts for DMFC applications. Mixed shells of Cu–Pt has shown markedly higher Pt mass activities than a commercial 20 wt % Pt/XC-72 electrocatalyst. The enhanced activity was correlated with the formation of bifunctional Cu–Pt sites predicted from previous computational studies [5]. The bifunctional site provides close proximity of OH_{ads} and CO_{ads} to promote facile oxidation to CO_2, thus lowering the strong inhibition effect of strongly adsorbed CO on Pt sites. Further, the ability of co-ED to prepare a wide series of bimetallic Cu–Pt shells has permitted correlation of experimental results with the optimum Cu:Pt = 3:1 ratio predicted by others [5,6]. A relatively simple

statistical model has shown that $Cu_{3,tri}$–Pt pair sites are likely to be the specific sites for enhanced activity and that the concentration of these species control activity. In these cases, H_2O is preferentially adsorbed in the three-fold hollow of a Cu_3 trimer, which is adjacent to a Pt site containing strongly adsorbed CO; the reaction is then facilitated to form CO_2, which readily desorbs. Activity trends correlate quite strongly with the calculated surface fraction of $Cu_{3,tri}$–Pt pairs.

Of economic importance is the more efficient use of Pt with this method of preparation. Pt is used only in a thin shell layer, improving the effective dispersion of Pt compared to bulk Pt alone. In this study, Pt weight loadings varied between 0.9 and 2.4 wt %. Although the core catalyst used in this study was a commercial 5 wt % Pd/C, there is no fundamental reason the core metal could not be at a lower concentration and/or a less expensive metal, so long it is stable under reaction conditions.

Further application of this method of preparation to other metals, which have OH adsorption at 3-fold hollows in an fcc lattice, could show similar mass activity trends. Currently, studies are being made with Ni–Pt and Co–Pt shells prepared using co-electroless deposition [49]. Clearly, less expensive, more active, and more stable electrocatalysts will be critical for the commercialization of any fuel cell technology.

6. Patents

J.R. Monnier, G.L. Tate, W. Xiong, and B.H. Meekins, "CO-ELECTROLESS DEPOSITION METHODS FOR FORMATION OF METHANOL FUEL CELL CATALYSTS, US pat. Appl. US 2020/0313214, 1 October 2020.

Author Contributions: Conceptualization, G.L.T. and J.R.M.; methodology, J.R.M., G.L.T. and B.A.T.M.; validation, B.A.T.M., formal analysis, G.L.T., W.X., B.A.T.M.; investigation, A.K., B.A.T.M., W.X., G.L.T.; writing—original draft preparation, G.L.T.; writing—review and editing, J.R.M.; visualization, G.L.T.; supervision, J.R.M.; project administration, J.R.M.; funding acquisition, J.R.M. All authors have read and agreed to the published version of the manuscript.

Funding: Authors are grateful to NSF, I/UCRC grant no. 1464630; DOE, grant no. DE-EE0008091; and UofSC ASPIRE-I track IIB grant no. 15510-E433 for the funding used to support this work.

Data Availability Statement: The data presented in this study are available on request from the corresponding author.

Acknowledgments: The authors are grateful to Abolfazl "Nabi" Shakouri for acquiring STEM images for this work under tight time constraints.

Conflicts of Interest: The authors declare no conflict of interest. The funders had no role in the design of the study, in the collection, analyses, or interpretation of data, in the writing of the manuscript, or in the decision to publish the results.

References

1. Koppel, T. *Powering the Future: The Ballard Fuel Cell and the Race to Change the World*; John and Wiley and Sons Canada Ltd: Mississauga, ON, Canada, 1999.
2. Poling, B.E.; Thomson, G.H.; Friend, D.G.; Rowley, R.L.; Wilding, W.V. *Perry's Chemical Engineers' Handbook*, 8th ed.; Green, D.W., Perry, R.H., Eds.; McGraw-Hill: New York, NY, USA, 2008; pp. 2–198.
3. Chung, D.Y.; Lee, K.-J.; Sung, Y.-E. Methanol Electro-oxidation on Pt Surface: Revisiting the Cyclic Volatammetry Intrepretation. *J. Phys. Chem. C* **2010**, *120*, 9028–9035. [CrossRef]
4. Day, J.B.; Vuissoz, P.-A.; Oldfield, E.; Wieckowski, A.; Ansermet, J.-P. Nuclear Magnetic Resonance Spectroscopic Study of the Electrochemical Oxidation Product of Methanol on Platinum Black. *J. Am. Chem. Soc.* **1996**, *118*, 13046–13050. [CrossRef]
5. Rossmeisl, J.; Ferrin, P.; Tritsaris, G.A.; Nilekar, A.U.; Koh, S.; Bae, S.E.; Brankovic, S.R.; Strasser, P.; Mavrikakis, M. Bifunctional anode catalysts for direct methanol fuel cells. *Energy Environ. Sci.* **2012**, *5*, 8335. [CrossRef]
6. Tritsaris, G.A.; Rossmeisl, J. Methanol Oxidation on Model Elemental and Bimetallic Transition Metal Surfaces. *J. Phys. Chem. C* **2012**, *116*, 11980–11986. [CrossRef]
7. Lai, S.C.S.; Lebedeva, N.P.; Housmans, T.H.M.; Koper, M.T.M. Mechanisms of Carbon Monoxide and Methanol Oxidation at Single-crystal Electrodes. *Top. Catal.* **2007**, *46*, 320–333. [CrossRef]
8. Schlapka, A.; Lischka, M.; Groß, A.; Käsberger, U.; Jakob, P. Surface Strain versus Substrate Interaction in Heteroepitaxial Metal Layers: Pt on Ru(0001). *Phys. Rev. Lett.* **2003**, *91*, 016101. [CrossRef]

9. Grabow, L.; Xu, Y.; Mavrikakis, M. Lattice strain effects on CO oxidation on Pt(111). *Phys. Chem. Chem. Phys.* **2006**, *8*, 3369–3374. [CrossRef]
10. Garrick, T.R.; Diao, W.; Tengco, J.M.; Stach, E.A.; Senanayake, S.D.; Chen, D.A.; Monnier, J.R.; Weidner, J.W. The Effect of the Surface Composition of Ru-Pt Bimetallic Catalysts for Methanol Oxidation. *Electrochim. Acta* **2016**, *195*, 106–111. [CrossRef]
11. Watanabe, M.; Motoo, S. Electrocatalysis by ad-atoms: Part II. Enhancement of the oxidation of methanol on platinum by ruthenium ad-atoms. *J. Electroanal. Chem.* **1975**, *60*, 267–273. [CrossRef]
12. Mehrabadi, B.A.T.; White, R.; Shakouri, A.; Regalbuto, J.R.; Weidner, J.W.; Monnier, J.R. Ruthenium-platinum bimetallic catalysts with controlled surface compositions and enhanced performance for methanol oxidation. *Catal. Today* **2019**, *334*, 156–161. [CrossRef]
13. Diao, W.; Tengco, J.M.M.; Regalbuto, J.R.; Monnier, J.R. Preparation and Characterization of Pt–Ru Bimetallic Catalysts Synthesized by Electroless Deposition Methods. *ACS Catal.* **2015**, *5*, 5123–5134. [CrossRef]
14. Mehrabadi, B.A.T.; Eskandari, S.; Khan, U.; White, R.D.; Regalbuto, J.R. Chapter One—A Review of Preparation Methods for Suported Metal Catalysts. In *Advances in Catalysis*; Song, C., Ed.; Academic Press: Cambridge, MA, USA, 2017; Volume 61, pp. 1–35.
15. Diao, W.; Tengco, J.M.M.; Gaffney, A.M.; Regalbuto, J.R.; Monnier, J.R. Rational synthesis of bimetallic catalysts using electroless deposition methods. In *Catalysis*; Spivey, J., Han, Y.F., Shekhawat, D., Eds.; Royal Society of Chemistry: London, UK, 2020; Volume 32, pp. 116–150.
16. Beard, K.; Schaal, M.; van Zee, J.; Monnier, J.R. Preparation of highly dispersed PEM fuel cell catalysts using electroless deposition methods. *Appl. Catal. B* **2007**, *72*, 262–271. [CrossRef]
17. Tengco, J.; Mehrabadi, B.T.; Zhang, Y.; Wongkaew, A.; Regalbuto, J.R.; Weidner, J.; Monnier, J.R. Synthesis and Electrochemical Evaluation of Carbon Supported Pt-Co Bimetallic Catalysts Prepared by Electroless Deposition and Modified Charge Enhanced Dry Impregnation. *Catalysts* **2016**, *6*, 83. [CrossRef]
18. Wongkaew, A.; Zhang, Y.; Tengco, J.M.M.; Blom, D.A.; Sivasubramanian, P.; Fanson, P.T.; Regalbuto, J.R.; Monnier, J.R. Characterization and evaluation of Pt-Pd electrocatalysts prepared by electroless deposition. *Appl. Catal. B* **2016**, *188*, 367–375. [CrossRef]
19. Ohashi, M.; Beard, K.D.; Ma, S.; Blom, D.A.; St-Pierre, J.; van Zee, J.W.; Monnier, J.R. Electrochemical and structural characterization of carbon-supported Pt–Pd bimetallic electrocatalysts prepared by electroless deposition. *Electrochim. Acta* **2010**, *55*, 7376–7384. [CrossRef]
20. Galhenage, R.P.; Xie, K.; Diao, W.; Tengco, J.M.M.; Seuser, G.S.; Monnier, J.R.; Chen, D.A. Platinum–ruthenium bimetallic clusters on graphite: A comparison of vapor deposition and electroless deposition methods. *Phys. Chem. Chem. Phys.* **2015**, *17*, 28354–28363. [CrossRef]
21. Xu, L.; Lin, J.; Bai, Y.; Mavrikakis, M. Atomic and Molecular Adsorption on Cu(111). *Top. Catal.* **2018**, *61*, 736–750. [CrossRef]
22. Potekaev, A.I.; Klopotov, A.A.; Starostenkov, M.D.; Klopotov, V.D.; Markova, T.N.; Morozov, M.M. Structure-phase states in the Cu-Pd-Pt system. *Steel Transl.* **2013**, *43*, 184–187. [CrossRef]
23. Nakahigashi, K. $L1_1$-Type Ordered Phase in Cu-Pt-Pd Ternary Alloys. *Jpn. J. Appl. Phys.* **1986**, *25*, 1284–1287. [CrossRef]
24. Kim, J.-S.; Lee, B.-J. Durability screening of Pt ternary alloy (111) surfaces for oxygen reduction reaction using Density Functional Theory. *Surf. Interfaces* **2020**, *18*, 100440. [CrossRef]
25. Mitsui, K.; Takahashi, M. Effect of ternary addition on the formation of Cu_3Pt and CuPt order phases in the Cu-Pt system. *Philos. Mag.* **1998**, *77*, 49–57. [CrossRef]
26. Wang, B.; Tao, L.; Cheng, Y.; Yang, F.; Jin, Y.; Zhou, C.; Yu, H.; Yang, Y. Electrocatalytic Oxidation of Small Molecule Alcohols over Pt, Pd, and Au Catalysts: The Effect of Alcohol's Hydrogen Bond Donation Ability and Molecular Structure Properties. *Catalysts* **2019**, *9*, 387. [CrossRef]
27. Capon, A.; Parsons, R. The oxidation of formic acid on noble metal electrodes: II. A comparison of the behaviour of pure electrodes. *J. Electroanal. Chem. Interfacial Electrochem.* **1973**, *44*, 239–254. [CrossRef]
28. Kadirgan, F.; Beden, B.; Leger, J.M.; Lamy, C. Synergistic effect in the electrocatalytic oxidation of methanol on platinum+palladium alloy electrodes. *J. Electroanal. Chem.* **1981**, *125*, 89–103. [CrossRef]
29. Vecchio, C.L.; Alegre, C.; Sabastián, D.; Stassi, A.; Aricò, A.S.; Baglio, V. Investigation of Supported Pd-Based Electrocatalysts for the Oxygen Reduction Reaction: Performance, Durability and Methanol Tolerance. *Materials* **2015**, *8*, 7997–8008. [CrossRef]
30. Tate, G.L.; Kenvin, A.; Diao, W.; Monnier, J.R. Preparation of Pt-containing bimetallic and trimetallic catalysts using continuous electroless deposition methods. *Catal. Today* **2019**, *334*, 113–121. [CrossRef]
31. Ohno, I.; Wakabayashi, O.; Haruyama, S. Anodic Oxidation of Reductants in Electroless Plating. *J. Electrochem. Soc.* **1985**, *132*, 2323–2330. [CrossRef]
32. Djokić, S.S. *Modern Aspects of Electrochemistry*; Conway, B.E., White, R.E., Eds.; Springer: Boston, MA, USA, 2002; Volume 35, pp. 51–133.
33. Benson, J.E.; Boudart, M. Hydrogen-oxygen titration method for the measurement of supported platinum surface areas. *J. Catal.* **1965**, *4*, 704–710. [CrossRef]
34. Vannice, M.A.; Benson, J.E.; Boudart, M. Determination of surface area by chemisorption: Unsupported platinum. *J. Catal.* **1970**, *16*, 348–356. [CrossRef]
35. Meites, L. *Handbook of Analytical Chemistry*; Meites, L., Ed.; McGraw-Hill: New York, NY, USA, 1963; p. 13.
36. Patterson, A.L. The Scherrer Formula for X-Ray Particle Size Determination. *Phys. Rev.* **1939**, *56*, 978–982. [CrossRef]

37. O'Connell, K.; Regalbuto, J.R. High Sensitivity Silicon Slit Detectors for 1 nm Powder XRD Size Detection Limit. *Catal. Lett.* **2015**, *145*, 777–783. [CrossRef]
38. King, H.W. Quantitative size-factors for metallic solid solutions. *J. Mater. Sci.* **1966**, *1*, 79–90. [CrossRef]
39. Banerjee, R.; Liu, Q.; Tengco, J.M.M.; Regalbuto, J.R. Detection of Ambient Oxidation of Ultrasmall Supported Platinum Nanoparticles with Benchtop Powder X-Ray Diffraction. *Catal. Lett.* **2017**, *147*, 1754–1764. [CrossRef]
40. Vanýsek, P. *Handbook of Chemistry and Physics*, 92nd ed.; Haynes, W.M., Ed.; CRC Press: Boca Raton, FL, USA, 2011; pp. 5–80.
41. *The Platinum Metals and Their Alloys*; Vines, R.F.; Wise, E.M. (Eds.) The International Nickel Company: New York, NY, USA, 1941; p. 84.
42. Hansen, M. *Constitution of Binary Alloys*; McGraw-Hill: New York, NY, USA, 1958; p. 1121.
43. Punyawudho, K.; Blom, D.A.; van Zee, J.W.; Monnier, J.R. Comparison of different methods for determination of Pt surface site concentrations for supported Pt electrocatalysts. *Electrochim. Acta* **2010**, *55*, 5349–5356. [CrossRef]
44. Punyawudho, K.; Vorayos, N.; Zhang, Y.; Shimpalee, S.; Monnier, J.R. Identification and quantification of performance losses for PEM fuel cells as determined by selective chemisorption and ESA measurements. *Int. J. Hydrog. Energy* **2014**, *39*, 11110. [CrossRef]
45. Bett, J.; Kinoshita, K.; Routsis, K.; Stonehart, P. A comparison of gas-phase and electrochemical measurements for chemisorbed carbon monoxide and hydrogen on platinum crystallites. *J. Catal.* **1973**, *29*, 160–168. [CrossRef]
46. Larsen, M.J.; Morales, I.J.; Cavaliere, S.; Zajac, J.; Jones, D.J.; Rozière, J.; Kaluža, L.; Gulková, D.; Odgaard, M. Development of tailored high-performance and durable electrocatalysts for advanced PEM fuel cells. *Int. J. Hydrog. Energy* **2017**, *42*, 7166–7176. [CrossRef]
47. Schneider, C.; Rasband, W.; Eliceiri, K. NIH Image to ImageJ: 25 years of Image Analysis. *Nat. Methods* **2012**, *9*, 671–675. [CrossRef]
48. Bard, A.J.; Faulkner, L.R. *Electrochemical Methods: Fundamentals and Applications*, 2nd ed.; Wiley-Interscience: New York, NY, USA, 2001; p. 92.
49. Catalyzing Commercialization: Creating Novel Bimetallic Catalysts for Methanol Fuel Cells. *Chem. Eng. Progr.* **2019**, *4*, 14.

nanomaterials

MDPI

Article

Carbon-Supported Mo_2C for Oxygen Reduction Reaction Electrocatalysis

Dušan Mladenović [1], Milica Vujković [1], Slavko Mentus [1,2], Diogo M. F. Santos [3], Raquel P. Rocha [4], Cesar A. C. Sequeira [3], Jose Luis Figueiredo [4] and Biljana Šljukić [1,3,*]

1 Faculty of Physical Chemistry, University of Belgrade, Studentski trg 12-16, 11158 Belgrade, Serbia; dusan.mladenovic@ffh.bg.ac.rs (D.M.); milica.vujkovic@ffh.bg.ac.rs (M.V.); slavko@ffh.bg.ac.rs (S.M.)
2 Serbian Academy of Sciences and Arts, Kneza Mihaila 35, 11000 Belgrade, Serbia
3 CeFEMA, Instituto Superior Técnico, Universidade de Lisboa, 1049-001 Lisbon, Portugal; diogosantos@tecnico.ulisboa.pt (D.M.F.S.); cesarsequeira@ist.utl.pt (C.A.C.S.)
4 Laboratory of Separation and Reaction Engineering-Laboratory of Catalysis and Materials (LSRE-LCM), Department of Chemical Engineering, Faculty of Engineering, University of Porto, Rua Dr. Roberto Frias, 4200-465 Porto, Portugal; rprocha@fe.up.pt (R.P.R.); jlfig@fe.up.pt (J.L.F.)
* Correspondence: biljka@ffh.bg.ac.rs or biljana.paunkovic@tecnico.ulisboa.pt; Tel./Fax: +38-(11)-13336641 or +35-(12)-18417765

Received: 13 August 2020; Accepted: 4 September 2020; Published: 10 September 2020

Abstract: Molybdenum carbide (Mo_2C)-based electrocatalysts were prepared using two different carbon supports, commercial carbon nanotubes (CNTs) and synthesised carbon xerogel (CXG), to be studied from the point of view of both capacitive and electrocatalytic properties. Cation type (K^+ or Na^+) in the alkaline electrolyte solution did not affect the rate of formation of the electrical double layer at a low scan rate of 10 mV s^{-1}. Conversely, the different mobility of these cations through the electrolyte was found to be crucial for the rate of double-layer formation at higher scan rates. Molybdenum carbide supported on carbon xerogel (Mo_2C/CXG) showed ca. 3 times higher double-layer capacity amounting to 75 mF cm^{-2} compared to molybdenum carbide supported on carbon nanotubes (Mo_2C/CNT) with a value of 23 mF cm^{-2} due to having more than double the surface area size. The electrocatalytic properties of carbon-supported molybdenum carbides for the oxygen reduction reaction in alkaline media were evaluated using linear scan voltammetry with a rotating disk electrode. The studied materials demonstrated good electrocatalytic performance with Mo_2C/CXG delivering higher current densities at more positive onset and half-wave potential. The number of electrons exchanged during oxygen reduction reaction (ORR) was calculated to be 3, suggesting a combination of four- and two-electron mechanism.

Keywords: oxygen reduction reaction; molybdenum carbide; carbon nanotubes; carbon xerogel; alkaline fuel cell

1. Introduction

Demand for sustainable and efficient energy sources to complement and eventually substitute existing fossil fuel-based ones has arisen with the increasing energy demand and environmental pollution. Electrochemical energy conversion devices such as fuel cells (FCs), batteries, and supercapacitors, are believed to be the most feasible alternatives among different energy technologies considered. Thus, the oxygen reduction reaction (ORR) has received much attention due to its application in fuel cells and metal-air batteries [1–4]. Sluggish ORR kinetics is one of the main limiting factors in the energy conversion efficiency of fuel cells and metal-air batteries, since ORR requires high overpotential and has a complex mechanism involving numerous steps [5–8]. ORR in alkaline media such as in alkaline fuel cells (AFCs) has faster kinetics, enabling the use of non-platinum

(Pt) electrocatalysts in these cells [9]. However, Pt-based electrocatalysts are currently the most common electrocatalysts in AFCs and FCs in general, holding back their large-scale production and application.

Transition metal carbides (TMCs) are a potential alternative to replace Pt-based electrocatalysts due to the TMCs' similar electronic density as Pt [10]. Furthermore, TMCs display high electrical conductivity, high oxidation resistance, high hardness, and high melting point. TMCs, such as molybdenum carbide (Mo_2C), vanadium carbide (V_8C_7), and tungsten carbide (WC), have shown similar catalytic and electrocatalytic activities as Pt-group noble metals [11–13]. For instance, TMCs have been suggested as supports for Pt and Pt-group metals in fuel cells [14–16]. Pt-group metals supported on vanadium carbide (VC) and tantalum carbide (TaC) have been shown to have synergistic effects for the ORR, while zirconium carbide (ZrC) has shown to be a good support material for hydrogen oxidation reaction electrocatalysts [17–19]. Recently, WC, carbon-supported and unsupported, has been explored as an inexpensive, Pt-free electrocatalyst for ORR [10,20–22]. Carbon-supported Mo_2C has also been reported to show high electrocatalytic activity for hydrogen evolution reaction (HER) [23,24], as well as for ORR [25–28]. TMCs' advantage for applications in fuel cells is their higher abundance (they are several orders of magnitude more abundant than Pt) [29] and, consequently, lower price as electrocatalysts account for ca. 50% of a commercial fuel cell price.

TMC particles tend to agglomerate during their synthesis, especially under high-temperature reaction conditions [10]. However, large carbide particles display lower electrocatalytic activity compared to their nanosized counterparts due to too high densities and low specific surface areas. Thus, it is of great importance to develop nanosized TMCs with controllable particle size [14]. Further increase of electrocatalysts efficiency in FCs and metal-air batteries can be achieved by using high-surface-area and high-porosity support materials [30]. The support material should additionally be characterised by high electrical conductivity along with high corrosion-stability in different electrolytes used in fuel cells. Various types of carbon materials including carbon black, activated carbon, carbon nanotubes (CNTs), carbon xerogel (CXG), and graphene have been considered and tested as electrocatalyst supports for electrochemical energy conversion and storage devices [9,31–33]. CNTs and CXG have an advantage in terms of their 3D interconnected uniform pore structure that allows a high-degree dispersion of the active material and efficient diffusion of electrolyte [34]. Hence, electrocatalysts supported on CXG and CNTs have been reported to exhibit improved performance in comparison with those supported on conventional supports, such as Vulcan carbon black [35–39].

In our recent work, we have successfully prepared Mo_2C supported on commercial CNTs (Mo_2C/CNT) and synthesised CXG (Mo_2C/CXG). In this work, Mo_2C/CNT and Mo_2C/CXG were tested as electrocatalysts for the ORR in alkaline fuel cells and for supercapacitors.

2. Materials and Methods

2.1. Materials Preparation and Characterisation

The precursor of carbon xerogel (CXG) was prepared by polycondensation of resorcinol (Sigma-Aldrich, Taufkirchen, Germany) with formaldehyde (Sigma-Aldrich, Taufkirchen, Germany). After pH adjustment to produce a mesoporous structure, gelation was completed after 3 days at 85 °C in a paraffin bath. The sample was then dried (4 days in an oven at a temperature of 60–120 °C, increasing temperature by 20 °C per day) and carbonisation was performed by heating the material to 150, 400, 600, and 800 °C. Each temperature was kept for 1–6 h to result in CXG. The detailed procedure is described in previous work [24,40]. Multi-walled CNTs (NANOCYL, NC3100 series, Nanocyl, Sambreville, Belgium) were pre-treated with hydrochloric acid (HCl) (Sigma-Aldrich, Taufkirchen, Germany) [24]. The Mo_2C electrocatalyst (Sigma-Aldrich, Taufkirchen, Germany) was supported on CXG and CNTs following a modified incipient wetness impregnation method [23,24]. Namely, an aqueous solution of ammonium molybdate (0.788 g in 6 mL, Sigma-Aldrich, Taufkirchen, Germany) was added dropwise to the carbon support (1 g), the slurry was homogenised in an ultrasonic bath (Model 3000514, JP Selecta, Barcelona, Spain) and dried at 110 °C overnight. Carburisation was

performed in a tube furnace (Termolab, Águeda, Portugal) at a slow temperature rise to 800 °C and then holding it at 800 °C for 2 h under permanent nitrogen flow (Air Liquide, 99.99995 %, Algés, Portugal). The characterization of the prepared composite electrocatalysts, Mo_2C/CNT and Mo_2C/CXG, by X-ray diffraction analysis (XRD) (Philips 1050 Bruker D8 Advance, Bruker, Billerica, MA, USA), scanning electron microscopy (SEM) (JEOL JSM 7001F, JEOL, Tokyo, Japan), thermogravimetric analysis (TGA) (TA SDT 2960, TA instruments, New Castle, DE, USA), and X-ray photoelectron spectroscopy (XPS) (Kratos AXIS Ultra HSA with VISION software, Kratos Analytical Ltd., Manchester, UK) is presented in detail in a previous paper [24].

Electrocatalysts conductivity measurements (in the form of pressure pelleted powders) were done using Wayne Kerr Universal Bridge B244 (Wayne Kerr, Begnor Regis, SXW, England).

2.2. Electrochemical Measurements

All electrochemical measurements were carried out on Gamry PCI4/300 Potentiostat/Galvanostat (Gamry Instruments, Werminster, PA, USA) using a conventional three-electrode system in a single-compartment glass cell of 50 mL volume. The working electrode (Pine Instruments, Durham, NC, USA) was prepared as described below, while a Pt electrode and a saturated calomel electrode (SCE, Hannah Instruments, Woonsocket, RI, USA) served as counter and reference electrode, respectively. All electrode potentials are converted and given relative to the reversible hydrogen electrode (RHE).

Catalytic ink was made by adding 5.0 mg of the electrocatalyst (Mo_2C/CNT or Mo_2C/CXG) with 50 μL of Nafion (5 wt.%, Sigma-Aldrich, Taufkirchen, Germany) into 750 μL of ethanol (p.a., Merck, St. Louis, MO, USA) and mixing it ultrasonically for 30 min. The working electrode (Mo_2C/CNT or Mo_2C/CXG) was prepared by pipetting 20 μL of the corresponding catalytic ink onto a polished glassy carbon electrode (GCE, 5 mm diameter) and leaving it to dry at room temperature. Current densities were calculated using the geometric surface area of the electrode.

Capacitance behaviour of the two electrocatalysts was studied by recording cyclic voltammograms (CV) in 6 M NaOH (Sigma-Aldrich, Taufkirchen, Germany) and 6 M KOH (Sigma-Aldrich, Taufkirchen, Germany) at different scan rates.

The electrodes were tested for the ORR in 0.1 M NaOH aqueous solutions at room temperature. cyclic voltammetry (CV) and linear scan voltammetry (LSV) measurements were done from 0.2 to 1 V vs. RHE at a scan rate of 10 mV s^{-1}. For rotating disk electrode (RDE) measurements, the rotation speed (ω) of the electrode was adjusted using a Pine rotator.

3. Results

3.1. Characterisation of the Electrocatalysts

The activity of two samples towards HER has been tested in the authors' previous work, along with their characterisation by XRD, SEM, TGA, and XPS [24,41]. XRD analysis confirmed the formation of α-Mo_2C onto CNTs and CXG and enabled the determination of crystal structure and average crystal size. XRD peaks were assigned to the orthorhombic structure of α-Mo_2C (ICSD card #1326) and crystallite sizes of 22.3 and 28.6 nm were evaluated for Mo_2C/CNT and Mo_2C/CXG, respectively. It should be mentioned that a previous study of ORR at different phases of molybdenum carbide supported on carbon in acidic media have shown that their activity towards ORR is strongly influenced by the carbides' structure so that α-Mo_2C/C shows higher activity compared to δ-MoC/C, most likely due to the stronger affinity of the former for O_2 adsorption [42]. This was further confirmed by the theoretical calculations of O_2 adsorption energy on the α-Mo_2C [43] and on the δ-MoC [44]. Thus, O_2 is predicted to spontaneously dissociate upon adsorption on α-Mo_2C.

TGA with linearly rising temperature in air atmosphere was used to determine the actual ratio of Mo_2C against CNT or CXG, based on the fact that the final product of the analysis is pure MoO_3. TGA data showed a similar amount of Mo_2C in both electrocatalysts. For CNT support, 28.5 wt.%

of Mo_2C was incorporated into Mo_2C/CNT. If CXG is used as support, synthesised electrocatalyst contained 25.6 wt.% of Mo_2C.

SEM and transmission electron microscopy (TEM) (FEI Tecnai F30, Thermo Fisher, Waltham, MA, USA) analyses revealed significantly different morphologies of the two electrocatalysts. Mo_2C/CNT showed characteristic tube-like morphology with tube diameters of 10–60 nm and disperse carbide nanoparticles clearly distinguishable in the TEM images (Figure 1a). For the CXG-supported electrocatalyst, particles were found to be agglomerated rather than dispersed (Figure 1b).

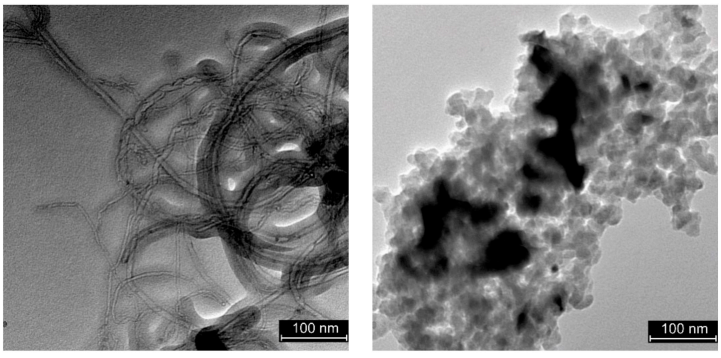

(**a**) (**b**)

Figure 1. Transmission electron microscopy (TEM) images of: (**a**) molybdenum carbide supported on carbon nanotubes (Mo_2C/CNT) and (**b**) molybdenum carbide supported on carbon xerogel (Mo_2C/CXG).

Specific surface area and porosity of electrocatalysts were investigated using N_2-sorption analysis (Quantachrome NOVA 4200e multi-station, Quantachrome Instruments, Boynton Beach, FL, USA). Mo_2C/CNT was found to be non-porous with a specific surface area of 182 m^2 g^{-1}. For mesoporous Mo_2C/CXG, an average pore diameter of ca. 18 nm and a specific area of 410 m^2 g^{-1} were determined.

XPS analysis revealed the presence of Mo in several oxidation states, including Mo 3d doublet located at 228.7 and 231.9 eV, characteristic of Mo_2C.

3.2. Electrical Conductivity Measurements

Non-porous and tube-like structure of a sample enables easier electron transport through the material, so Mo_2C/CNT showed higher conductivity (10.5 S cm^{-1}) compared to Mo_2C/CXG sample (3.8 S cm^{-1}).

3.3. The Capacitance Behaviour of Mo_2C/CXG and Mo_2C/CNT

To characterise the Mo_2C/CXG and Mo_2C/CNT interface in an alkaline aqueous solution, cyclic voltammograms of both samples were recorded in KOH and NaOH electrolyte solution (Figure 2). At a low scan rate of 10 mV s^{-1}, one can see that the capacitive current does not depend on the type of electrolyte used. Namely, the current response is determined by the sample texture, whereas the K^+ and Na^+ ions have enough time to penetrate the pores/spaces equally. At higher rates, the difference between K^+ and Na^+ adsorption/desorption processes becomes more pronounced. The ion mobility through the electrolytes turns out to be the determining step at higher scan rates, thus causing the difference in the rate of the electric double layer (EDL) formation. Namely, the higher current response in KOH than in NaOH, measured at 50 mV s^{-1}, originates from the faster motion of K^+ ions through the electrolyte, in other words, the higher transference number of K^+ vs. Na^+.

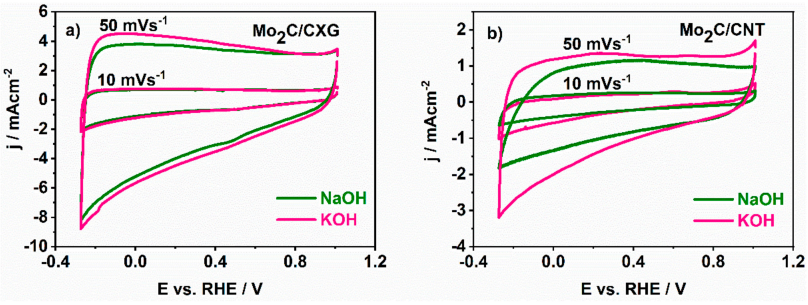

Figure 2. Cyclic voltammograms of (**a**) Mo_2C/CXG and (**b**) Mo_2C/CNT in KOH and NaOH aqueous electrolytic solution at scan rates of 10 mV s^{-1} and 50 mV s^{-1}.

The fast EDL formation at the interface of Mo_2C-based electrodes and KOH is confirmed by the stability of CVs shape upon increasing the scan rate (Figure 3).

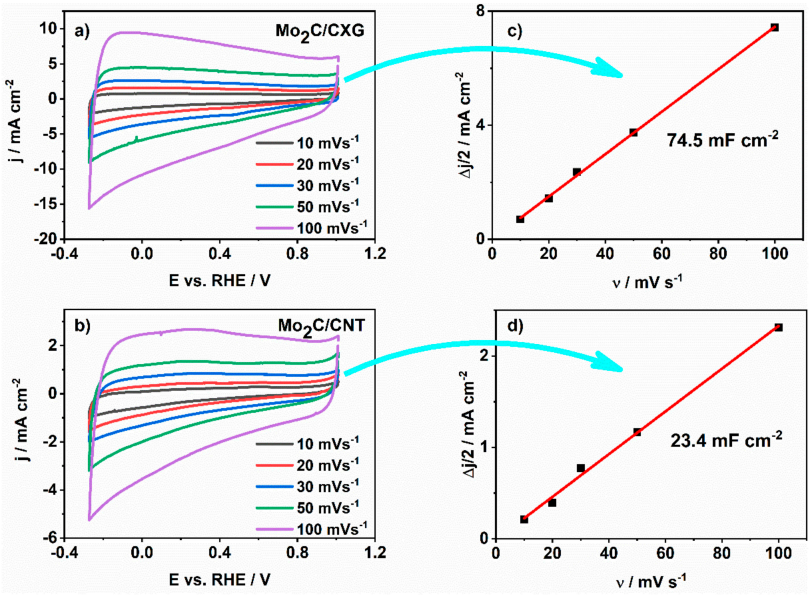

Figure 3. (**a**,**b**) Cyclic voltammograms of Mo_2C/CXG and Mo_2C/CNT in 6 M KOH at different scan rates; (**c**,**d**) specific capacitance versus scan rate, calculated from the corresponding cyclic voltammograms for each composite.

Double-layer capacity was determined as the slope of $\Delta j/2$ vs. ν plot (Figure 3c,d), where Δj is the difference of anodic j_a and cathodic j_c current densities at a given potential and ν is the scan rate. Thus, double-layer capacity was calculated to be 75 mF cm^{-2} and 24 mF cm^{-2} for Mo_2C/CXG and Mo_2C/CNT, respectively. This result indicates the higher electrochemically active surface of Mo_2C/CXG than of Mo_2C/CNT sample, in agreement with BET (Brunauer–Emmett–Teller) surface area values determined from N_2-sorption measurements performed in our previous work and evidenced in comparative cyclic voltammograms (Figure 4). The higher current response of Mo_2C/CXG compared to Mo_2C/CNT is the consequence of the higher specific surface of CXG-supported Mo_2C.

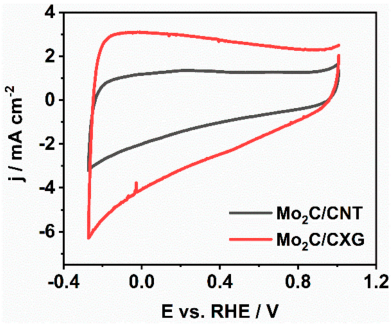

Figure 4. Cyclic voltammograms of Mo_2C/CXG and Mo_2C/CNT recorded in 6 M KOH at the scan rate of 50 mV s^{-1}.

To summarize, the background current of the electrical double layer in an alkaline solution is insensitive to the nature of cation at lower scan rates. In contrast, at higher scan rates, it is less pronounced in NaOH than in KOH. For this reason, NaOH was chosen as the conductive electrolytic medium to examine the electrocatalytic activity of samples towards the ORR.

3.4. Carbon-Supported Mo_2C Activity for ORR

The catalytic activity of carbon-supported Mo_2C electrocatalysts for ORR was investigated in O_2-saturated (Messer, 99.9995 vol%, Belgrade, Serbia) 0.1 M NaOH using LSV with a rotating disk electrode (RDE). ORR onset potential was found to be somewhat more positive at Mo_2C/CXG (0.89 V) compared to Mo_2C/CNT (0.81 V) (Figure 5) and comparable to the ORR onset potential at similar materials, such as Mo_2C nanoparticles embedded in nitrogen-doped porous carbon nanofibers (Mo_2C/NPCNFs) (0.9 V in 0.1 M KOH) [28] or Mo_2C nanowires (0.87 V in 0.1 M KOH) [45]. Generally, ORR onset potential values for different Mo_2C-based electrocatalysts were reported to range from 0.75 to 0.91 V [25–27]. Furthermore, ORR current densities at Mo_2C/CXG were found to be higher (−2.9 mA cm^{-2} for Mo_2C/CXG vs. −1.6 mA cm^{-2} for Mo_2C/CNT at 0.6 V at 1600 rpm) with ca. 90 mV higher half-wave potential (0.71 V for Mo_2C/CXG vs. 0.62 V for Mo_2C/CNT), most likely due to its porosity, higher double-layer capacitance, and larger (active) surface area that accelerate the electron transfer at the electrode/electrolyte interface and enhance its performance towards ORR. For further comparison purposes, ORR current densities at Mo_2C-based electrocatalysts at 0.6 V at 1600 rpm fall in the range from −2.3 to −4.6 mA cm^{-2} [25–28].

The reaction kinetics were studied in more detail with the evaluation of key reaction parameters and elucidation of the reaction mechanism. Koutecky–Levich (K–L, Equation (1)) analysis of the background-current corrected LSV curves enabled the determination of the number of electrons exchanged, n:

$$\frac{1}{j} = \frac{1}{j_d} + \frac{1}{j_k} = \frac{1}{0.62nFD^{2/3}\nu^{-1/6}C_{bulk}\omega^{1/2}} + \frac{1}{j_k}, \quad (1)$$

where j, j_k, and j_d are measured current density, kinetic current density (free of mass-transfer limitations), and the limiting diffusion current density at the electrode potential E, respectively. Additionally, D is the O_2 diffusion coefficient (1.9×10^{-5} cm^2 s^{-1}), ν is the solution kinematic viscosity (0.01 cm^2 s^{-1}), and C_{bulk} is the concentration of dissolved O_2 (1.2×10^{-3} M). As defined, j_d is determined by the physicochemical properties of the solution and electrode potential E in the same manner as n. Though K–L analysis is a standard way to determine the number of electrons transferred during the ORR, it should be kept in mind that this analysis is derived for a single one-electron transfer with a preceding chemical reaction of first order and, as such, it might not give absolutely reliable results in case of multi-step reactions involving intermediates [46,47]. Additionally, the K–L analysis might not give reliable results in cases where surfaces may be rough, porous, or both [46] or in case of electrode

surface modified with nanoparticles where the real surface area differs from the electrode's geometric area [47]. Rotating ring disk measurements have been suggested as alternatives, but they still bring some misinterpretation of results due to the theory behind them not being valid for multi-step reactions.

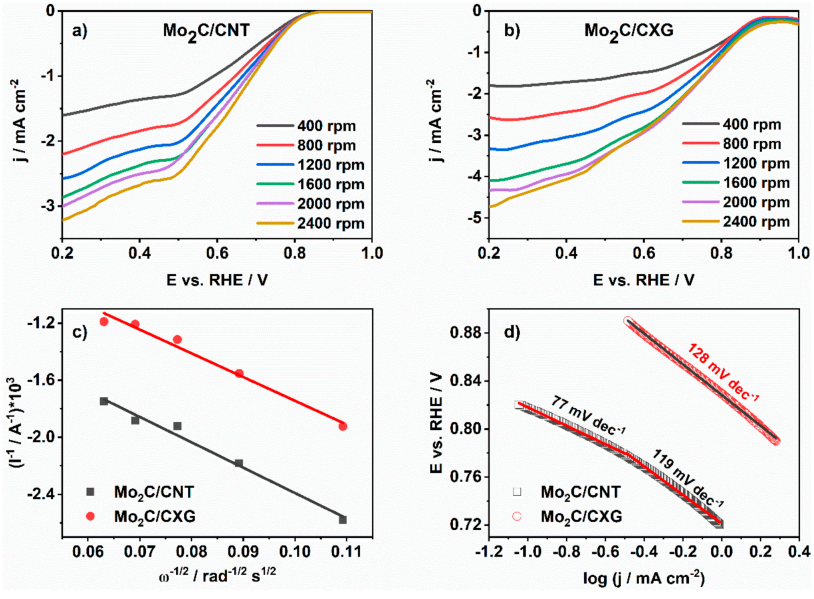

Figure 5. Linear scan voltammograms (LSVs) at different rotation rates for (**a**) Mo_2C/CXG and (**b**) Mo_2C/CNT in O_2-saturated 0.1 M NaOH with (**c**) Koutecky–Levich (K–L) analysis and (**d**) Tafel analysis of oxygen reduction reaction (ORR) at tested samples.

The RDE profiles of two studied carbon-supported Mo_2C showed increasing current density with increasing rotation rates up to 2400 rpm, indicating a kinetic limitation of the reaction. Constructed K–L plots (Figure 5c) represented straight lines of good linearity, suggesting that ORR is a first-order reaction with respect to O_2 concentration in the electrolytic solution [27]. For Mo_2C/CNT and Mo_2C/CXG, n values were determined from the slope of K–L plots to be 2.7 and 3.0 electrons, respectively. Similar behaviour has been reported for the case of unsupported and carbon-supported Mo_2C nanowires where average n during ORR was determined to be 3 in 0.7–0.4 V potential range and 4 in 0.3–0 V potential range. Values from 2.1 to 3.8 have been reported for different Mo_2C-based electrocatalysts [25–28].

Next, Tafel analysis was carried out providing insight into the mechanism of oxygen adsorption on the surface of two studied samples. ORR Tafel slopes, b, were determined from the mass transfer-corrected j vs. E curves at 1600 rpm, Figure 5d. It has been pointed out that choosing a suitable current range relative to the value of the limiting steady-state current for Tafel analysis might provide more reliable results than choosing a suitable potential range [48]. The suitable current typically lies in the 10–80% range of the limiting current (upon mass-transfer correction). Still, the authors opted for defining a potential range for Tafel analysis as well-defined limiting current densities were not reached.

b values for the ORR at Mo_2C/CNT were evaluated to be 77 mV dec^{-1} (in the low overpotential region where the ORR rate is governed by the rate of surface reaction on the electrocatalyst) and 119 mV dec^{-1}. For Mo_2C/CXG, only one Tafel slope was observed with a value of 128 mV dec^{-1}. Tafel slope for ORR at Mo_2C nanowires was reported to be 65 mV dec^{-1} in low overpotential region (0.87–0.83 V), close to the value for a Pt/C catalyst (64 mV dec^{-1}) [45], 60.2 mV dec^{-1} at Mo_2C/NPCNFs, while Tafel slope of ORR at Mo_2C NPs embedded in Fe-N-doped carbon nanolayers (Mo_2C@NC-Fe) was as low as 46 mV dec^{-1} [49].

4. Discussion

ORR can occur through two- or four-electron mechanism. The four-electron mechanism implies a direct reduction of molecular oxygen to water by the exchange of four electrons. This is the preferred pathway for oxygen reduction because the alternative two-electron mechanism implies a reduction of molecular oxygen to water via an intermediate step in which peroxide ions are formed. Peroxide can then be reduced to water or can segregate from the electrode and not be involved in the subsequent reaction. ORR on almost all catalysts proceeds by a combination of these two mechanisms where the four-electron mechanism is only dominant in the activation-controlled potential range. One of the most investigated catalysts on which ORR is dominantly occurring through a four-electron mechanism is Pt and Pt-based catalysts; however, even on them, ORR is not occurring by this mechanism in the whole ORR potential range. The number of exchanged electron values obtained herein indicated that ORR at Mo_2C/CNT and Mo_2C/CXG is under mixed control where both of the above-mentioned mechanisms are involved, as supported by the appearance of two reduction waves. Previous studies on other Mo_2C-based electrocatalysts indicated that the ORR at these electrocatalysts also proceeds by a combination of two-electron and four-electron mechanisms or by a two-step two-electron mechanism involving the generation of HO_2^- intermediate [44].

Tafel slope values of 119 and 128 mV dec^{-1} determined for Mo_2C/CNT (high overpotential region) and Mo_2C/CXG suggest that, though O_2 adsorbs dissociatively on the Mo_2C surface at room temperature [42,50], in an aqueous solution, O_2 and H_2O adsorption are competing so that O_2 adsorption might become the rate-determining step [42].

Supporting Mo_2C nanoparticles on carbon materials, commercial CNTs and prepared CXG, resulted in their good catalytic performance towards ORR for electrochemical energy conversion and storage applications. Their activity is attributed to the synergic effect between carbide species and carbon support. The nature of the catalytic sites (Mo_2C species, molybdenum oxides, or molybdenum oxycarbide species) for the ORR is still under discussion. Namely, it has been shown that the surface of Mo_2C particles is contaminated with molybdenum oxides (MoO_3 and MoO_2), but their concentration notably decreases upon short activation by galvanostatic electrolysis. The activity of Mo_2C/CXG was observed to be somewhat higher due to its porosity and large active surface area that accelerate the interfacial electrochemical reaction. In comparison with the available data for other Mo_2C-based electrocatalysts reported in the literature so far (Table 1), Mo_2C/CXG shows higher onset potential along with comparable current densities and number of exchange electrons.

Table 1. Comparison of ORR performance of Mo_2C/CXG and Mo_2C/CNT with other reported Mo_2C-based catalysts.

Catalysts	Onset Potential / V	Current Density at 0.6 V ; / mA cm^{-2}	Tafel Slope / mV dec^{-1}	Electron Transfer Number	Reference
G-Mo_2C	0.75	−2.3	/	2.1–3.2	[25]
FeMo carbide/NG	0.91	−3.5	/	3.5	[27]
Mo_2C nanowires	0.87	−2.7	65	3–4	[45]
Hollow Mo_2C-C microspheres	0.83	−4.2	72.2	3.2–3.6	[26]
Mo_2C/NPCNFs	0.90	−4.6	60.3	3.8	[28]
Mo_2C@NC-Fe	/	/	46	3.7	[49]
C(Mo_2C)	0.84	/	57 (126)	2.8	[51]
Mo-doped MCG	0.76	/	37	2.3	[52]
Mo_2C/CXG	0.89	−2.9	128	3.0	This work
Mo_2C/CNT	0.81	−1.6	77 (119)	2.7	This work

G-Mo_2C—graphite carbon-supported Mo_2C; NG—nitrogen-doped graphene; NPCNFs—nanoparticles embedded nitrogen-doped porous carbon nanofibers; NC-Fe—Fe-N-doped carbon nanolayers; C(Mo_2C)—micromesoporous molybdenum carbide-derived carbon powder; MCG—mesoporous carbon/graphene composite.

Compared to the herein studied catalysts, better results in terms of Tafel slope and current densities at a given potential values display the compositions Mo_2C/NPCNFs [28] and Mo_2C@NC-Fe [49]. In the case of the Mo_2C@NC-Fe catalyst, better performance may be attributed to the promotive effect of ferrous carbide. Considering Mo_2C/NPCNFs, its synthesis procedure assumed a simultaneous outbreak of molybdenum carbide and carbon support which most likely led to a better contact between them. These facts may serve as directions for future improvement of the herein studied catalysts.

5. Conclusions

Within this study, it was shown that the type of cation (K^+ or Na^+) in the alkaline electrolytic solution does not affect the rate of the formation of an electrical double layer at low scan rates, since both K^+ and Na^+ ions are capable of penetrating the available active sites. However, the different mobility of these cations through the electrolyte is found to be critical for the rate of double-layer formation at higher scan rates. Thus, the capacity of ions that are involved in the EDL formation was higher in KOH than in NaOH, due to the higher mobility of K^+ ions through the electrolyte. Furthermore, Mo_2C/CXG shows higher specific capacitance than Mo_2C/CNT (75 mF cm^{-2} vs. 23 mF cm^{-2}), due to the higher specific surface area and porosity.

The catalytic performance of two carbon-supported Mo_2C in alkaline solution was comparable so that ORR proceeds by a combination of two- and four-electron mechanisms at both electrocatalysts. Mo_2C/CXG showed somewhat higher activity in terms of the ORR onset potential, half-wave potential, and recorded current densities due to the mentioned higher surface area and a higher number of active sites. Therefore, the use of inexpensive carbides on highly-conductive, high-surface-area carbon nanotubes and carbon xerogel support materials points out a new direction of electrocatalyst performance optimisation for next-generation fuel cells. Further work should include testing of long-term stability of synthesised samples and evaluating the potential application in fuel cells, metal-air batteries, and supercapacitors.

Author Contributions: Conceptualization, M.V. and B.Š.; investigation, R.P.R., M.V., S.M., and B.Š.; data curation, D.M.; writing—original draft preparation, D.M. and B.Š.; writing—review and editing, J.L.F., C.A.C.S., D.M.F.S., S.M., and B.Š.; visualization, D.M. All authors have read and agreed to the published version of the manuscript.

Funding: This research was funded by the Foundation for Science and Technology (FCT, Portugal) contract no. IF/01084/2014/CP1214/CT0003 under IF2014 Programme (D.M.F. Santos) and contract no. IST-ID/156/2018 (B. Šljukić), by the Ministry of Education, Science and Technological Development of Republic of Serbia (contract no. 451-03-68/2020-14/200146), by the Serbian Academy of Sciences and Arts (Contract no. F-190: Electrocatalysis in Contemporary Processes of Energy Conversion) and by Base Funding - UIDB/50020/2020 of the Associate Laboratory LSRE-LCM - funded by national funds through FCT/MCTES (PIDDAC).

Conflicts of Interest: The authors declare no conflict of interest.

References

1. Dresselhaus, M.S.; Thomas, I.L. Alternative energy technologies. *Nature* **2001**, *414*, 332–337. [CrossRef] [PubMed]
2. Adzic, R.R. Electrocatalysis. In *Frontiers in Electrochemistry*; Lipkowski, J., Ross, P.N., Eds.; Wiley-VCH: New York, NY, USA, 1998; Volume 3, p. 197.
3. Bruce, P.G.; Hardwick, L.J.; Abraham, K.M. Lithium-air and lithium-sulfur batteries. *MRS Bull.* **2011**, *36*, 506–512. [CrossRef]
4. Cheng, F.; Chen, J. Metal-air batteries: from oxygen reduction electrochemistry to cathode catalysts. *Chem. Soc. Rev.* **2012**, *41*, 2172. [CrossRef] [PubMed]
5. Gatto, I.; Stassi, A.; Passalacqua, E.; Aricò, A. An electro-kinetic study of oxygen reduction in polymer electrolyte fuel cells at intermediate temperatures. *Int. J. Hydrogen Energy* **2013**, *38*, 675–681. [CrossRef]
6. Dong, H.; Lin, B.; Gilmore, K.; Hou, T.; Lee, S.-T.; Li, Y. Theoretical investigations on SiC_2 siligraphene as promising metal-free catalyst for oxygen reduction reaction. *J. Power Sources* **2015**, *299*, 371–379. [CrossRef]
7. Keith, J.A.; Jerkiewicz, G.; Jacob, T. Theoretical Investigations of the Oxygen Reduction Reaction on Pt(111). *ChemPhysChem* **2010**, *11*, 2779–2794. [CrossRef]

8. Wang, B. Recent development of non-platinum catalysts for oxygen reduction reaction. *J. Power Sources* **2005**, *152*, 1–15. [CrossRef]
9. Šljukić, B.; Santos, D.M.F.; Sequeira, C. Manganese dioxide electrocatalysts for borohydride fuel cell cathodes? *J. Electroanal. Chem.* **2013**, *694*, 77–83. [CrossRef]
10. Ko, A.-R.; Lee, Y.-W.; Moon, J.-S.; Han, S.-B.; Cao, G.; Park, K.-W. Ordered mesoporous tungsten carbide nanoplates as non-Pt catalysts for oxygen reduction reaction. *Appl. Catal., A* **2014**, *477*, 102–108. [CrossRef]
11. Tominaga, H.; Aoki, Y.; Nagai, M. Hydrogenation of CO on molybdenum and cobalt molybdenum carbides. *Appl. Catal. A.* **2012**, *423–424*, 192–204. [CrossRef]
12. Esposito, D.V.; Hunt, S.T.; Kimmel, Y.C.; Chen, J.G. A new class of electrocatalysts for hydrogen production from water electrolysis: Metal monolayers supported on low-cost transition metal carbides. *J. Am. Chem. Soc.* **2012**, *134*, 3025–3033. [CrossRef] [PubMed]
13. Cheekatamarla, P.; Thomson, W.J. Catalytic activity of molybdenum carbide for hydrogen generation via diesel reforming. *J. Power Sources* **2006**, *158*, 477–484. [CrossRef]
14. Yan, Z.; He, G.; Shen, P.K.; Luo, Z.; Xie, J.; Chen, M. MoC-graphite composite as a Pt electrocatalyst support for highly active methanol oxidation and oxygen reduction reaction. *J. Mater. Chem. A* **2014**, *2*, 4014–4022. [CrossRef]
15. Elbaz, L.; Kreller, C.R.; Henson, N.J.; Brosha, E.L. Electrocatalysis of oxygen reduction with platinum supported on molybdenum carbide-carbon composite. *J. Electroanal. Chem.* **2014**, *720–721*, 34–40. [CrossRef]
16. Nikolic, V.M.; Perović, I.; Gavrilov, N.M.; Pašti, I.A.; Šaponjić, A.; Vulić, P.J.; Karic, S.D.; Babić, B.M.; Kaninski, M.P. On the tungsten carbide synthesis for PEM fuel cell application—Problems, challenges and advantages. *Int. J. Hydrogen Energy* **2014**, *39*, 11175–11185. [CrossRef]
17. Hu, Z.; Chen, C.; Meng, H.; Wang, R.; Shen, P.K.; Fu, H. Oxygen reduction electrocatalysis enhanced by nanosized cubic vanadium carbide. *Electrochem. Commun.* **2011**, *13*, 763–765. [CrossRef]
18. Polonský, J.; Petrushina, I.M.; Christensen, E.; Bouzek, K.; Prag, C.B.; Andersen, J.E.T.; Bjerrum, N.J. Tantalum carbide as a novel support material for anode electrocatalysts in polymer electrolyte membrane water electrolysers. *Int. J. Hydrogen Energy* **2012**, *37*, 2173–2181. [CrossRef]
19. Horigome, M.; Kobayashi, K.; Suzuki, T.M. Impregnation of metal carbides in Raney Ni-PTFE hydrogen electrodes. *Int. J. Hydrogen Energy* **2007**, *32*, 365–370. [CrossRef]
20. Huang, T.; Mao, S.; Pu, H.; Wen, Z.; Huang, X.; Ci, S.; Chen, J. Nitrogen-doped graphene-vanadium carbide hybrids as a high-performance oxygen reduction reaction electrocatalyst support in alkaline media. *J. Mater. Chem. A* **2013**, *1*, 13404–13410. [CrossRef]
21. Huang, T.; Yu, J.; Han, J.; Zhang, Z.; Xing, Y.; Wen, C.; Wu, X.; Zhang, Y. Oxygen reduction catalytic characteristics of vanadium carbide and nitrogen doped vanadium carbide. *J. Power Sources* **2015**, *300*, 483–490. [CrossRef]
22. Zhou, X.; Qiu, Y.; Yu, J.; Yin, J.; Gao, S. Tungsten carbide nanofibers prepared by electrospinning with high electrocatalytic activity for oxygen reduction. *Int. J. Hydrogen Energy* **2011**, *36*, 7398–7404. [CrossRef]
23. Chen, W.F.; Wang, C.H.; Sasaki, K.; Marinkovic, N.; Xu, W.; Muckerman, J.T.; Zhu, Y.; Adzic, R.R. Highly active and durable nanostructured molybdenum carbide electrocatalysts for hydrogen production. *Energy Environ. Sci.* **2013**, *6*, 943–951. [CrossRef]
24. Šljukić, B.; Vujković, M.; Amaral, L.; Santos, D.M.F.; Rocha, R.P.; Sequeira, C.A.C.; Figueiredo, J.L. Carbon-supported Mo_2C electrocatalysts for hydrogen evolution reaction. *J. Mater. Chem. A* **2015**, *3*, 15505–15512. [CrossRef]
25. Huang, K.; Bi, K.; Liang, C.; Lin, S.; Wang, W.J.; Yang, T.Z.; Liu, J.; Zhang, R.; Fan, D.Y.; Wang, Y.G.; et al. Graphite carbon-supported Mo_2C nanocomposites by a single-step solid state reaction for electrochemical oxygen reduction. *PLoS One* **2015**, *10*, e0138330. [CrossRef] [PubMed]
26. Luo, Y.; Wang, Z.; Fu, Y.; Jin, C.; Wei, Q.; Yang, R. In situ preparation of hollow Mo_2C-C hybrid microspheres as bifunctional electrocatalysts for oxygen reduction and evolution reactions. *J. Mater. Chem. A* **2016**, *4*, 12583–12590. [CrossRef]
27. Chen, M.; Liu, J.; Zhou, W.; Lin, J.; Shen, Z. Nitrogen-doped graphene-supported transition-metals carbide electrocatalysts for oxygen reduction reaction. *Sci. Rep.* **2015**, *5*, 10389. [CrossRef]
28. Wang, H.; Sun, C.; Cao, Y.; Zhu, J.; Chen, Y.; Guo, J.; Zhao, J.; Sun, Y.; Zou, G. Molybdenum carbide nanoparticles embedded in nitrogen-doped porous carbon nanofibers as a dual catalyst for hydrogen evolution and oxygen reduction reactions. *Carbon* **2017**, *114*, 628–634. [CrossRef]

29. Kimmel, Y.C.; Xu, X.; Yu, W.; Yang, X.; Chen, J.G. Trends in electrochemical stability of transition metal carbides and their potential use as supports for low-cost electrocatalysts. *ACS Catal.* **2014**, *4*, 1558–1562. [CrossRef]
30. Te Hsieh, C.; Lin, J.Y. Fabrication of bimetallic Pt-M (M = Fe, Co, and Ni) nanoparticle/carbon nanotube electrocatalysts for direct methanol fuel cells. *J. Power Sources* **2009**, *188*, 347–352. [CrossRef]
31. Shanmugharaj, A.M.; Ryu, S.H. Excellent electrochemical performance of graphene-silver nanoparticle hybrids prepared using a microwave spark assistance process. *Electrochim. Acta* **2012**, *74*, 207–214. [CrossRef]
32. Aricò, A.S.; Baglio, V.; Di Blasi, A.; Modica, E.; Monforte, G.; Antonucci, V. Electrochemical analysis of high temperature methanol electro-oxidation at Pt-decorated Ru catalysts. *J. Electroanal. Chem.* **2005**, *576*, 161–169. [CrossRef]
33. Job, N.; Pirard, R.; Marien, J.; Pirard, J.P. Synthesis of transition metal-doped carbon xerogels by solubilization of metal salts in resorcinol-formaldehyde aqueous solution. *Carbon* **2004**, *42*, 3217–3227. [CrossRef]
34. Arbizzani, C.; Righi, S.; Soavi, F.; Mastragostino, M. Graphene and carbon nanotube structures supported on mesoporous xerogel carbon as catalysts for oxygen reduction reaction in proton-exchange-membrane fuel cells. *Int. J. Hydrogen Energy* **2011**, *36*, 5038–5046. [CrossRef]
35. Alegre, C.; Gálvez, M.E.; Moliner, R.; Baglio, V.; Aricò, A.S.; Lázaro, M.J. Towards an optimal synthesis route for the preparation of highly mesoporous carbon xerogel-supported Pt catalysts for the oxygen reduction reaction. *Appl. Catal., B* **2014**, *147*, 947–957. [CrossRef]
36. Al-Muhtaseb, S.A.; Ritter, J.A. Preparation and properties of resorcinol-formaldehyde organic and carbon gels. *Adv. Mater.* **2003**, *15*, 101–114. [CrossRef]
37. Job, N.; Pereira, M.F.R.; Lambert, S.; Cabiac, A.; Delahay, G.; Colomer, J.F.; Marien, J.; Figueiredo, J.L.; Pirard, J.P. Highly dispersed platinum catalysts prepared by impregnation of texture-tailored carbon xerogels. *J. Catal.* **2006**, *240*, 160–171. [CrossRef]
38. Samant, P.V.; Fernandes, J.B.; Rangel, C.M.; Figueiredo, J.L. Carbon xerogel supported Pt and Pt-Ni catalysts for electro-oxidation of methanol in basic medium. *Catal. Today* **2005**, *102–103*, 173–176. [CrossRef]
39. Job, N.; Marie, J.; Lambert, S.; Berthon-Fabry, S.; Achard, P. Carbon xerogels as catalyst supports for PEM fuel cell cathode. *Energy Convers. Manage.* **2008**, *49*, 2461–2470. [CrossRef]
40. Job, N.; Pirard, R.; Marien, J.; Pirard, J.P. Porous carbon xerogels with texture tailored by pH control during sol-gel process. *Carbon* **2004**, *42*, 619–628. [CrossRef]
41. Šljukic, B.; Santos, D.M.F.; Vujkovic, M.; Amaral, L.; Rocha, R.P.; Sequeira, C.A.C.; Figueiredo, J.L. Molybdenum Carbide Nanoparticles on Carbon Nanotubes and Carbon Xerogel: Low-Cost Cathodes for Hydrogen Production by Alkaline Water Electrolysis. *ChemSusChem* **2016**, *9*, 1200–1208. [CrossRef]
42. Gómez-Marín, A.M.; Bott-Neto, J.L.; Souza, J.B.; Silva, T.L.; Beck, W.; Varanda, L.C.; Ticianelli, E.A. Electrocatalytic Activity of Different Phases of Molybdenum Carbide/Carbon and Platinum–Molybdenum Carbide/Carbon Composites toward the Oxygen Reduction Reaction. *ChemElectroChem* **2016**, *3*, 1570–1579. [CrossRef]
43. Ren, J.; Huo, C.F.; Wang, J.; Li, Y.W.; Jiao, H. Surface structure and energetics of oxygen and CO adsorption on α-Mo_2C(0 0 0 1). *Surf. Sci.* **2005**, *596*, 212–221. [CrossRef]
44. Viñes, F.; Sousa, C.; Illas, F.; Liu, P.; Rodriguez, J.A. A systematic density functional study of molecular oxygen adsorption and dissociation on the (001) surface of group IV-VI transition metal carbides. *J. Phys. Chem. C* **2007**, *111*, 16982–16989. [CrossRef]
45. Liao, L.; Bian, X.; Xiao, J.; Liu, B.; Scanlon, M.D.; Girault, H.H. Nanoporous molybdenum carbide wires as an active electrocatalyst towards the oxygen reduction reaction. *Phys. Chem. Chem. Phys.* **2014**, *16*, 10088–10094. [CrossRef]
46. Sokolov, S.V.; Sepunaru, L.; Compton, R.G. Taking cues from nature: Hemoglobin catalysed oxygen reduction. *Appl. Mater. Today* **2017**, *7*, 82–90. [CrossRef]
47. Masa, J.; Batchelor-McAuley, C.; Schuhmann, W.; Compton, R.G. Koutecky–Levich analysis applied to nanoparticle modified rotating disk electrodes: Electrocatalysis or misinterpretation. *Nano Res.* **2014**, *7*, 71–78. [CrossRef]
48. Li, D.; Batchelor-McAuley, C.; Compton, R.G. Some thoughts about reporting the electrocatalytic performance of nanomaterials. *Appl. Mater. Today* **2020**, *18*, 100404. [CrossRef]
49. Xu, Y.; Chen, T.; Wang, T.; Yang, J.; Zhu, Y.; Ding, W. Molybdenum carbide promotion on Fe-N-doped carbon nanolayers facilely prepared for enhanced oxygen reduction. *Nanoscale* **2018**, *10*, 21944–21950. [CrossRef]

50. Óvári, L.; Kiss, J.; Farkas, A.P.; Solymosi, F. Surface and subsurface oxidation of Mo_2C/Mo(100): Low-energy ion-scattering, auger electron, angle-resolved X-ray photoelectron, and mass spectroscopy studies. *J. Phys. Chem. B* **2005**, *109*, 4638–4645. [CrossRef]
51. Jäger, R.; Kasatkin, P.E.; Härk, E.; Lust, E. Oxygen reduction on molybdenum carbide derived micromesoporous carbon electrode in alkaline solution. *Electrochem. Commun.* **2013**, *35*, 97–99. [CrossRef]
52. Dong, Y.; Liu, M.; Liu, Y.; Wang, S.; Li, J. Molybdenum-doped mesoporous carbon/graphene composites as efficient electrocatalysts for the oxygen reduction reaction. *J. Mater. Chem. A* **2015**, *3*, 19969–19973. [CrossRef]

MDPI
St. Alban-Anlage 66
4052 Basel
Switzerland
Tel. +41 61 683 77 34
Fax +41 61 302 89 18
www.mdpi.com

Nanomaterials Editorial Office
E-mail: nanomaterials@mdpi.com
www.mdpi.com/journal/nanomaterials

MDPI
St. Alban-Anlage 66
4052 Basel
Switzerland

Tel: +41 61 683 77 34

www.mdpi.com

ISBN 978-3-0365-4822-7